THE CHARACTERIZATION AND SOURCE IDENTIFICATION OF AIRBORNE PARTICLES IN HONG KONG

GAO YUAN

Ph.D

The Hong Kong Polytechnic University

2016

The Hong Kong Polytechnic University

Department of Civil and Environmental Engineering

The characterization and source identification of airborne particles in Hong Kong

by:

GAO Yuan

A thesis submitted in partial fulfillment of the requirements

for the degree of Doctor of Philosophy

April, 2016

Certificate of originality

I hereby declare that this thesis entitled “the characterization and source identification of airborne particles in Hong Kong” is my own work and that to the best of my knowledge and belief, it reproduces no material previously published or written nor material which has been accepted for the award of any other degree or diploma, except where due acknowledgement has been made in the text.

----------(Signed)

----------Gao Yuan----------(Name of student)

Abstract

Low visual range indicates an air pollution problem. In Hong Kong, poor visibility has been of increasing concern since 2000. This thesis explores the relationships between local air pollution and visibility degradation by characterizing particle optical and chemical properties, estimating chemical contributions to light extinction, and identifying particulate matter sources.

Particle light scattering and absorption coefficients (B_{sp}, B_{ap}) in Hong Kong differ among urban, sub-urban and rural areas. Highest values were observed in urban areas due to particles from traffic and cooking sources in addition to regionally distributed particles. Regional-scale B_{sp} and B_{ap} measured outside the urbanized area was dominantly affected by secondary sulfate, nitrate and organics.

The highest PM_{10} concentrations were observed during the fall and the lowest were found during the spring at three sampling sites. Urban particulate matters (PM) contained large increments of organic and elemental carbon (EC), typical of engine exhaust. Dominant species in the urban area were particle organic matters (POM) and EC, which due to high traffic flow. Regional transportation and stagnant meteorological conditions elevated aged and secondary pollutants in the Hong Kong sub-urban area.

Most of the SO_4^{2-}, NH_4^+, K^+, OC and EC, were in the size range of 0.56 μm to 1.8 μm, NO_3^- and Cl^- were dominated in the 1.8 μm to 10 μm size range. Because of complex chemical compositions in droplet mode, eight emission sources profiles have been determined in the mode. The largest contribution of droplet mode source was from anthropogenic emission sources, i.e. secondary SO_4^{2-} (24%), industrial

emission (19%), vehicle emission, secondary NO_3^- and sea salt (13-15% in each) with 10% of other sources. Relatively simple sources were identified in the coarse mode (3 sources) and the condensation mode (4 sources). Over 80% of PM_{coarse} mass comprised of sea salt and soil dust. Most of the primary emissions were identified in the condensation mode, including 27% vehicle emissions and 18-19% each from residual oil combustion and coal/biomass burning. Secondary formation i.e. secondary SO_4^{2-} contributed approximately 37% of the particles in the condensation mode

The special chemical composition and particles size distribution in Hong Kong was observed, mass scattering efficiency of Hong Kong need to be determined. The Hong Kong mass scattering efficiency (MSE) value was investigated under the clean and polluted air quality situation. It is presented as follows: 2.6 (clean) and 3.2 m^2/g (polluted) for ammonium sulfate, 2.2 (clean) and 1.5 m^2/g (polluted) for ammonium nitrate, 2.1 (clean) and 4.3 m^2/g (polluted) for particle organic matters, 1.5 m^2/g for sea salt and 1.5 m^2/g for soil dust.

In general, the largest contributors to particle light extinction in Hong Kong were traffic/engine emission and secondary formation. In other words, to improve visibility degradation situation in HK, the government should control the local traffic emission and build the collaboration with regional institution or government to improve regional air quality. In addition, the air pollution in Hong Kong was mainly affected by south and south east China during autumn and winter months and by north and central China during spring and summer months.

.

Publications

International journals

Gao Y, Lai S, Lee S-C, Yau PS, Huang Y, Cheng Y, Wang T., Xu Z., Yuan C., Zhang Y. Optical properties of size-resolved particles at a Hong Kong urban site during winter. Atmospheric Research 2015; 155: 1-12.

Gao Y, Lee S-C, Huang Y, Chow JC, Watson JG. Chemical characterization and source apportionment of size-resolved particles in Hong Kong sub-urban area. Atmospheric Research 2016; 170: 112-122.

Cheng, Y., Lee, S.C., **Gao, Y.,** Cui, L., Deng, W., Cao, J., Shen, Z., Sun, J., 2015. Real-time measurements of $PM_{2.5}$, $PM_{10–2.5}$, and BC in an urban street canyon. Particuology 20, 134-140.

Yang F, Kawamura K, Chen J, Ho K, Lee S, **Gao Y,** Cui, L, Wang, T, Fu P, Anthropogenic and biogenic organic compounds in summertime fine aerosols ($PM_{2.5}$) in Beijing, China. Atmospheric Environment 2016; 124, Part B: 166-175.

Huang, Y., Ling, Z.H., Lee, S.C., Ho, S.S.H., Cao, J.J., Blake, D.R., Cheng, Y., Lai, S.C., Ho, K.F., **Gao, Y.**, Cui, L., Louie, P.K.K., 2015. Characterization of volatile organic compounds at a roadside environment in Hong Kong: An investigation of influences after air pollution control strategies. Atmospheric Environment 122, 809-818.

Guo, J., Tilgner, A., Yeung, C., Wang, Z., Louie, P.K.K., Luk, C.W.Y., Xu, Z., Yuan, C., **Gao, Y.,** Poon, S., Herrmann, H., Lee, S., Lam, K.S., Wang, T., 2014.

Atmospheric Peroxides in a Polluted Subtropical Environment: Seasonal Variation, Sources and Sinks, and Importance of Heterogeneous Processes. Environmental Science & Technology 48, 1443-1450.

Li, W., Wang, T., Zhou, S., Lee, S., Huang, Y., **Gao, Y.**, Wang, W., 2013. Microscopic Observation of Metal-Containing Particles from Chinese Continental Outflow Observed from a Non-Industrial Site. Environmental Science & Technology 47, 9124-9131.

Cheng, Y., Ho, K.F., Wu, W.J., Ho, S.S.H., Lee, S.C., Huang, Y., Zhang, Y.W., Yau, P.S., **Gao, Y.**, Chan, C.S., 2012. Real-time characterization of particle-bound polycyclic aromatic hydrocarbons at a heavily trafficked roadside site. Aerosol Air Qual Res 12, 1181-1188.

Cheng, Y., Yu, C.W.F., Huang, Y., Zhang, Y.W., **Gao, Y.,** Yau, P.S., Chan, C.S., Lee, S.C., 2012. Particle counts and size distributions in the roadside environment. Indoor and Built Environment 21, 633-641.

Huang, Y., Ho, S.S.H., Ho, K.F., Lee, S.C., **Gao, Y.**, Cheng, Y., Chan, C.S., 2011. Characterization of biogenic volatile organic compounds (BVOCs) in cleaning reagents and air fresheners in Hong Kong. Atmospheric Environment 45, 6191-6196.

Huang, Y., Ho, S.S.H., Ho, K.F., Lee, S.C., **Gao, Y.**, Feng, N.S.Y., 2012. Optimization of solid-phase microextraction (SPME) to determine airborne biogenic volatile organic compounds (BVOCs): An application for measurement of household cleaning products. Analytical Methods 4, 277-283.

Huang, Y., Lee, S.C., Ho, K.F., Ho, S.S.H., Cao, N., Cheng, Y., **Gao, Y.,** 2012. Effect of ammonia on ozone-initiated formation of indoor secondary products with emissions from cleaning products. Atmospheric Environment 59, 224-231.

International conference paper

Gao Y., Lee S.C. 2014. Influence of regional pollution outflow on the concentration of black carbon in the coastal area of southern China. European Geosciences Union General Assembly, Vienna, Austria, 27 April-02 May, 2014.

Gao Y., Lee S.C., 2013. Size-resolved Particles at an Urban Site in Hong Kong during Winter Period: Chemical Characteristics and Optical Properties. The 11th aerosol conference, Ilan, Taiwan, 23-29 October, 2013.

Acknowledgements

I express my thanks to my supervisor, Prof. S.C. Lee, for his guidance and mentoring. He encouraged this research and facilitated my growth as a research scientist. My dissertation committee members provided constructive criticism and advice. My co-supervisor, Prof. T. Wang, provided valuable support and comments. Without the technical support of Mr. W.F. Tam for analysis instrument for this study would be unachievable. Drs. J.C. Chow, J.G. Watson, S.C. Lai, Y. Cheng, Y. Huang, K.F. Ho, and P.K.K. Louie assisted in the review and revision of published papers as well as their thesis. The Hong Kong Polytechnic University provided this Ph.D. opportunity with essential financial support.

Thanks to all of my friends who always supported me during the many challenges that were met to achieve this goal. Finally, special thanks to my family. Words cannot express how grateful I am to my father and mother for the sacrifices they made on my behalf. Their love and support made it possible for me to go further than anyone thought possible.

Table of Contents

List of Figures

List of Tables

Chapter 1. Introduction

1.1 General background and the objectives of the study

Poor visibility concerns citizens with adverse health effects, affects tourism, and lowers quality of life. On a global scale, visibility-reducing particles disturb the Earth's radiation balance and indirectly affect cloud formation, contributing to climate change (Bohren and Huffman, 2008; Rosenfeld, 1999; Yan et al., 2008). Visibility impairment results from scattering and absorption of solar radiation by gases and particles (Tao et al., 2009; Watson, 2002). Meteorological conditions (i.e. relative humidity, wind speed) affect particle transport and the growth of particles into size ranges that more efficiently scatter light.

Low visibility days in Hong Kong started to increase significantly since 2000 (HKO, 2015), which challenges the Hong Kong Special Administrative Region (HKSAR) government to make improvements. Suspended particulate matter (PM), and their chemical constituents are the most important to visibility degradation, but some of these particles are formed by emitted gases, such as oxides of nitrogen (NO_x), sulfur dioxide (SO_2) and ammonia (NH_3).

In past studies, Chang and Koo (1986), Cheung et al. (2005), Lai and Sequeira (2001), Lee and Sequeira (2002), Man and Shih (2001), Sequeira and Lai (1998), Wang et al., (2003) found that meteorological factors, especially relative humidity (RH) along with PM composed of ammonium sulfate ($(NH_4)_2SO_4$), organic carbon (OC), elemental carbon (EC) and ammonium nitrate (NH_4NO_3) are important

factors related to light scattering and absorption. These studies have applied theoretical, partial scattering measurement, and multi-linear regression (MLR) methods (Lowenthal and Kumar, 2006; Lowenthal and Kumar, 2004; Malm and Pitchford, 1997; Sloane, 1986, Hand and Malm, 2007). The U.S. Interagency Monitoring of Protected Visual Environments (IMPROVE) chemical extinction formula (Pitchford et al., 2007) has been widely applied.

No studies have developed a chemical extinction equation specific to the Hong Kong situation. PM_{10} and $PM_{2.5}$ (mass of PM < 10 μm and 2.5 μm) are most commonly measured with $PM_{2.5}$ accounting of > 70% of particle extinction in Hong Kong and the PRD region (Wang et al., 2003; Deng et al., 2008). Therefore, the aims of this study are:

a) to identify particle optical properties in Hong Kong, including particle light scattering, light absorption, single scattering albedo and scattering and absorption Angstrom exponents;
b) to determine chemical characteristics of size-resolved PM in Hong Kong;
c) to quantify relationships between chemical characteristics of particulate matters (PM) and optical properties;
d) to evaluate chemical extinction equations for Hong Kong; and
e) to identify emission source contributions to local visibility degradation by using the positive matrix factorization (PMF) solution to Chemical Mass Balance (CMB) equations.

1.2 Roadmap

Chapter 1 gives the overview information and the objectives of the study. Chapter 2 provides background information on particle optical properties, particle size distributions, and a review of previous studies. Chapter 3 introduces the methodology and explains the instrumentation, analysis methods, calculations, and modeling. Chapter 4 presents PM properties in Hong Kong, including particle light scattering, light absorption, single scattering albedo, and absorption/scattering angstrom exponent. Chapter 5 discusses particle size distributions and their chemical characteristics. Chapter 6 evaluates chemical extinction equations and develops a Hong Kong specific equation. Chapter 7 estimates source contributions to visibility impairment. Chapter 8 summarizes results. Finally, Chapter 9 evaluates the significance and limitations of this work.

Chapter 2. Literature Review

2.1 Overview of visibility degradation

2.1.1 Visibility degradation and light extinction coefficient

Visual range (VR), in meteorology, is the maximum distance where an object can be discerned from the background. VR originated as an aid to light safety, and it is visually reported at airport weather stations. In a particle free atmospheric environment, the visual range is estimated to be 296 km, owing scattering by air molecules (Malm, 1999). The light extinction coefficient (B_{ext}, Unit in Mm^{-1}) is used to describe the light attenuation through a medium (equation 2.1).

$$\frac{I_x}{I_o} = e^{-Bext,x} \qquad (2.1)$$

Where: I_o = light intensity at a target

I_x = light intensity at observation distance x,

x = distance between target and observer

It provides the equation for light extinction calculation related to visibility and Koschmeider factor,

$$B_{ext} = \frac{\mathrm{K}}{\mathrm{VR}} \qquad (2.2)$$

Where: K is Koschmeider factor (~3.9, for accounted limit of 0.02)

VR the visual range (km)

Depending on the measurement methods for VR and B_{ext}, K value ranges from 1.6 to 2.9. Previously K = 2.6 was calculated for Hong Kong (Wang et al., 2003).

B_{ext}, can be expressed as a summation of particle and gases scattering and absorption.

$$B_{ext}=B_{sp}+B_{ap}+B_{sg}+B_{ag} \qquad (2.3)$$

Where: B_{sp} is light scattering by particles,

B_{ap} is light absorption by particles,

B_{sg} is light scattering by gases

B_{ag} is light absorption by gases

The B_{sg} is a constant due to Rayleigh scattering, which is proportional to air density, with a value of ~13 Mm^{-1}, for above sea level at wavelength of 520 nm (Seinfeld and Pandis, 2006). Nitrogen dioxide (NO_2) is the only important

contributor to B_{ag} and is highly wavelength dependent. NO_2 plumes have red, brown or yellow colours (Seinfeld and Pandis, 2006). Based on the result of IMPROVE study, the NO_2 absorption efficiency is 0.33 at 520 nm. B_{sg} + B_{ag} constitutes a small fraction of B_{ext}, ~ 4-10% (Groblicki et al., 1981). Particle scattering and absorption are the major contributors to light extinction with the largest contributor from B_{sp}.

Particles with diameters similar to visible light wavelengths (400 nm to 700 nm) effectively scatter solar radiation, part of which goes back into the space. This reduces the incoming solar radiation energy and results in cooling at the Earth's surface. Some PM chemical components, black and brown carbon absorb solar radiation acting like Green House Gas (GHGs), resulting in warming of the Earth's surface (Seinfeld and Pandis, 2006).

VR by human observation has the longest history of visibility impairment study (Watson, 2002). Among the more precise visibility measurements and methodologies, as summarized in Table 2.1, the Transmissometer and Photoacoustic extinctiometer directly measure B_{ext} and have higher time resolution. Particle B_{ext} is the sum of B_{sp} and B_{ap} value and detailed description on B_{sp} methodology is summarized in Table 2.1.

2.1.2 Single scattering albedo and angstrom exponent

The single scattering albedo (SSA) is the ratio of scattering to the total extinction coefficient, (B_{sp}/B_{ext}), and is an indicator of particle cooling or heating effects

(Hyvärinen et al., 2009). SSA depends on the particle composition, which influenced by combustion efficiency and secondary aerosol formation. Flaming bush combustion showed an SSA of ~0.3, similar that of kerosene and diesel soot, but pine and duff combustion yielded SSAs of 0.9-1.0 (Paredes-Miranda et al., 2009). Dubovik et al., (2002) found mean SSA in the northern hemisphere of 0.85-0.95, as derived from the Aerosol Robotic Network (AERONET). Tables 2.2 summarize SSA values measured at different location. Rural sites in China and U.S. have SSA values of 0.85-0.95, while SSA values at urban sites (i.e. China, India, Spain) are lower.

The scattering Angstrom exponent (α_s) describes the wavelength dependence of B_{sp} and α_s is related with particle size. Value of α_s higher than 1 indicated fine particles dominated and the value lower than 1, coarse particles was predominated. Yang et al., (2009) associated source types with α_s, with values of α_s 0.59 is from coarse fugitive dust, α_s of 1.52 for fine particle biomass burning, α_s 1.49 for and urban plume, and 1.39 from coal combustion. Sea salt showed α_s value of 1.2, at a Mediterranean coastal site (Esteve et al., 2012). α_s has not been estimated for Hong Kong and the PRD region.

The absorption angstrom exponent (α_a) relate B_{ap} to λ, with $B_{ap}(\lambda)\ \lambda^{-\alpha a}$. The black carbon α_a equals 1, $\alpha_a \approx 1$, for engine exhaust and flaming biomass. For smoldering biomass, α_a increases to ~2, with flaming and smoldering biomass having value of 1-2 (Hyvärinen et al., 2009). Light absorbing particle not only contains black carbon, soot from incomplete combustion, but also mineral dusts, some organic compounds. $\alpha_a > 1$ is an indicator for these brown-BC absorbers. Zhang et al., (2013) found α_a ranging from 3.2 to 7.6 in California's South Coast Air Basin (SOCAB),

indicating light-absorbing organic compounds. Brown carbon properties and potential visibility impacts remain poorly understood.

2.2 Chemical characteristics of atmospheric particles

2.2.1 Particle size

Atmospheric PM have aerodynamic diameters ranging from 0.002 to 50 μm. Large size particles (> 10 μm) deposit to the surface within minutes to hours after release, depending on their injection height. The smallest particles diffuse rapidly to surfaces, or combine with each other or large particle (Finlayson-Pitts and Pitts Jr, 1999). Atmospheric particles have different shapes, but in recent visibility research, atmospheric shapes are often assumed to be spherical. Several types of particles diameter are used, e.g. aerodynamic diameter (D_a), geometric diameter (D_g) and Stokes diameter (D_s). D_a defined as the equivalent diameter of a spherical particle with 1 g/cm^3 density that has the same settling velocity in air, which reflects the particle residence time in the air and deposit area in human respiratory system; $D_g = \frac{D_a}{\sqrt{\rho_p}}$, where ρ_p is the particle density. Stoke diameter, D_s, represents the diameter, D_a, that has been adjusted with slip correction factor (according to this diameter) at the particle's terminal settling velocity and density (Flagan and Seinfeld, 1988).

PM sources include natural emitters (i.e. pollen, geological material) and anthropogenic sources (i.e. industrial process, biomass burning, engine exhaust,

fugitive dust, and secondary aerosol). Gaseous emissions are important, as they connect to solid and liquid particles upon atmospheric oxidation (Seinfeld and Pandis, 2006). PM often fall into one of three size modes: the ultrafine mode, the accumulation mode and the coarse mode, with size ranges of < 0.1 μm, 0.1 to 2 μm and 2-100 μm, respectively (Kannosto et al., 2008; Watson, 2002; Whitby and Sverdrup, 1980). Figure 2.1 illustrate these size modes with their origins and residence times. Ultrafine particles are usually observed in fresh emissions very close to the emission source. They have short residence times, low scattering efficiencies and low mass concentrations. Ultrafine particles have less effect on the local/regional visibility, although they may penetrate into the deep lung cross cellular membranes and even directly enter the circulatory system (Geiser et al., 2005). Ultrafine number concentrations decrease as these particles coagulate with each other, or evaporate and re-condense onto accumulation mode particles. Accumulation mode particles are formed via coagulation and condensation processes. Accumulation mode particles have the longest residence time compared with particles of other sizes. Since accumulation-mode particles have sizes similar to visible light wavelengths (300-700 nm), they have the highest particle mass scattering efficiencies and the highest impacts on regional and local visibility degradation. Two sub-modes are found within the accumulation size range, refers the condensation (0.1 to 0.5 μm) and the droplet (0.5 to 2 μm) mode. The condensation mode results from gas-phase oxidation while the droplet mode results from aqueous-phase chemistry within water droplets (Hering and Friedlander, 1982; John et al., 1990; Meng and Seinfeld, 1994). Anthropogenic source contribution dominated these sub-modes, including secondary sulfates, nitrates, organics as well as primary organic carbon, elemental carbon, and mineral/industrial related

elements. Coarse particles are dominated by geological materials, pollen, spores and sea salt near coastal sites. Fugitive dust from material handling, paved and unpaved roads and disturbed soils dominate the coarse mode. PM in the coarse mode persist force few hours up to one or two days, due to gravitational settling (Finlayson-Pitts and Pitts Jr, 1999). In recognition of particulate matter and public health impact, the World Health Organization (WHO), U.S. EPA and China have established PM_{10} and $PM_{2.5}$ standards to regulate the different size ranger (Cao et al., 2013). Respirable suspended particulate (RSP) is another form for PM_{10}, means suspended particles in the air with a nominal aerodynamic diameter of 10 μm or less. Fine suspended particulate ($PM_{2.5}$) refers to particle with $D_a < 2.5$ μm. $PM_{2.5}$ has the greatest effect on visibility (Watson, 2002) and has been widely associated with mortality and morbidity (Pope and Dockery, 2006).

2.2.2 Particle sampling

Size-segregated particles can be collected by impactors, cyclones, aerosol centrifuges, etc. Size-selective inertial impactors are used to define D_a (Jones et al., 1983; Marple et al., 1991). Particle suspended in an air jet encounter an impactor plate on which the large particles are collected. Smaller particles with lower interim follow the airflow to the next impaction plate, when the impactor plates are concerned with a removal sampling media, the deposit can be analyzed for chemical components (Hering, 1995). These impactors can separate particle into size bins ranging from 0.005 μm to 100 μm. The Andersen Cascade Impactor (ACI) and the Micro-orifice Uniform Deposit Impactor (MOUDI) are in common use.

Each impactor stage is characterized by a 50% D_a, cut point (D_{50}). At D_{50}, half the particles are removed, and the other half remain entrained in the air stream leading to the next stage. The ACI has several versions: 1) 4-stage cascade impactor with size bins (defined by D_{50}) of >7.0 μm, 3.3~7.0 μm, 2.0~3.3 μm and 1.1~2.0 μm; 2) 6-stage cascade impactor with size bins of >7.0 μm, 4.7~7.0 μm, 3.3~4.7 μm, 2.1~3.3 μm, 1.1~2.1 μm and 0.65~1.1 μm; and 3) 8-stage cascade impactor with size bins of >11 μm, 7.0~11 μm, 4.7~7.0 μm, 3.3~4.7 μm, 2.1~3.3 μm, 1.1~2.1 μm, 0.65~1.1 μm and 0.43~0.65 μm (Flesch et al., 1967; Vaughan, 1989). Wide size range (from 18 μm to 0.018 μm, even up to 10 nm) and uniform deposited particle can be collected by MOUDI. The MOUDI impaction plates are rotated to provide uniform deposit on the substrate, rather than the individual spots for the ACI, which are more amended to chemical analysis (Marple et al., 1991). The MOUDI stages are: 0.010, 0.018, 0.032, 0.056, 0.1, 0.18, 0.32, 0.56, 1.0, 3.2, 5.6, 1.8, 10 and 18 μm.

2.2.3 Size distribution inversion

Owing to difference in the shapes of impactor sampling effectiveness curves, a more accurate derivation of the size distribution is obtained by an inversion method (Dzubay and Hasan, 1990).

Inversions assume a super position of log-normal distributions. The main difference between a normal distribution and a log-normal distribution is that the normal is addictive and the log-normal is multiplicative (Limpert et al., 2001). The

triangle shapes of the normal distribution are isosceles nor of log-normal distribution. The function of normal distribution is given by equation (2.4),

$$f(x) = \frac{M}{\sqrt[2]{2\pi} \times \sigma_x} \times e^{\left(-\frac{(x-\overline{x})^2}{2{\sigma_x}^2}\right)} \quad (2.4)$$

Where, $\overline{x}$ is mean of distribution, σ_x is standard deviation, (the width of the distribution). However, the function of x is natural logarithms (ln(x)) and have normal distribution pattern, which assume to be log-normal distribution. The lognormal distribution is:

$$f(\ln(x)) = \frac{M}{\sqrt[2]{2\pi} \times \ln(\sigma_x)} \times e^{\left(-\frac{(\ln(x)-\ln(\overline{x}))^2}{2(ln\sigma_x)^2}\right)} \quad (2.5)$$

The particle size distribution based on the equation 2.5, is provided in equation (2.6), where N is the number of particles and $\ln D_a$ and $\ln D_a$ $d\ln D_a$,

$$\frac{dN}{dlnD_a} = \frac{N}{\sqrt[2]{2\pi} \times \ln(\sigma_{D_a})} \times e^{\left(-\frac{(\ln(D_a)-\ln(\overline{D_a}))^2}{2(ln\sigma_{D_a})^2}\right)} \quad (2.6)$$

$\overline{D_a}$ is the geometric mean diameter for N number diameter. Equation (2.6) expresses a single modal particle size distribution, but most of ambient particle superimpose several distributions (Figure 2.1). The multimodal lognormal distribution approach becomes a necessary solution. Twomey inversion method is one of the acceptable inversion algorithms, which is based on the same theory with multimodal log normal size distribution method (Twomey, 1975; Winklmayr et al., 1990). The expression for the multi-modal lognormal distribution is below:

$$M_i = \frac{M_t \int_0^\infty f(D) E_i(D) \prod_{j=0}^{i-1} [1 - E_i\ (D)] dD}{\int_0^\infty f(D) [1 - E_0\ (D)] dD} \qquad (2.7)$$

Where, f(D) is lognormal distribution function (equation 2.7). If the ambient particle has three size modes, $f(D) = k_1 \times f_1(D) + k_2 \times f_2(D) + k_3 \times f_3(D)$, and $k_1 + k_2 + k_3 = 1$, where each k is the fraction of the total mass in each mode. The inversion involves solution for k_i, D_i and σ_i based on a least squares minimization, χ^2 (Dzubay and Hasan, 1990).

2.2.4 Particle components and sources

Particle size distribution in the troposphere shows diversified patterns site by site; particle chemical compositions are also different via varied particle size, emission sources and site circumstance. In general, fine particles are formed from combustion, heterogeneous process, homogeneous nucleation, condensation,

coagulation process. Final particles include four major chemical components: water-soluble ions (e.g., sulfate, nitrate), carbonaceous materials (elemental carbon and organic carbon), soil dust, and sea salt. Soil dust and sea salt materials are the typical chemical component in coarse particle, around 20-80% and only 5-10% was found in fine particles (Seinfeld and Pandis, 2006). To understand their formation mechanism is essential for making pollution control plans.

Sulfate (SO_4^{2-})

Figure 2.2 illustrates sulfate formation pathways. Sulfate is a common species formed in rural and urban areas (Sheridan et al., 1994). Most of the SO_4^{2-} derives from atmospheric oxidation of SO_2. Volcanoes, residual oil combustion and coal combustion are the major SO_2 sources (Seinfeld and Pandis, 2006). Major oxidants include the OH radical, O_3, H_2O_2 and O_2. SO_4^{2-} size distributions differ by formation mechanism (Figure 2.2). Secondary ultrafine and condensation SO_4^{2-} is formed by homogeneous reactions between SO_2 and OH radicals to form sulfuric acid (H_2SO_4). H_2SO_4 is hygroscopic, and the size increases with humidity. NH_3 neutralizes H_2SO_4, so most SO_4^{2-} exists as $(NH_4)_2SO_4$ and NH_4HSO_4. Ultrafine $(NH_4)_2SO_4$ and NH_4HSO_4 particles have further condensation and coagulate to increase particle size (Yao and Zhang, 2011). SO_2 diffuses into fog and cloud droplets, where HSO_3^- is formed, which reacts with hydrogen peroxide (H_2O_2), ozone (O_3) to form H_2SO_4. The large droplet mode SO_4^{2-} results when the larger cloud or fog droplet evaporates. From the U.S. IMPROVE chemical budget extinction equation assumes that $(NH_4)_2SO_4$ is one of the key chemical contributors to visibility degradation. The multiplicative molar correction factor (mcf) used to $(NH_4)_2SO_4$ from SO_4^{2-} is 1.375 (Chow et al., 2015; Malm et al., 1994).

Nitrate (NO_3^-)

Figure 2.3 illustrates PM nitrate formation pathways. Ammonium nitrate (NH_4NO_3) is the main form of NO_3^- particles, but NH_4NO_3 is equilibrium with NH_3 and HNO_3 gases (Schryer, 1982). Lower temperature (< 15 ^oC) and higher humidity (RH > 70%) favor the PM phase. HNO_3 results from oxidation of NO and NO_2. Natural sources of NO_x are soil and lightening. Most of the NO_x derives from fossil fuel combustion and biomass burning with power plants and motor traffic as major sources. When NH_3 is abundant, HNO_3 is combing with NH_3 to form NH_4NO_3 (Pathak et al., 2009). The derived NH_4NO_3 is from NO_3^- (mcf - molar correction factor is 1.29), which assumes that HNO_3 is neutralized by NH_3 (Chow et al., 2015; Malm, 1999; Malm et al., 1994). HNO_3 can also react with sea salt or soil dust to form $NaNO_3$ or $Ca(NO_3)_2$ in the coarse mode (De Haan and Finlayson-Pitts, 1997; Goodman et al., 2000). In addition to daytime photochemistry, HNO_3 also forms at night via N_2O_5 and HONO related reactions (Gerecke et al., 1998).

Carbonaceous materials

Carbonaceous materials consist of organic compounds and black non-volatile materials (Gray et al., 1986). Organic compounds usually are represented by organic carbon (OC) measurements and result from combustion as well as the oxidation of volatile organic compounds (VOCs) (Bond et al., 2004). PM OC results from both primary emission and secondary gaseous precursors and contains hundreds compounds, usually with more than 20 carbon atoms couple to oxygen and hydrogen atoms (Schauer et al. 1996; Reisen and Arey, 2005). Carbon can contribute around 20-30% of particle light extinction value (Kim et al., 2006; Wang et al., 2003). Organic matter (OM) is derived from OC using a mcf that depends on

amount of oxygen incorporated in the organic molecules, varies from 1.1 to 2.2 (Bond et al., 2013; Russell, 2003). The soot from combustion is termed black carbon (BC) when derived from B_{ap} measurement and elemental carbon (EC) when derived from physical measurement. EC and BC are highly corrected but their comparability depends on the measurement methods (Watson et al., 2005). BC dominates B_{ap} and affects the Earth's radiation budget (Gray et al., 1986; Bond et al., 2013; Solomon, 2007). Global-scale of BC emissions from 2000 were estimated at 1690 Gg/year for Africa, 1550 Gg/year for East Asia (Bond et al., 2007). East Asian economic development increased BC emissions from industrial, traffic and residential sources (Bond et al., 2004; 2007; 2013; Chow et al., 2011; Lamarque et al., 2010). The U.S. EPA national BC/EC emission inventory shows that 80% of total BC/EC originates from biomass burning and mobile sources (Chow et al., 2015).

Sea salt

Sea salt particles are abundant in the marine environment and commonly found in coastal areas. In general, sea water contains 57% of Cl^- and 32% of Na^+ (Seinfeld and Pandis, 2006). Near coastal areas, sea salt (NaCl) can have further reaction with NO_3^- or SO_4^{2-} to release Cl^- and become an important species to participate the atmospheric sulfur, nitrogen cycle (Chameides and Stelson, 1992). In the revised U.S. IMPROVE chemical extinction budget equation, sea salt has been added into the equation showing its significance in visibility degradation (Pitchford et al., 2007; Tang et al., 1997). The molar weight ratio of Cl^- and Na^+ is 1.8 and sea salt is estimated as $1.8 \times Cl^-$ (Lowenthal and Kumar, 2006).

Soil dust

Soil-related minerals are oxides of Al, Si, Ca, Ti and Fe. Chow et al. (2015) have summarized various weighting approaches, with the IMPROVE equation using 2.2×Al + 2.49×Si + 1.63×Ca + 2.42×Fe + 1.94×Ti.

2.3 Calculation and modeling

2.3.1 The Positive Matrix Factorization (PMF) receptor model solution to the Chemical Mass Balance (CMB) equations

Receptor models intend to quantify source contributions by demonstrating mixtures of chemical components in source profiles (Watson, 2002). The first factor models were used to estimate specific sources of pollutant in the atmosphere pronounced in 1970's (Hopke et al., 1976). More recently, the Positive matrix factorization (PMF) solution to the Chemical Mass Balance model (PMF-CMB) has been used for source apportionment (Crilley et al., 2015; Huang et al., 2009; Kim et al., 2003; Paatero and Tapper, 1994; Lee et al., 1999). The PMF solution imposes non-negativity constraints while minimizing the squared difference between calculated and measured chemical concentrations. Lee et al., (1999) applied the PMF-CMB to respirable suspended particulate (RSP) in Hong Kong, finding source factors related to sulfate, non-ferrous smelters, particulate copper, fuel oil combustion, vehicular exhaust and road dust. The species Al, Ca, Mg, Pb, Na^+, V, Cl^-, NH_4^+, SO_4^{2-}, Br^-, Mn, Fe, Ni, Zn, Cd, K^+, Ba, Cu and As concentrations served as PMF-CMB input. Kim et al., (2003) applied the PMF solution to size-

resolved chemical concentrations in Gosan area, Korea, while Crilley et al., (2015) applied PMF to identify sources of carbonaceous materials in London, UK.

2.3.2 Cluster and CWT model

Source types and origin location was usually identified by receptor models. To know sources types, the tracers are the key components for the source type identification, such as PMF model. In order to know the origin location, hybrid models with trajectory winds may be used. The cluster analysis technique assists understanding of source related to different air transport patterns. Back-trajectories calculated from the measurement sites are clustered into ten categories (Dumka et al., 2013). Cluster analysis intends to reduce the uncertainty among trajectories within a cluster (Gogoi et al., 2009).

Concentration weighted trajectory (CWT) analysis is applied to designate for individual pollutants or PMF-derived source factors. Each grid cell gets a weighted concentration by averaging receptor concentrations when the related trajectories pass through the grid cell (Vinoj et al., 2010). The CWT analysis could improve the limitation of potential source contribution function (PSCF) method for the potential source region identification. CWT analysis has been developed more recently and the method is more accurate than the PSCF as it shows the spatial pattern of the potential sources of particles at the receptor site (Liu et al., 2013; Wang et al., 2004).

2.3.3 Mass scattering and absorption efficiency

Based on the relationship between particle diameter and incident wavelength, particle scattering can be divided into Rayleigh scattering (particle diameter is much smaller than incident wavelength), Mie scattering (particle diameter size is similar to the incident wavelengths) and Geometric scattering (particle diameter size is much larger than the incident wavelengths). Solar radiation from Rayleigh scattering is small for PM, being dominated by Mg and O_2 atoms. Since most of particles are in the range of 0.01 μm to 10 μm, similar to the wavelength of visible light (290 nm to 750 nm), most of Mie theory applies scattering activities (Seinfeld and Pandis, 2006). Mathematical methods to calculate particle B_{ext} (B_{sp} + B_{ap}) provides higher precision for spherical particle with known size distribution patterns. Equation 2.8 shows particle B_{ext} calculation via Mie theory (Bohren and Huffman, 2008).

$$B_{ext} = \int_0^{D_p^{max}} Q_{ext}\left(D_p, \lambda, m\right) n_M\left(D_p\right) dD_p \qquad (2.8)$$

Where: D_p^{max} is an upper limit diameter for the particle population (μm),

$Q_{ext}(D_p, \lambda, m)$ is the extinction cross section (m^2)

$n_M(D_p)$ is the particle number (#/m^3) with diameter D_p

λ is the wavelength of the light (nm)

m is the refractive index of the particle

B_{ext} can be summed into B_{sp} and B_{ap}, the equation can be written as:

$$B_{ext} = \int_0^{D_p^{max}} Q_{scat}(D_p, \lambda, m) n_M(D_p) dD_p + \int_0^{D_p^{max}} Q_{abs}(D_p, \lambda, m) n_M(D_p) dD_p \quad (2.9)$$

Where: D_p^{max} is an upper limit diameter for the particle population (μm),

Q_{scat} (D_p,λ ,m) is the scattering cross section (m^2)

Q_{abs} (D_p,λ ,m) is the absorption cross section (m^2)

$n_M(D_p)$ is the particle number with diameter D_p (#/m^3)

λ is the wavelength of the light (nm)

m is the refractive index of the particle

Based on the Mie theory (Mie, 1908), the particle extinction is estimated from particle number distribution/mass distribution, cross section/mass scattering (absorption) efficiency and incident wavelength. Therefore, the calculation should include different chemical components to have further calculation. The major particles components contribute to light scattering coefficient and light absorption coefficient are sulfate, organic carbon, nitrate and black carbon (soot).

Mass scattering/absorption efficiencies cannot be directly measured from instrument, which should be calculated from particle optical properties and particle

chemical species. There are two methods to compute mass scattering efficiencies, a theoretical method and a multi-linear regression method (Hand et al., 2007). Different particle size will contribute varied scattering intensity. The theoretical method (equation 2.7) for determination mass scattering efficiency is from particle size distribution pattern and the optical cross section based on Mie theory and a function of refractive index, particle diameter.

Mass scattering efficiency, $MSE = \frac{3Q}{2D\rho}$ *(2.10)*

$Q = \frac{4\sigma}{\pi D^2}$ *(2.11)*

Where, σ is the cross section corresponding to a specific chemical species and Q is the scattering efficiency (Sloane, 1986). The result on this method is more accurately than other methods, but the major disadvantage is that need to have more intensive analytical size distribution measurements.

The MLR method estimates efficiencies by fitting nephelometer or transmsometers measured of B_{sp} or B_{ext} for species mass concentrations (Hand and Malm, 2007), i.e. ammonium sulfate, ammonium nitrate, particle organic matters, soil dust, sea salt and coarse mode mass.

Mass scattering efficiency, $\mathrm{MSE} = \frac{B_{sp}}{\mathrm{M}}$ *(2.12)*

B_{sp} is light scattering coefficient measured from nephelometer or transmometers, and M is the mass concentration on different species.

2.4 Previous studies of particles and visibility degradation

The most comprehensive visibility network is the U. S. Interagency Monitoring of Protected Visual Environments network (IMPROVE) with objectives to aim to: 1) establish relationships between visibility degradation and atmospheric particles in U.S. 2) determine the contribution of anthropogenic emissions on local visibility degradation; 3) assess the long-term change in visibility levels and 4) determine reasonable progress toward natural visibility conditions. Ammonium sulfate (AS), ammonium nitrate (AN), particle organic matter (POM), elemental carbon (EC) and soil dust (SD) are the major contributors to particle extinction (Hand and Malm, 2007). The IMPROVE MSE was computed via theoretical method based on Mie theory, which have two versions, one was published in 2003 and the updated version have been published in 2007. Since the method was calculated based on the United State IMPROVE site, there are many similar studies were conducted in China. Because Chinese PM level and compositions differ from those in the U.S. and other European countries, IMPROVE MSE may not apply. Table 2.3 summarizes the value of MSEs of fine particles, ammonium sulfate, ammonium nitrate, particle organic matters, sea salt, and soil dust for different places. Lower values for ammonium sulfate MSEs are observed in clean condition, e.g. 2 m^2/g in Ocean/Marine area. But the relative low value of ammonium nitrate is in urban area rather than remote area, usually average MSE for ammonium nitrate is 2.7 m^2/g in

non-urban area and 2.2 m^2/g in urban area. For OM, a higher value is found in industrial and biomass burning influence areas, for example ~6 m^2/g observed in Bondville, IL, US (Hand and Malm, 2007).

Hong Kong is located in southern China (114°15 E, 22°13 N). Its climate is governed by the East Asian monsoons. Wind fields vary by seasons and bring different air masses to the PRD. In summer, the southwesterly winds prevail, bringing warm and damp marine air masses. In fall and winter, flows are dominated by northwesterly winds, bringing cool and dry air masses (Ho, 2003). In these seasons, transport is from mainland China continent. In spring, wind directions change from northwesterly to southwesterly, with elevated fluxes of mainland pollution. Examination of 52 years of visual range observation in Guangzhou found that the hazy days increased during 2001-2009. Industrial development in the PRD region (GDP increased 280%) engendered higher emissions. More than 100 hazy days were observed during 2004-2008 and average daily $PM_{2.5}$ concentrations were as high as 250 $\mu g/m^3$ (Deng et al., 2008). Visual range observation in Hong Kong dated from 1969 showing urban visibility was poorer than rural visibility for 1969 to 1982 (Chang and Koo, 1986). The number of hazy days per year in Hong Kong peaked in 2004 and 2005, based on the Hong Kong long term visibility monitoring. In 1983, Hong Kong Environmental Protection Department (HKEPD) established air quality monitoring station networks, which started to provide comprehensive information on air pollution problems to public. Particle light scattering and absorption have been monitored to determine seasonal variations with large variances among seasons (Man and Shih, 2001). Maximum B_{ext} values were 5-fold larger than U.S. rural values, comparable to other rural area on the mainland.

Sequeira and Lai, (1998) sought the factors responsible for the visibility degradation in Hong Kong. Lee and Sequeira (2001) used a linear multivariate model to identify contributions from respirable suspended particles (RSP) and NO_2 to B_{ext} at urban site (Lai and Sequeira, 2001). They found that RSP contributed 63% and NO_2 17% of B_{ext}.

Since 1997, fine particle ($PM_{2.5}$) and RSP (PM_{10}) mass concentrations together with chemical speciation data have been available from the HK monitoring stations. The chemically speciated data illustrated that 80% of PM_{10} is $PM_{2.5}$, with carbonaceous material, water-soluble sulfate, nitrate and ammonium as the major chemical components (Cheng, 2007; Louie et al., 2005). Chemical extinction was estimated by Wang et al., (2003) and Cheung et al., (2005). Cheung et al., (2005) used U.S. IMPROVE chemical extinction formula to estimate ammonium sulfate (45% to 70%) and particle organic matters (22% to 44%) contributions. Wang T. (2003) applied the MLR method to estimate MSEs for ammonium sulfate (4.16 m^2/g), ammonium nitrate (2.97 m^2/g), organic matter (3.18 m^2/g), elemental carbon (8.28 m^2/g) and soil dust (6.7 m^2/g). These MSEs differed from those of the IMPROVE formula, especially for soil dust (1 m^2/g) in IMPROVE MSEs varied by location. MLR is limited, however, owing to the need for many sample as well as inter-correlations among variables. Sample sets give different MSEs. Theoretical methods better simulate mass scattering efficiencies for each chemical species. Cheng et al., (2015) have applied a theoretical method to determine mass scattering efficiency for ammonium sulfate, ammonium nitrate, and particle organic matters in Shanghai by using size-resolved particle measurement.

Size-resolved particle studies have been conducted in Hong Kong since 1999. Zhuang et al., (1999b) used Mirco-Orifice Uniform Deposit Impactor (MOUDI) sampler and found that sulfate, ammonium and nitrate were tri-modally distributed. Sulfate and nitrate were the dominant species in fine particles (D_p < 1.8 μm), especially for the droplet mode. Nitrate was dominant mainly in the coarse mode due to reactions of HNO_3 with sea-salt and soil dust. And also they found that chloride was depleted (74% deplete) in the marine aerosol (Yao et al., 2003b; Zhuang et al., 1999a). Elemental carbon and organic carbon showed tri-modal patterns and were dominant in the condensation and droplet modes, respectively, at a Shenzhen urban site. The Positive matrix factorization (PMF) solution was applied to find the peak size of the three modes (Lan et al., 2011). Based on the previous size-resolved data, a systematic study was conducted to determine MSEs for Hong Kong and investigate the chemical species contributions to local visibility degradation.

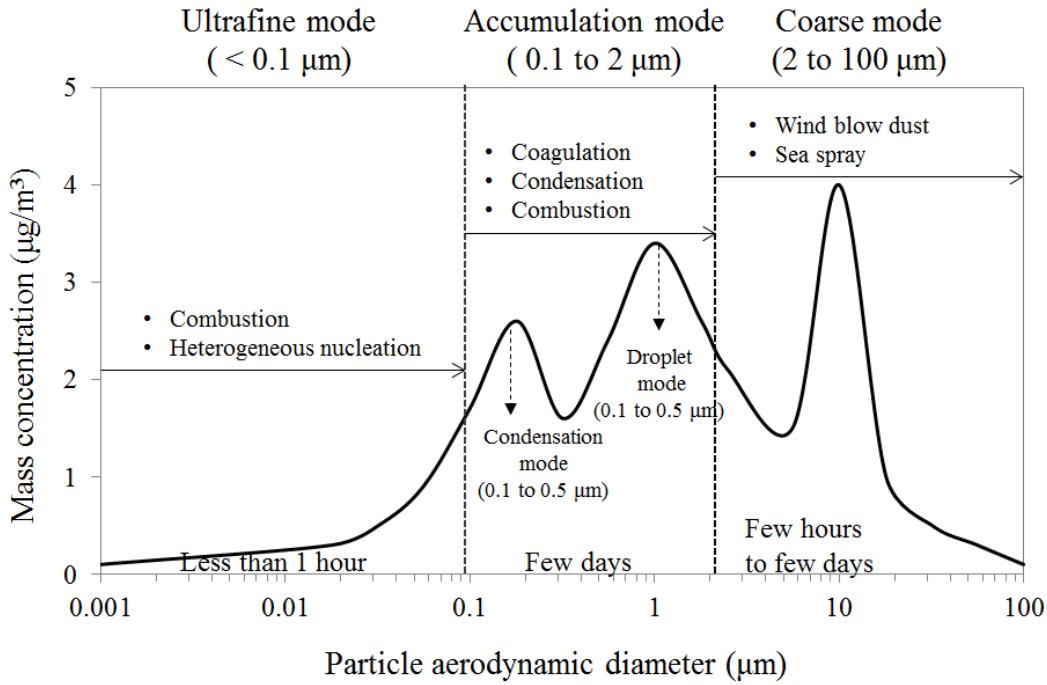

Figure 2.1 Representation of origins, residence times and sizes of particle as a function of size (Finlayson-Pitts and Pitts Jr, 1999; Watson, 2002; Willeke and Whitby, 1975)

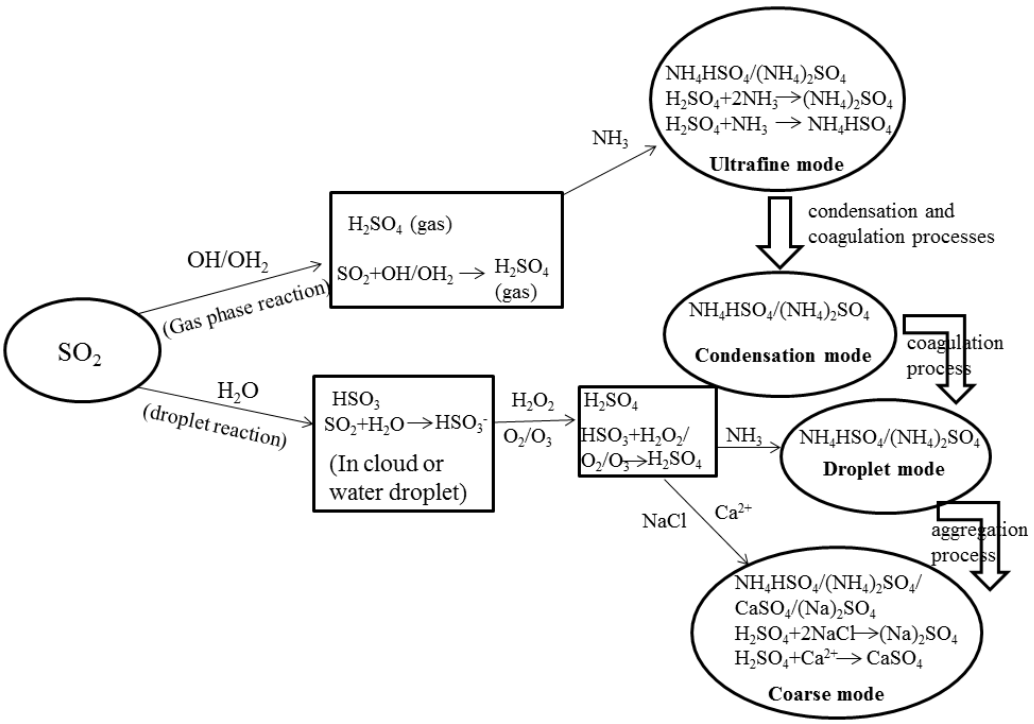

Figure 2.2 Formation pathway of secondary SO_4^{2-}

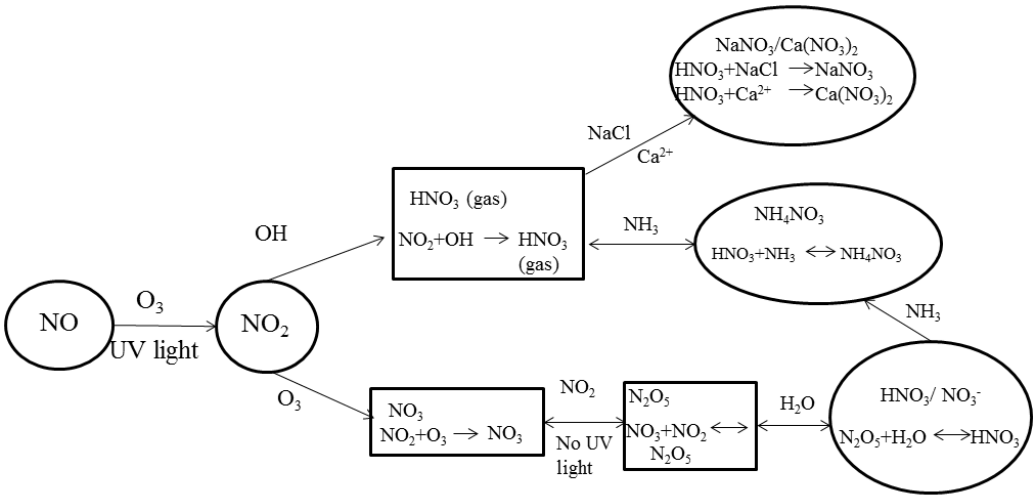

Figure 2.3 Formation pathways for secondary NO_3^-

Table 2.1 Summary of visibility metrics and methods

Instrumentation	**Measurement**	**Principle**
Human observation	Visual range (VR)	Human observation of targets at various distances from the observer, taken mostly at airport for flight safely
Transmissometer	Gas and particle light extinction (B_{ext})	Quantification of light alternation along a 1 km to 10 km slight path using a calibrated light source at one end and a detector at the other end.
DMT Photoacoustic Extinctiometer (PAX)	Particle light absorption (B_{ap})	A modulated laser heat PM suspended in a sensing volume, the heating and cooling of light absorb particle reactor a pressure wave is detected by a sensitive microphone.
Integrated Nephelometer	Particle light scattering (B_{sp})	PM in sensing volume is illuminated by a focused light beam, and scattered light is sensed by a reactor at 900 nm the incident beam
Particle Soot Absorption Photometer (PSAP)	Particle light absorption (B_{ap})	Light transmitted through a filter containing a PM deposit is composed to light transmitted through a blank filter to estimate B_{ap}

Multi-Angle Absorption photometer (MAAP)	Particle light absorption (B_{ap})	Same principle as PSAP, but using reflected light to better correct for filter scattering
Single particle soot photometer (SP2)	Particle light absorption (B_{ap})	Individual particles are heated with a laser and the absorbed light is re-emitted as black body radiation that is related to the heating caused by light absorption
Aethalometer	Particle light absorption (B_{ap})	Same principle as PSAP, but with a filter tape moved advanced when the deposit become excessive

Table 2.2 Summary of the single scattering albedo values from different areas

Site	SSA (525 nm-550 nm)	Source
Beijing, China (urban)	0.79-0.81	(Bergin et al., 2001)
US (Illinois, Alaska)	0.92-0.99	(Delene and Ogren, 2002)
Lin'an China (rural)	0.93	(Xu et al., 2004)
Yulin China (Gobi desert)	0.95	(Xu et al., 2004)
Shangdianzi, China (rural)	0.88	(Yan et al., 2008)
Xinken, China (rural)	0.83	(Cheng et al., 2008)
Guangzhou, China (urban)	0.80	(Deng et al., 2008)
Mukteshwar, India (rural)	0.75-085	(Hyvärinen et al., 2009)
Delhi, India (urban)	0.63-0.74	(Soni et al., 2010)
Southern Mexico city (urban)	0.59 (dry season) - 0.83 (wet season)	(Garcia et al., 2010)
Granada, Spain (urban)	0.71	(Titos et al., 2012)
Shanghai, China (urban, winter)	0.81	(Xu et al., 2012)

Table 2.3 Mass scattering/absorption efficiencies for PM chemicals

Mass scattering or absorption efficiency, MSE (m^2/g)	IMPROVE I (Watson, 2002)	IMPROVE II (Pitchford et al., 2007)	PRD region (Jung et al., 2009)	Guangzhou (Tao et al., 2014)	Shanghai (Cheng et al., 2015)
Ammonium sulfate scatter	3.00			2.9, 2.5, 4.8, 5.3	3.50
small mode		2.20	2.20		
large mode		4.80	3.24		
Ammonium nitrate scatter	3.00			3.2, 2.6, 4.9, 5.5	4.30
small mode		2.40	2.40		
large mode		5.10	4.47		
Particle Organic matter scatter	4.00			3.3, 2.8, 5.1, 6.2	4.50
small mode		2.80	2.80		
large mode		6.10	4.93		
Soil dust scatter	1.00	1.00	1.00		
Sea salt scatter	n.a.	1.70	1.70		
Elemental carbon absorber	10.00	10.00	7.70		
Coarse mass scatter	0.60	0.60	0.60		

Table 2.4 Summary of light scattering and absorption values for different areas

Site	Period	Scattering	Absorption	Source
		Mm^{-1}		
Beijing, China (urban)	1999.6	488	83	(Bergin et al., 2001)
US (Alaska, Illinois)	1996.9-2000.9	9.76-57.7	0.39-4.66	(Delene and Ogren, 2002)
Lin'an China (rural)	1999.11	353	23	(Xu et al., 2004)
Yulin China (Gobi desert)	2001.4	158	6	(Xu et al., 2004)
Shangdianzi, China (rural)	2003.9-2005.1	174.6	17.54	(Yan et al., 2008)
Cape D'Aguilar, Hongkong	1997.1-1998.2	8.71-64.77	6.03-25.72	(Man and Shih, 2001)
Xinken, China (rural)	2004.10-11	333	70	(Cheng et al., 2008)
Guangzhou, China (urban)	2004.10	418	91	(Andreae et al., 2008)
Mukteshwar, India (rural)	2005.9-2007.9	24.6-94.3	4.5-20.3	(Hyvärinen et al., 2009)

Tai O, Hong Kong (rural)	2002.10-12	224	22.1	(Wang T. 2003)
Southern Mexico city (urban)	2005.2-8	20.6-93.3	12.0-29.4	(Garcia et al., 2010)
Granada, Spain (urban)	2006.3-2007.2	61	24	(Titos et al., 2012)
Shanghai, China (urban, winter)	2010.12-2011.3	292.81	65.81	(Xu et al., 2012)

Chapter 3. Methodology

3.1 Sampling locations

This study was conducted at three sampling sites located in Hong Kong, including a rural site, a sub-urban site, and an urban site. The detailed description of three sites was provided below.

3.1.1 Hok Tsui (HT) - the rural sampling site

HT is a background sampling station in Hong Kong, located 60 m above mean sea level (ASL) 22.22^{o} N, 114.25^{o} E (Figure 3.1), which was established by the Hong Kong Polytechnic University. The Pacific Ocean lies from the northeast to southwest. The site is approximately 15 km from urbanized areas and had minimal anthropogenic emission impacts. Air masses could be transported from South China, the PRD region, Taiwan Island, normally less air mass pass through Hong Kong urban area. Therefore, HT was chosen to determine regional pollution effects, especially during the winter time. During the summer period, air masses often arrive from cleaner areas to the worst, although ship emission could be one of the pollution contributors.

3.1.2 Tung Chung (TC) – suburban sampling site

The TC monitoring station coordinator is on the rooftop of a health center, around 21 meters above the ground level, which is established by Hong Kong Environmental Protection Department (HKEPD). This site is on the north Coast of Lantau Island, and about 20 km far from south-west of the Hong Kong urban center. Around 3 km to the north is one of the busiest airports (Hong Kong International Airport, HKG) in the world (Figure 3.1). The TC monitoring station is influenced by local and regional emission sources.

3.1.3 The Hong Kong Polytechnic University (HKPU) – urban sampling site

The HKPU sampling site (22.30^{o} N, 114.17^{o} E) is on the rooftop of an 8-story building on the HKPU campus (Figure 3.1). It is a typical urban site in Hong Kong, which is located in a canyon of commercial and residential area, near the Victoria Harbour Tunnel, experiencing heavy traffic impacts. The site was surrounded by cooking/restaurant emissions and ship emissions from Victoria Harbor.

3.2 Measurement periods, methods and observation in three sampling locations

The detailed sampling periods, methods, and observation are summarized in Table 3.1. The field measurements cover all four seasons, except at the HKPU station, where field measurements were conducted only in the winter.

3.3 Instrumentation system

The study includes measurement of particle scattering coefficient (B_{sp}), black carbon (BC) and size-resolved particle mass concentration, atmospheric visual range, and meteorological parameters. Particle scattering coefficient (B_{sp}) was monitored by using an integrating nephelometer (Ecotech, M9003), which draws ambient air through an inlet tube and then illuminates it by LEDs at wavelength (λ) = 525 nm. The scattered light detected at angles from 7^o to 170^o is measured and integrated to yield scattering coefficient, B_{sp}. Zero check was performed every day and span check was done on a monthly basis using 99.99% pure CO_2 gas, with a scattering coefficient of 24.79 Mm^{-1} at 520 nm recommended by the manufacturer. Zero was maintained within ±1 Mm^{-1} and spans did not vary by more than ±10%. Relative humidity (RH) was monitored in the nephelometer chamber and did not exceed by 60% owing to all smart heater at the inlet that raised the air stream fem perforce when RH > 60%. This heating inlet could cause some evaporation of volatile inorganic species (nitrate) and volatile organic matter, but it was more than a few temperatures. Less than 20% of NH_4NO_3 is affected by this heating (Bergin et al. 1997) during the study period and in the study site, the nitrate is account small fraction of the total mass in fine particles. Truncation errors are negligible for $PM_{2.5}$ and less than 10% for $PM_{10\text{-}2.5}$.

The TSI Model 3563 three-wavelength (λ=450, 550, 700nm) integrating nephelometer was used at HT. This instrument draws a sample of ambient air through an inlet, illuminates it with a halogen lamp and measures the scattered light using a photomultiplier tube. The scattered light is integrated over an angular range

which can be adjusted to either 7-170^{o} or 90-170^{o} by means of a backscatter shutter. This provides the total scattering or a backscatter signal. The total B_{sp} option was used here. Measurements were made at ambient relative humidity without aerosol cut at around 15 m above the ground. Data was acquired every minute and averaged to 55 min. Zero air was measured for 5 min during each hour. The flow rate was fixed at 30 l/min. The nephelometer was calibrated monthly by using pure CO_2. The calibration data did not vary by more than ± 6%.

BC concentration was measured with an Aethalometer (Model AE 31, Magee Scientific, USA) which measures light attenuation through an aerosol deposit accumulation on a 1.6 cm portion of a quartz filter tape at 2 min. The AE31 Aethalometer measured the optical attenuation of light from LED lamps produce seven different wavelengths (370, 470, 520, 590, 660, 880 and 950 nm) so that B_{ap} is estimated across the visible, rear-on, and near IR spectrum transmitted through the aerosols deposited continuously on a quartz filter (Hansen et al. 1984). The ratio of light transmission through the particle laden sample spot and a particle free reference spot is attributed to the particle absorption. The measured B_{ap} is reported as BC after application of a mass extinction efficiency of $14625/\lambda$ m^2/g. The Aethalometer was operated at 4-5 l/min with an inlet at the top of the sampling room. In the Section 3.5, the light absorption coefficient (B_{ap}) calculation will be further discussed by using light attenuation.

3.4 Particulate matter mass and chemical composition measurements

3.4.1 Size-resolved particles sampler

Two sets of Micro-Orifice Uniform Deposit Impactor (MOUDI) were used for size distribution measurements. The ten-stage MOUDI 110 (MSP Corp. USA) was operated at 30 l/min. Particles were classified by the MOUDI in the following aerodynamic particle diameter size bins of: 0.056-0.1, 0.1-0.18, 0.18-0.32, 0.32-0.56, 0.56-1.0, 1.0-1.8, 1.8-3.2, 3.2-5.6, 5.6-10, 10-18 μm. On one MOUDI, 47 mm Teflon membrane (#R2PJ037&R2PJ047, Teflo^{TM}, Pall Corporation Life Science, Michigan, USA) filters were used on each stage with one 37 mm Teflon membranes used as the backup filter. On the other MOUDI, 47mm quartz fiber filters (#1851047, QMA, Whatman International Ltd. Maidstone, England) were used on each stage with one 37 mm filter on the backup. The MOUDI was operated for 24-hour (from 10:00 a.m. to 10:00 a.m. LST.) in order to collect sufficient deposit on each stages for chemical analysis. Ions, OC, and EC were analyzed on quartz fiber filters. While mass and elements were analyzed on the Teflon filters. During the sampling periods, particle bounce from one stage to a lower stage was neglected since the relative humidity was considered negligible owing to high humidies (60% to 80%).

3.4.2 Gravimetric analysis

In order to determine particle mass concentration by gravimetric analysis, all the filters used in this study were pre- and post- weighed at least twice (more times when the difference between two weights deviated more than ±10%) and the net weights were obtained by subtracting the pre-sampling weights from the post-sampling weights. The net weights were divided by the total sampling volume with consideration of the temperature and pressure during each sampling periods to obtain mass concentrations. Before weighing, filters were equilibrated for > 24 hours at temperatures of 20-23^{o}C and relative humidities of 30-40%. The filters were weighted on a Microbalance (Model MC5, Sartourius AG, Goettingen, Germany) with the sensitivity of ± 1 μg in the 0-250 mg range. The model MC5 Sartorius Microbalance contains a separated weighing cell and evaluation unit, which minimized thermal and electrostatic influences. The weighing cell and evaluation unit are interfaced together and also interfaced with power supply unit. An automatic door and draft shield facilitates operation and prevents disturbances. The Model MC5 Sartorius Microbalance contains an automatic, temperature-controller and internal calibration and linearization feature, which automatically calibrates the balance. In operation, a filter is placed on the weighing pan and the door of the glass draft shield is automatically closed. After approximately 20-30 seconds, the filter weight is registered on a digital display and recorded in a data base.

3.4.3 Carbon analysis

The methods currently being applied for the determination of organic and elemental carbon in particulate filters are operationally defined and it is a popular subject of investigation owing to the important roles carbon play in atmospheric chemistry and policy formulation. In the study samples were analyzed using a DRI Model 2001Thermal/Optical Carbon Analyzer (AtmAA Inc, Calabasas, CA, USA), with the IMPROVEA thermal/optical reflectance (TOR) protocol (Chow et al., 2007). A 0.526 cm^2 sample is heated to temperatures of 140 ^oC (OC1), 280 ^oC (OC2), 480 ^oC (OC3) and 580 ^oC (OC4) in a non-oxidizing He atmosphere, then to 580 ^oC (EC1), 740 ^oC (EC2) and 840 ^oC (EC3) in an oxidizing atmosphere with 2 % oxygen in Helium (He). The evolved carbon is oxidized to be carbon dioxide (CO_2) and reduced to methane (CH_4) for quantification with flame ionization detection (FID). OC pyrolysis is continuously monitored by a helium-neon (He-Ne) laser at a wavelength of 632.8nm. OC is defined as the portion of carbon that evolves before the filter reflectance attains the initial value, carbon evolving after this is defined as EC. The MDL of carbon combustion method is 0.82 $\mu g/cm^2$ for OC, 0.19 $\mu g/cm^2$ for EC and 0.93 $\mu g/cm^2$ for total carbon. All samples in this study yields concentration higher than MDL. Replicate analyses were performed for ~10% of all samples to estimate measurement precision.

3.4.4 Ions analysis

Half of each quartz fiber filter was extracted in 10 ml of ultra-pure deionized distilled water (specific resistance ≥18.1MΩ). The extraction solutions were filtered and stored in plastic vials in a refrigerator at < 4 ºC until analysis. Water soluble ions analyzed included chloride (Cl^-), nitrate (NO_3^-), sulfate (SO_4^{2-}), sodium (Na^+), potassium (K^+), calcium (Ca^{2+}) and ammonium (NH_4^+) by ion chromatography (DIONEX, USA). Ion Chromatography is a liquid chromatographic technique based on an ion exchange mechanism and suppressed conductivity detection for the separation and determination of anions. Each ion's affinity for the exchange site, known as its selectivity quotients, is largely determined by its radius and its valence. Ions are identified by its retention times within the ion exchange column and ionic concentrations are quantitatively determined from conductivity peak areas. The detection limits of chloride, nitrate, sulfate, sodium, ammonium and potassium were 0.5, 15, 20, 15 and 15 μg/l, respectively. Blank and replicated analyses were performed for 10% of all samples to calculate precisions.

3.4.5 Elemental analysis

Elemental analyses were done using an energy dispersive X-ray fluorescence (XRF) technique (Watson et al. 1999). The method was applied to determine the concentrations of about 40 different elements in particles deposited on Teflon filters without destroying the sample. The elements include: Na, Mg, Al, Si, P, S, Cl, K,

Ca, Ti, V, Cr, Mn, Fe, Co, Ni, Cu, Zn, Ga, As, Se, Br, Rb, Sr, Y, Zr, Mo, Pd, Ag, Cd, In, Sn, Sb, Ba, La, Au, Hg, Tl, Pb and U. XRF spectroscopy is based on the measurement of X-ray energy produced by the ejection of an inner shell electron from an atom in the sample. X-rays are specific for different atoms and the intensity of the X-ray is proportional to the number of atoms in the sample. Therefore, the concentrations of elements can be quantitatively determined through a comparison with known standards. Blank Teflon filters were also analyzed to evaluate potential contaminations during the filter handling process.

3.5 Calculations and modeling

3.5.1 Absorption coefficient calculation

The particle light absorption coefficient B_{ap} can be directly calculated from the attenuation measured by Aethalometer or indirectly calculated based on the BC concentrations reported from the instrument. The direct calculation of particle light absorption at any wavelength, λ, uses the following equation 3.1 (Weingartner et al., 2003; Yang et al., 2009):

$$B_{ap,\lambda} = \frac{A}{q} \times \frac{\Delta ATN\ (\lambda)}{\Delta t} \times \frac{1}{CR} \qquad (3.1)$$

Where, A is the filter spot area, cm^2, q is the volumetric flow rate, L/min, and ΔATN is the change in the attenuation during the time interval Δt, min, and C is a wavelength-independent empirical correction factor, which corrects for the enhancement of the optical path due to multiple scattering of the light beam within the filter fiber, R is the correction factor describing the changes in instrumental response with increased particle loading on the filter (shadow effect). The C factor varies for different particle types and mixing states and R = 1 unity for light loadings (Weingartner et al., 2003). Or to make the equation easier to understand, the equation 3.2 could be re-expressed as:

$$B_{ap} = (B_{atn} - F_{aa} \times B_{sp}) \times \frac{F_{load}}{F_{ms}} \qquad (3.2)$$

At a given time (t) and wavelength (λ), the corrected absorption coefficient (B_{ap}) is related to raw absorption coefficient from Aethalometer attenuation (B_{atn}), by three wavelength-dependent correction factors. F_{aa}, which is the apparent absorption correction factor adopted from Arnott et al., (2005); F_{ms} is the multiple scattering coefficient correction factor taken from Weingartner et al. (2003) for coated soot, and B_{sp} is from the nephelometer. F_{load} is calculated based on the equation 3.3.

$$F_{load} = (R_f\text{-}1) \times \frac{Ln\ (ATN\ (t,\lambda)) - Ln(ATN\ (A,\lambda))}{Ln\ (ATN\ (B,\lambda)) - Ln\ (ATN\ (A,\lambda))} \qquad (3.3)$$

Here A designates the first point after the Aethalometer tape advancement and B represents the last point before that advancement, respectively. At a given wavelength, R_f is defined as R_a/R_s, where $R_a = B_{atn}(A)/ B_{atn}(B)$ and $R_s = B_{sp}(A)/ B_{sp}(B)$.

In the PRD region, Schmid, et al (2005) have conducted a study to find out an absorption coefficient conversion factor $\alpha = 8.28\ m^2/g$, with correlation coefficient $R^2=0.92$ with a liner regression to BC concentrations at 880 nm from the light absorption coefficient at 532nm.

3.5.2 Single scattering albedo (SSA) calculation

The single scattering albedo (SSA, ω) at 550nm was calculated as equation 3.4:

$$\omega = \frac{B_{sp}}{B_{sp}+B_{ap}} \qquad (3.4)$$

SSA was used to evaluate the source of primary and secondary PM.

3.5.3 Angstrom exponent calculation

The scattering Angstrom exponent and absorption Angstrom exponents were calculated from equation 3.5:

$$\alpha_s = -\frac{\mathrm{Ln}\left(B_{sp}^{\lambda 1}/B_{sp}^{\lambda 2}\right)}{\mathrm{Ln}\left(\lambda 1/\lambda 2\right)} \quad \text{and} \quad \alpha_a = -\frac{\mathrm{Ln}\left(B_{ap}^{\lambda 1}/B_{ap}^{\lambda 2}\right)}{\mathrm{Ln}\left(\lambda 1/\lambda 2\right)} \qquad (3.5)$$

The scattering Angstrom exponent is used to determine the dominant particle size in the sampling site and the absorption Angstrom exponent is used to evaluate the chemical composition of light absorption, i.e. those compounds related to BrC.

3.5.4 Methods for chemical extinction calculation

In the study, light extinction measurement only included particle phase and hence this is called particle light extinction. In order to further understand the relationship between chemical species and visibility degradation. Particle light extinction for size-resolved particles is calculated based on the Mie theory (Mie, 1908). Ammonium sulfate, ammonium nitrate, particulate organic matter (POM), sea salt and soil dust are the chemical components that contribute to visibility degradation. The followed equations 3.6, 3.7, 3.8, 3.9, 3.10 are used to derive mass contributions from the markers for major chemical component, i.e. ammonium sulfate, ammonium nitrate, POM, sea salt and soil dust. The coarse mass was estimated by

summing particle mass in the 1.8 to 10 μm size bins. Mass scattering efficiencies (MSE) for ammonium sulfate, ammonium nitrate, particle organic matter, sea salt, soil dust and coarse mass for original IMPROVE, revised IMPROVE, Guangzhou, Shanghai chemical extinction algorithms were summarized in Table 2.3 (Cheng et al., 2015; Jung et al., 2009; Pitchford et al., 2007; Sloane, 1986; Sloane et al., 1991). In the study, comparison of particle scattering coefficient were focused, the mass absorption efficiency (MAE) was ignored.

$$\text{Ammonium sulfate}=1.375\times SO_4^{2-} \quad (3.6)$$

$$\text{Ammonium nitrate}=1.29\times NO_3^{-} \quad (3.7)$$

$$\text{Particle organic matter} =1.8\times OC \quad (3.8)$$

$$\text{Fine soil}=2.2\times Al+2.49\times Si+1.63\times Ca+2.42\times Fe+1.94\times Ti \quad (3.9)$$

$$\text{Sea salt}=1.8\times Cl^{-} \quad (3.10)$$

Since particle scattering depending on hygroscopic characteristics of these components, the internal nephelometer RH value was used for the RH hygroscopic curve (U.S. IMPROVE *f*(RH) and f_{ss}(RH)). U.S. IMPROVE *f*(RH) was used for ammonium sulfate, ammonium nitrate, U.S. IMPROVE f_{ss}(RH) was used for sea salt. The particle scattering coefficient equation is shown below (equation (3.11)),

B_{sp} = f(RH)×(MSE_1)×[ammonium sulfate] + f(RH)×(MSE_2)×[ammonium nitrate] + (MSE_3)×[particle organic matters] + f_{ss}(RH)×(MSE_4)×[sea salt] +(MSE_5)×[soil dust] + (MSE_6)×[coarse mass] *(3.11)*

The scattering cross section (Q) was calculated via the Mie theory (Mie, 1908) by introducing particle diameters (D), refractive indexes (m) and incident wavelengths (λ). The MOUDI particle size bins were converted to continuous size distributions by positive matrix factorization (PMF) and a log-normal distribution inversion (Huang et al., 2006b; Kim et al., 2003). The mass scattering efficiency of specific particle was estimated by equation (3.12), where Q stands for scattering cross section, D is particle size and ρ is density of chemical component.

$$MSE = \frac{3Q}{2D\rho} \quad (3.12)$$

The integrated fine particle MSE for the species was calculated by equation (3.13), where j represent different chemical components, $C_{j,D}$ stands for the concentration of the species in the particle size. All the particle species are assumed external mixed.

$$\text{MSE (j, D} \leq 2.5\ \mu\text{m}) = \frac{\sum_{stage=1}^{D\leq 2.5\mu m} MSE\ (j,D)\times C_{j,D}}{\sum_{stage=1}^{D\leq 2.5\mu m} C(j,D)} \quad (3.13)$$

3.5.5 PMF-solution receptor model

EPA positive matrix factorization (PMF) solves the CMB equations using constrained, weighed, least-squares. The general model assumes there are p sources, source types or source regions with similar source profiles (termed factors) contributable impacting a receptor, and liner combinations of the impact from the p factors give rise to the observed concentration of the various species. Mathematically stated as:

$$X_{ij}=\Sigma^{p}_{k=1}\, g_{ik}f_{kj}+e_{ij} \qquad (3.14)$$

Where x_{ij} is the concentration at receptor for the j^{th} species on the i^{th} sample, g_{ik} is the contribution of the k^{th} factor to the receptor on i^{th} sample, f_{kj} is the fraction of the k^{th} factor that is species j, and e_{ij} is the residual for the j^{th} species on the i^{th} sample. The EPA PMF software assumes that only the x_{ij}'s are known so that the goal is to estimate the g_{ik} and x_{ij} are calculated by minimizing the sum of squares:

$$Q=\sum_{i=1}^{n}\sum_{j=1}^{m}\left[\frac{x_{ij}-\sum_{k=1}^{p} g_{ik}f_{ki}}{u_{ij}}\right] \qquad (3.15)$$

Where u_{ij} is the uncertainty in j^{th} species for sample i, EPA PMF software's robust mode minimizes the influence of outliers when fitting of the source factors and contributions to the measured species concentrations. If the model is appropriate for the data and if the uncertainties specified area truly reflect the true uncertainties in the data, then Q should be less than the number of data points in the concentration data set. The uncertainty estimation provides a useful tool to decrease the weight of missing and below detection limit data in the solution as well as to account for the variability in the source factors. PMF-derived source factors do not necessarily correspond to real-world source profiles, there is often profile mixing within a factor, especially when marker concentration are correlated owing to meteorological factors.

3.5.6 CWT back trajectories

The cluster analysis technique can aid in understanding the particle emission sources under different air masses. It uses a multivariate statistics method to combine all the trajectories into one to ten representative trajectories based on the air parcel transportation. Concentration weighted trajectory (CWT) analysis is used to determine source regions for the source factors. Each grid cell gets a weighted concentration by averaging sample values on the receptor place when the related trajectories pass through the grid cell (Vinoj et al., 2010). The CWT analysis could improve the limitation of potential source contribution function (PSCF) method for the potential source region identification. CWT analysis has been developed more recently and the method is more sophisticated than PSCF as it shows the spatial

pattern of the potential sources of particles at the receptor site (Wang et al., 2009). In CWT method, every grid cell is a weighted concentration by averaging sample concentrations, which has trajectories crossing the grid cell. The calculation formula is followed:

$$C_{ij} = \frac{1}{\sum_{l=1}^{M} \tau_{ijl}} \sum_{l=1}^{M} C_l \tau_{ijl} \qquad (3.16)$$

Where C_{ij} is the averaged weight given to the *ij*th cell, *l* is the index of the trajectory, M is the total number of trajectories, C_l is the concentration observed on arrival from trajectory *l*, and τ_{ijl} is the time spent in the *ij*th cell by trajectory *l*. A high value for C_{ij} implies that air parcels traveling over the *ij*th cell would be, on average, associate with high concentrations at the receptor. The arbitrary weighting function described above was used in CWT analyzes to reduce the effect of the small value of n_{ij}.

3.5.7 E-AIM model

The Extended aerosol inorganic model (E-AIM, http://www.aim.env.uea.ac.uk/aim/aim.php) was used to estimate the water content calculation of the particles. The model included four types of model, AIM-I, AIM-II, AIM-III and AIM-IV. The condition of each model category varies, but the principle is similar, which determines the gas/particle positioning of complex

mixture (Clegg et al., 1998; Clegg and Seinfeld, 2004). In the present study, web-version AIM-II was used to calculate the liquid using ambient temperature, pressure, relative humidity, and molar concentrations of ambient water-soluble ions (SO_4^{2-}, NO_3^-, NH_4^+ and H^+).

3.6 Quality assurance and quality control (QA/QC)

3.6.1 Instruments calibration and flow check

- Nephelometers were automatically conducting a zero check every day at 0:00 for 15 min and a manual span check were performed every month.
- The Aethalometer does not need to do any special calibration actions, but flow rates of the instrument were checked weekly.
- For the size-resolved sampler, MOUDI, flow rates were checked before and after each sample and did not deviate from 30 l/min by more than ±5%. Impactor sets plates were cleaned with compressed air or strong solvent after each sample. Because heavy particle loading is very easy to be stuck into impactor nozzle, based on the principle of sampling collection.

3.6.2 Filter handling

Quartz and Teflon filters are used in the study. Before sampling, 47mm quartz fiber filters should be preheated at 900 ^{o}C in an electric furnace for 3 hours to remove carbonaceous contaminants to absorb on filters. 20.3 cm × 25.4 cm quartz microfiber filters should be preheated at 540 ^{o}C for 3 hours. All the filters (quartz fiber filters, Teflon filters) need to be equilibrated in a RH (30% - 40%) and temperature (20 - 30 ^{o}C) controlled desiccator for 24 hours before pre-sampling weighing. Filter is used for sampling need to handle it with cautious, cleaned forceps and disposable gloves to prevent contaminants. After sampling, filters should be placed into clean plastic petri dishes quickly transported to RH and temperature controlled desiccator for post-sampling weighing. After weighing, all samples should be stored in refrigerator at about - 4 ^{o}C to prevent the volatile components evaporation and wait for the chemical analysis.

3.6.3 Chemical analysis

In order to reduce background contamination, blank samples are essential for chemical analysis, one blank sample for each batch of 10 samples.

Water-soluble ions – Dionex Ion Chromatography

Plastic tubes and glassware were cleaned with distilled deionized water followed by air-drying. Calibration standards were prepared weekly with values spanning the range of expected concentrations. The detection limit of Ion Chromatography

should be investigated before analyzing samples. 5-6 standard concentrations were prepared and each standard was analyzed for 3-5 times to determine repeatability. The variation of each standard was within ±5%. Replicates samples were run with each set of 10 samples to ensure the stability of the instrument baseline and evaluate precision.

Carbonaceous materials – DRI OC/EC analyzer

Components were regularly cleaned, maintained, or replaced, (e.g. punching tool, forceps, and quartz rods). Calibrations were performed after repairs and instrument adjustment. 5% CH_4/He standard served as an internal calibration check at the end of each run to normalize any drift in FID response. KHP and Sucrose solution standards were used for instrument calibration, which was performed every 6 months or after maintenance. Replicated samples were analyzed for every 10 samples. When replicated differed by more than ± 10%, the entire batches was re-analyzed.

Elements – XRF analyzer

Samples for XRF analysis should be not heavy, otherwise, the absorption of the incident X-rays will be influenced. The film standards were used for calibration, performance testing and evaluation. Polymer film and NIST (National Institute of Standard and Technology) standards are used for quality control. A NIST standard and a replicate sample were analyzed with each batch. If the difference with respect to the NIST standard values exceeded ±5%, or if the difference among replicates exceed ±10%, the batch of samples are needed to be re-analyzed.

Before samples were analyzed for water-soluble ions, OC/EC, and elements, the method detection limit is needed, the method of detection limit of all the species is summarized in the followed Table 3.2

3.6.4 Data validation

Several measures of data validation were conducted to ensure data accuracy, precision and validity: a) sum of species to mass ratio; b) anions to cations ratios; and c) SO_4^{2-}/S and Cl^-/Cl ratios.

The measured versus reconstructed mass

Figure 3.2 shows the relationship between the reconstructed and measured Teflon-filter mass concentration for each impactor stage. The reconstructed mass was calculated based on the sum of equation 3.6 – 3.10: fine soil ($2.2\times Al+2.49\times Si+1.63\times Ca+2.42\times Fe+1.94\times Ti$), particle organic matter ($OC\times 1.8$), soot (elemental carbon), ammonium sulfate ($1.375\times SO_4^{2-}$), ammonium nitrate ($1.29\times NO_3^-$) and non-crustal trace elements (sum of other-than-geological trace elements). A reasonable correlation of $R^2 = 0.90$ was found. It is confirmed the validity of the gravimetric and chemical measurement.

Anions Versus Cations

Figure 3.3 shows the anion and cation balance. The correlation of the balance for different particle size collected by MOUDI ($R^2 = 0.88$) and the slope is ~1. This scatter plots suggest that adequate anions & cations were measured for this study.

Sulfur versus sulfate; chlorine versus chloride

Figure 3.4 shows the correlation between S and SO_4^{2-}; Cl and Cl^-. The ratio of sulfate to sulfur is ~3 with good correlation ($R^2 > 90$); the ratio of chloride to chlorine is less than unity with high correlation ($R^2 > 90$) support that XRF and IC measurement are valid in this study.

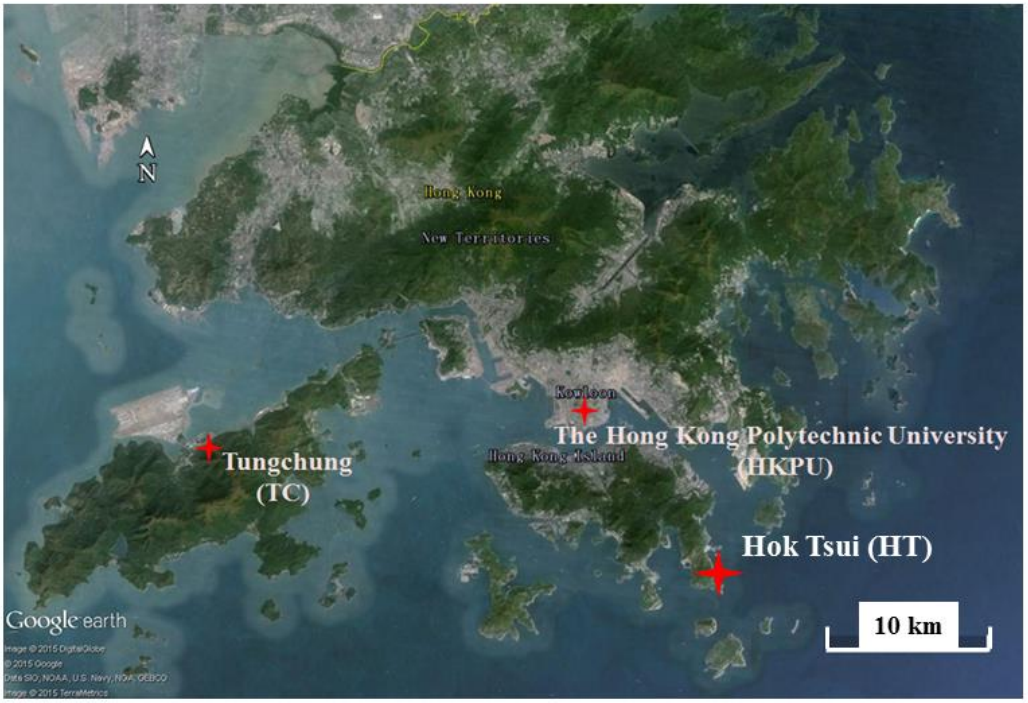

Figure 3.1 Sampling sites located at: 1) Hok Tsui (HT); 2) Tung Chung (TC); 3) the Hong Kong Polytechnic University (HKPU)

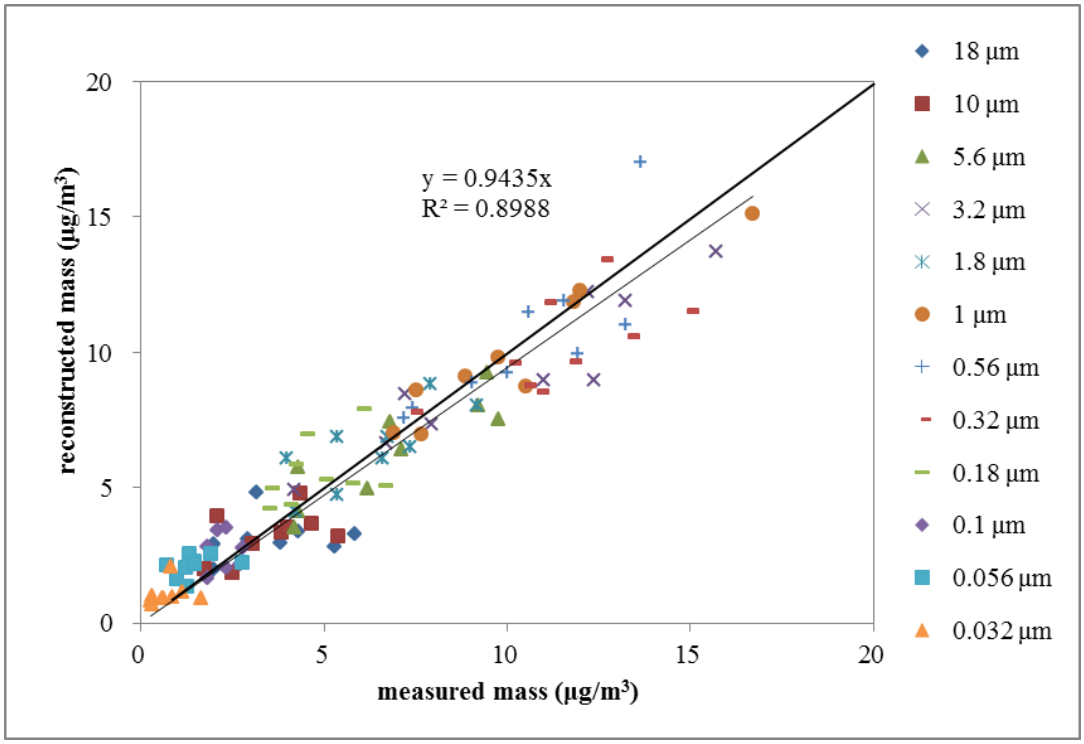

Figure 3.2. Average 24-h relationship between measured mass and reconstructed mass

(fine soil: 2.2×Al+2.49×Si+1.63×Ca+2.42×Fe+1.94×Ti; particle organic matter: OC×1.8; ammonium nitrate: 1.29×NO_3^-; ammonium sulfate: 1.375×SO_4^{2-}; sea salt: 1.8×Cl^-; non-crustal elements: sum of other-than-geological elements)

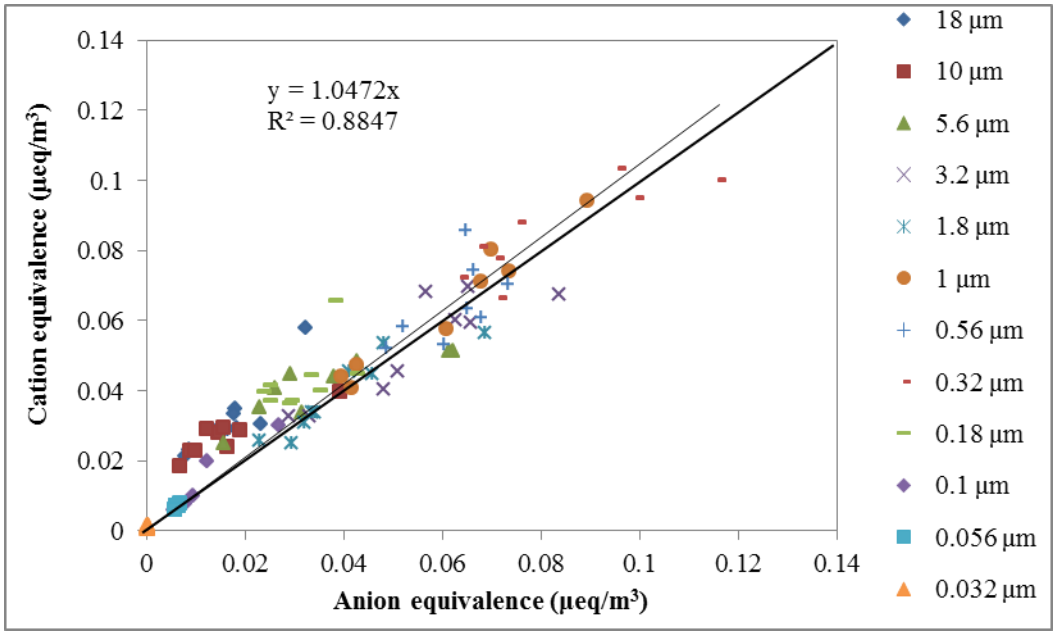

Figure 3.3 Anion and cation balance for different size bins;

$$(Anion = \frac{(sulfate)}{96} + \frac{(nitrate)}{62.005} + \frac{(chloride)}{35.453};$$

$$Cation = \frac{(sodium)}{23} + \frac{(ammonium)}{18.04} + \frac{(pottasium)}{39.098})$$

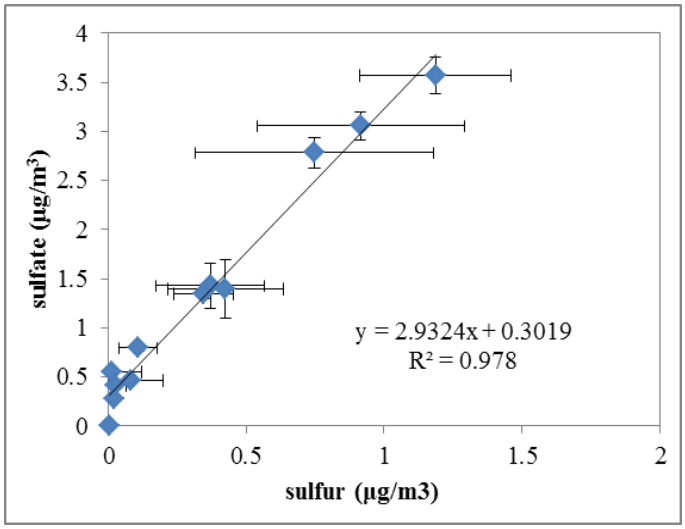

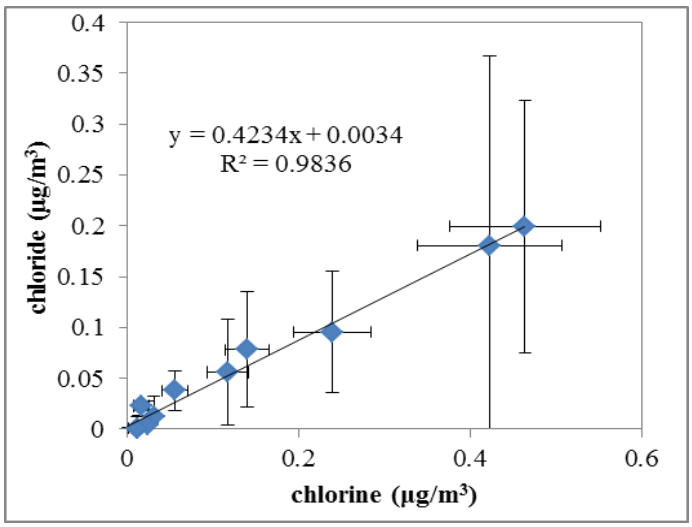

Figure 3.4 Scatter plot for sulfur versus sulfate and chloride versus chlorine. (Total sulfur and chlorine were measured on Teflon-membrane filter by X-ray Fluorescence, whereas water-soluble sulfate and chloride anions were measured by ion chromatography)

Table 3.1 Measurement periods and variables

	Sample duration	**HT**	**TC**	**HKPU**
Period		1st June 2011-31st May 2012	August 2011 November 2011 February 2012 May 2012	October to December 2010
Black carbon (BC) (λ = 880 nm)	1 hour	Aethalometer Model AE-31, Magee scientific, USA	Aethalometer Model AE-31, Magee scientific, USA	Aethalometer Model AE-31, Magee scientific, USA
Particle light scattering, B_{sp}	1 hour	Nephelometer Model 3563 TSI Inc. (λ = 470, 520, 700 nm)	Nephelometer Model M9003, Ecotech, Australia (λ = 525 nm)	Nephelometer Model M9003, Ecotech, Australia (λ = 525 nm)
Size-resolved particles	24 hours	N/A	2 sets of MOUDI 110, MSP Corp. USA with Teflon and quartz filters	2 sets of MOUDI 110, MSP Corp. USA with Teflon and quartz filter

			(Flow rate = 30 l/min)	(Flow rate = 30 l/min)
Meteorological data (T, RH, WS, WD, visual range)	1 hour	HKO	HKO	HKO

Table 3.2 Method detection limit of chemical species

Species analysis	**Species**	**Method detection limit (MDL, μg/m^3)**
Water-soluble ions	Na^+	0.006327
	NH_4^+	0.012655
	K^+	0.008858
	Mg^{2+}	0.0088
	Ca^{2+}	0.0086
	Cl^-	0.012655
	NO_3^-	0.012655
	PO_4^{3-}	0.01266
	SO_4^{2-}	0.012655
Carbons	OC	0.064167
	EC	0.008556
Elements	Na	0.203613
	Mg	0.33254
	Al	0.00743
	Si	0.042429

P	0.001051
S	0.000688
Cl	0.000589
K	0.001037
Ca	0.000414
Sc	0.00074
Ti	0.000295
V	0.00027
Cr	0.000488
Mn	0.000788
Fe	0.001821
Co	0.000295
Ni	0.000369
Cu	0.000438
Zn	0.000526
Ga	0.001921
As	0.000491
Se	0.000806

	Br	0.000754
	Rb	0.000492
	Sr	0.000459
	Pb	0.001395

Remark: Method detection limit (MDL) is the concentration at which instrument response equals three times the standard deviation of the lab blanks concentrations

Chapter 4. Particle optical properties in Hong Kong

4.1 Introduction

Visibility degradation becomes an indicator of local and regional air pollution, because a decreased visual range is mainly due to increased light scattering and absorption by suspended particles and gases. Based on the comprehensive review study by Watson (2002), the strong linkage between air pollution and visibility reduction was observed in U.S. urban, remote area and national parks (Lowenthal and Kumar, 2003; Malm et al., 2003; Watson, 2002). Since 1986, studies with visibility impairment in Hong Kong have been conducted and the important cause for visual range reduction was air pollution (Chang and Koo, 1986; Man and Shih, 2001; Wang et al., 2003). From Hong Kong Observatory reported low visibility days' record, the low visibility days were significantly increased since 2004-2015 until the present when the number of low visibility days is three times the number of low-visibility days observed in 1986. Man and Shih (2001) have determined seasonal particle light scattering coefficient and absorption coefficient characteristics in HT, which is the only study of optical properties in a Hong Kong rural area. Many previous Hong Kong studies have discussed the relationship between particle and visibility impairment based on the large particle size bulk (Lai and Sequeira, 2001). Some studies have investigated the chemical species contribution to particle light scattering in Hong Kong via U.S. IMPROVE equations. This thesis includes a detailed study that determined particle and chemical components in relation to visibility degradation in Hong Kong and

simulated a Hong Kong chemical extinction equation (see Chapter 6). The relationship of size-segregated chemical components with particle light scattering coefficient is provided in Chapter 7.

In this chapter, particle light scattering and absorption coefficients are derived for the Hong Kong urban (HKPU), sub-urban (TC) and rural sites (HT). Seasonal variations of B_{sp}, B_{ap} are also presented for the sub-urban and rural sites. Angstrom scattering exponents are calculated to better understand the particle size effects on light scattering at the rural site. The relationship of fine particles and meteorological parameters with visibility impairment is also examined.

4.2 Results and discussion

4.2.1 Light extinction (B_{ext}) composition in Hong Kong

B_{ext} is the sum of particulate and gaseous scattering and absorption. On average of Hong Kong three sites, B_{ext} in Hong Kong was 186 ± 73 Mm^{-1}. Particle scattering and absorption was dominant, similar to worldwide cases, which constituted ~90% of B_{ext}, with B_{sp}, B_{ap}, B_{sg} and B_{ag} accounting for ~ 75%, 14%, 7% and 4%, respectively. Gaseous scattering is Rayleigh scattering which assumes to be a constant, 13 Mm^{-1}. There was no clear seasonal variation in these relative contributions (Figure 4.1). B_{sp} constituted ~71% to 77% of B_{ext} while B_{ap} constituted ~12% to 14% of B_{ext}. The highest B_{ext} value was observed in the fall and winter months, and was attributable to regional air pollution. During the fall and the winter, northerly winds brought pollutants from the mainland China. The

highest B_{ext} value was observed at the Hong Kong urban site, HKPU, indicating an enhancement by locally-produced PM. The NO_2 B_{ag} contribution was the highest at HKPU, indicating the importance of engine exhaust. BC concentrations to B_{ap} were also enhanced at HKPU, indicative to the importance of local traffic source.

4.2.2 Temporal variations on particle optical properties in HKPU, TC and HT

Figure 4.3 (a-c) shows B_{sp} and B_{ap} time series with meteorological parameters at the three sampling sites in Hong Kong. B_{sp} at HT ranged from 2.09 to 907.11 Mm^{-1} and B_{ap} value ranged from 2.23 to 122.35 Mm^{-1}. The B_{sp} values observed at HKPU and TC ranged from 2.43 to 788.91 Mm^{-1} and from 5.67 to 892.04 Mm^{-1}, respectively. B_{ap} value showed the largest standard deviation, from 4.77 to 156.95 Mm^{-1} at HKPU and from 3.36 to 168.23 Mm^{-1} at TC, respectively. At HT and TC site, B_{sp} and B_{ap} were highest in autumn (September to November) and in winter (December to February) with lower values in summer (June to August) and spring (March to May). Table 4.1 summarizes particle optical properties among the three sites, HT, TC and HKPU. Average B_{ap} value at HT, TC and HKPU were 15.12, 21.08 and 39.91 Mm^{-1}, respectively. The mean B_{sp} values at HT, TC and HKPU were 110.84, 116.48 and 201.96 Mm^{-1}, respectively.

Particle light scattering coefficient (B_{sp}) and particle light absorption coefficient (B_{ap})

B_{ap} and B_{sp} at the Hong Kong sites were much lower than those measured in mainland China. The values for Hong Kong were 30-200% higher than those recorded for other countries, as shown in Table 4.2. B_{ap} and B_{sp} at HT were lower than those at Lin'an (23 and 353 Mm^{-1}), Shangdianzi (18 and 174 Mm^{-1}), Xinken (70 and 333 Mm^{-1}) and Tai' O (22 and 224 Mm^{-1}) (Cheng et al., 2008; Wang et al., 2003; Yan et al., 2008). They exceed those found at higher than in Mukteshwar, India (Hyvärinen et al., 2009). B_{ap} value measured in Yulin was lower than that at HT but B_{sp} value was 40% higher than that at HT (Yan et al., 2008). It may be due to lower source strengths near the sampling site compared with HT site. Compared to B_{ap} and B_{sp} values measured at HT 13 years ago (Man and Shih, 2001), the current B_{ap} was lower, but B_{sp} value was higher (Man and Shih, 2001). In recent years, BC emissions from motor engines in Hong Kong have been decreasing whereas regional pollutants from the mainland China have been increasing. These changes may be due to different characteristics of the local and regional sources. B_{ap} and B_{sp} at TC and HKPU were lower than these measured in mainland China at places such as Beijing (83 and 488 Mm^{-1}), Guangzhou (91 and 418 Mm^{-1}) and Shanghai (66 and 293 Mm^{-1}) (Andreae et al., 2008; Xu et al., 2012; Yan et al., 2008). HK values exceed those in Atlanta, USA (16 and 120 Mm^{-1}), Southern Mexico City, Mexico (12-29 and 21-93 Mm^{-1}), and Granada, Spain (24 and 61 Mm^{-1}) (Garcia et al., 2010; Titos et al., 2012; Xu et al., 2012).

B_{ap} and B_{sp} frequency distributions are compared in Figure 4.4. B_{ap} at HT and TC are frequently < 20 Mm^{-1}, while B_{sp} are mostly < 200 Mm^{-1}. The higher values of

B_{ap} and B_{sp} were more frequent at HKPU than at HT and TC, suggesting the presence of more light scattering and absorption sources at HKPU worsening visibility degradation.

Diurnal B_{sp} and B_{ap} variations at HKPU, TC and HT are illustrated in Figure 4.5. Since HT was a Hong Kong rural site surrounding which there were no continuous emission sources, no clear diurnal variation was observed at this site, in contrast to the clear diurnal pattern seen at HKPU. HKPU shows two B_{ap} peaks, corresponding to the morning (9:00 a.m.) and evening (19:00 p.m.) rush hours of local traffic.. HKPU B_{sp} was not clear in the afternoon, likely resulting from secondary formation. In the sub-urban area, B_{sp} at TC showed a peak in the afternoon (16:00 p.m.), possibly due to secondary aerosol formation (Wang et al., 2005). Since EC or BC is the most important contributors to particle absorption, traffic activities are the main sources on particle absorption (Bond and Bergstrom, 2006). There was no heavy traffic in TC, so the morning and evening B_{ap} peaks were not evident.

Single scattering albedo (SSA, ω)

The single scattering albedo (SSA) = $B_{sp}/(B_{ap}+B_{sp})$ is related to radiative forcing (Haywood and Boucher, 2000). The mean values of SSA, ω, were 0.84, 0.81 and 0.82 at HT, TC and HKPU, respectively. The difference of SSA, ω among the three sites was small which indicated that 16%-19% of pollutants from B_{ap} and 81%-84% of pollutants from B_{sp} in the three sampling site and similar SSA value in China and U.S. urban sites had been reported in past 10 years (Table 4.2). Compared to SSAs, ω, from US rural areas (0.95-0.99) (Delene and Ogren, 2002), Hong Kong SSA is much lower, indicating even rural Hong Kong is affected by primary pollutants, e.g. BC, more so than in the U.S.

Scattering Angström exponent (α_s)

Scattering Angström exponent (α_s) is related to coarse particles that affect B_{sp}. Large particle sizes have lower α_s. For fine particles, α_s is ~ 1.5, while α_s is ~ 0 for coarse particles (Esteve et al., 2012). It could be calculated by three wavelengths of nephelometer. At HT, the mean α_s value is 1.23 ± 0.42 (Table 4.1), similar to the mean value of 1.28 obtained at a Greece remote coastal area (Finokalia), but lower than α_s value = 1.4 measured at Evora (Portugal), and α_s ~1.6 obtained at a Spain urban coastal site in Valencia, Spain (Esteve et al., 2012). In North China, Yang et al., (2009) found the varied values in different circumstances, with mean α_s value = 0.59 for Asian dust pollution, ~1.52 for biomass burning, and ~1.39 for coal combustion pollution episodes. In addition, the sampling site is a coastal site and sea salt seems as a constant source for light scattering contributor, which could make large contribution on coarse particle size, decreasing the value.

4.2.2 Seasonal variation of particle optical properties

The seasonal variations of particle optical properties and influencing factors have been discussed in HT and TC sites.

Hong Kong rural area-HT

Seasonal average B_{ap} and B_{sp}, SSA,ω and α_s are shown in Table 4.3 (a), in which the summer time is from June to August 2011, the autumn is from September to November 2011, the winter is from December 2011 to February 2012 and the spring is from March to May of 2012. B_{ap} and B_{sp} were higher in fall (16.79 ± 8.9 Mm^{-1}

and 124.23 ± 82.4 Mm^{-1}) and winter (18.74 ± 10.3 Mm^{-1} and 157.27 ± 98.8 Mm^{-1}), and lower in summer (10.84 ± 10.1 Mm^{-1} and 65.24 ± 75.2 Mm^{-1}) and spring (12.87 ± 7.5 Mm^{-1} and 91.30 ± 73.3 Mm^{-1}). Different patterns were found in a Beijing rural area (Shang dianzi), with the highest values in summer and fall, and lowest values in winter (Yan et al., 2008). Different emission sources and meteorology situation cause these differences. SSA (ω), showed no significant seasonal variations, indicating that the contribution of primary and secondary pollutants to the aerosol light extinction did not siginificantly differ by season. However, different from SSA, calculated scattering angström exponent (α_s) showed seasonal changes, with the highest values in the autumn and the lowest values in the spring. The reason for the seasonal variation pattern can be explained by Hong Kong wind patterns. In the summer, the prevailing wind is mainly from the south-west, where there are no strong anthropogenic emission sources. In the winter, the dominant wind direction is from the northeast to north, carrying air from polluted regions. In the autumn, wind direction variability is large, mainly from the east to north, and similar to the spring circumstances.

Hong Kong sub urban area-TC

The seasonal variation of light extinction has been measured in TC, a residential urban site in Hong Kong. Several anthropogenic emission sources affect B_{ext} at TC. Table 4.3(b) shows seasonal variation of optical property in TC based on observations in four months including August, November (2011), February and May (2012). These months represented the four seasons corresponding to, summer, autumn, winter and spring, respectively. High B_{ap} and B_{sp} values were measured in autumn and winter, with lower values measure in summer and spring. During the

autumn and winter period, winds were from the north, bringing polluted air masses from mainland China. The SSA (ω), the value is differed in summer compared with the other three seasons, with value of 0.75, compared to three seasons during the other (0.8).

4.2.3 Visual range relationship to other indicators in Hong Kong sub-urban area

Visual range is determined at the Hong Kong airport station, close to the TC site. HT and HKPU do not have nearby visibility observation data, so comparisons are not possible.

Visual range is negatively correlated with B_{ap} and B_{sp} (Figure 4.6a and 4.6b). Black carbon is the key light absorber and $PM_{2.5}$ contains the most efficient light scattering compounds (Xu et al., 2012). Figure 4.6c and 4.6d illustrate BC's influence and $PM_{2.5}$ influence on VR. Jung et al., (2009) proposed: VR= 749.9× $[PM_{2.5}]^{-1.035}$ (R^2=0.93) in Guangzhou. Xu et al., (2012) proposed: VR= 160.36× $[PM_{2.5}]^{-0.692}$ (R^2=0.36) in Shanghai. Cao et al., (2012) reported: VR=1.88+ 19.46× $e^{-0.01[PM2.5]}$ (R=0.61) in Xi'an. For TC, VR= 69.439× $[PM_{2.5}]^{-0.493}$ (R^2=0.63) and VR= 20.981× $[BC]^{-0.421}$ (R^2=0.36). BC is a poorer indicator of VR but $PM_{2.5}$ is a better VR indicator. The correlation with visibility and $PM_{2.5}$ in Xi'an and Shanghai is not high, estimating that the primary emission (traffic emission), e.g. black carbon, is the main contributor to the visibility impairment. In Figure 4.7 shows the best relationships are between B_{sp} and $PM_{2.5}$, and between B_{ap} and EC with good correlations ($R^2 > 0.8$). B_{ap} and $PM_{2.5}$ are not well correlated ($R^2 = 0.67$). The slope

of B_{ap} and EC is 11 m^2/g, consistent with the IMPROVE equation MSE value of 10 m^2/g. The ratio of light scattering coefficient and $PM_{2.5}$ is 4.9 m^2/g, within the spread of MSEs from the U.S. (7.4 m^2/g), Guangzhou (3.5 m^2/g), and Beijing (4.2 m^2/g) (Hand and Malm, 2007; Tao et al., 2009; Tao et al., 2015). The ratio between particle light scattering coefficient and $PM_{2.5}$ in China is almost the same, but the ratio in U.S. is around a factor of two higher, which indicate that particle composition and particle size distribution are different between U.S. and China. In order to understand the relationship between chemical components and particle light extinction, the new mass scattering efficiency should be identified based on the local particle size distribution and chemical composition.

4.3 Summary

With the rapid industrial development, low visibility problem attracts many people's attentions for concerns. Light extinction (B_{ext}) can directly represent the relationship between optical property and chemical characteristics. Most dominated composition of B_{ext} is particle scattering, B_{sp}, with ~76% of the contribution. There is no clear seasonal variation on the contribution of light extinction components, i.e. B_{sp}, B_{ap}, B_{sg}, B_{ag}. The highest light extinction was observed in Hong Kong urban site, because of complex emission sources, i.e. traffic activities, cooking, etc. The dominant B_{sp}, B_{ap} values in HT and TC are 0-100 Mm^{-1} and 0-20 Mm^{-1}. But the most of B_{sp} and B_{ap} value in HKPU was distributed in 100-200 Mm^{-1} and 30-50 Mm^{-1}. No clear diurnal variation of B_{sp} and B_{ap} in HT. The value of scattering angstrom exponent in HT indicated fine particle size is major contributor for

visibility degradation. There is one dominated peak on B_{sp} in TC. The significant two traffic peaks were observed in HKPU site. The mean value of the B_{sp} and B_{ap} is 30%-80% and 50%-80% lower than the value measure in mainland China but 30-100% and 20%-200% higher than the value measured in US and EU cities. Black carbon is the main contributor to the light absorption. From 2004-05 to 2011-12, the black carbon concentration has 27% to 48% decreasing in Hong Kong rural site, which caused 32% light absorption value reduction. By comparing $PM_{2.5}$ with B_{sp} and B_{ap}, the strong correlation ($R^2 = 0.93$) between B_{sp} and $PM_{2.5}$ was observed, which indicated that $PM_{2.5}$ was majorly scattered the sunlight. The ratio between B_{sp} and $PM_{2.5}$ was 4.9 m^2/g, U.S. value is 2 factors higher, due to varied chemical components in $PM_{2.5}$ and different particle size composited. Therefore, the new mass scattering/absorption efficiency need to be investigated based on the local particle size-distribution and chemical composition.

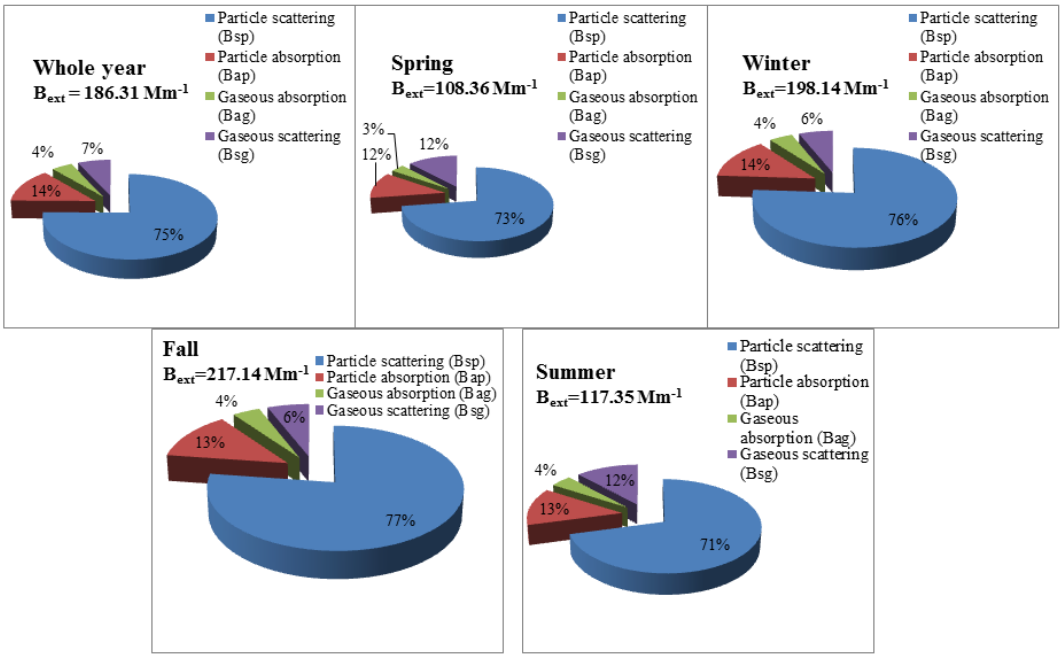

Figure 4.1 Fractional contributions of particle and gas scattering and absorption to B_{ext} by season

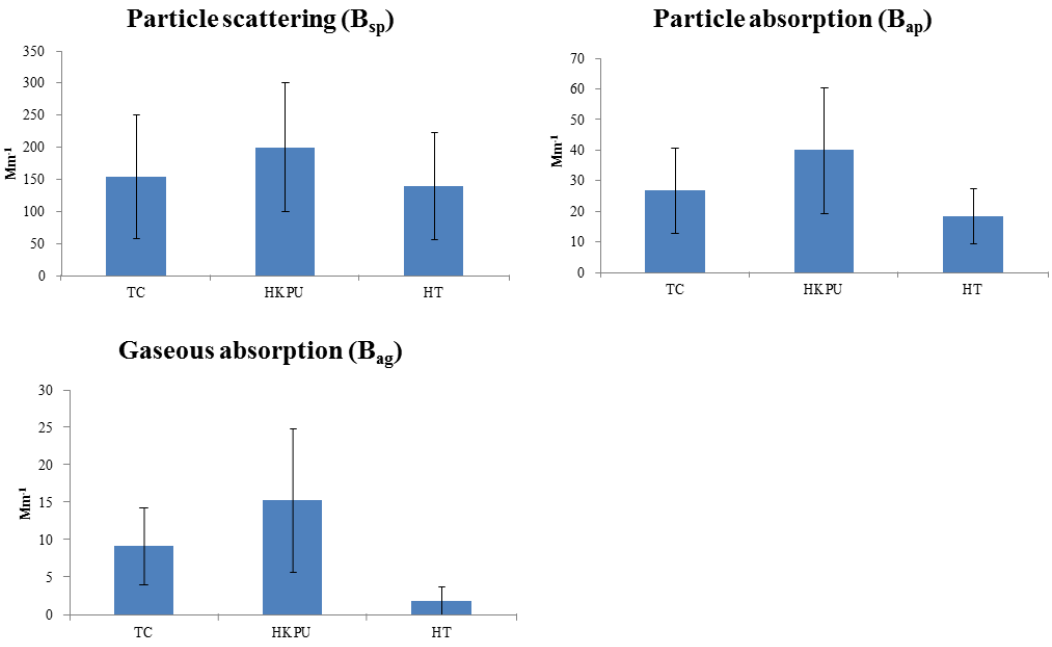

Figure 4.2 Difference in B_{ext} components among sites

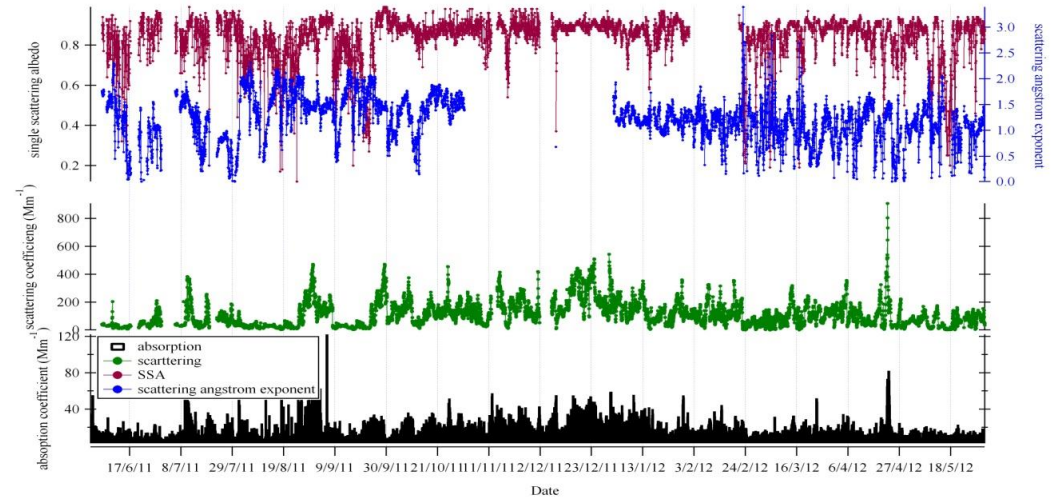
single scattering albedo
scattering angstrom exponent
scattering coefficieng (Mm-1)
absorption coefficient (Mm-1)
absorption
scarttering
SSA
scattering angstrom exponent
17/6/11 8/7/11 29/7/11 19/8/11 9/9/11 30/9/11 21/10/11 11/11/11 2/12/11 23/12/11 13/1/12 3/2/12 24/2/12 16/3/12 6/4/12 27/4/12 18/5/12
Date

(a) HT

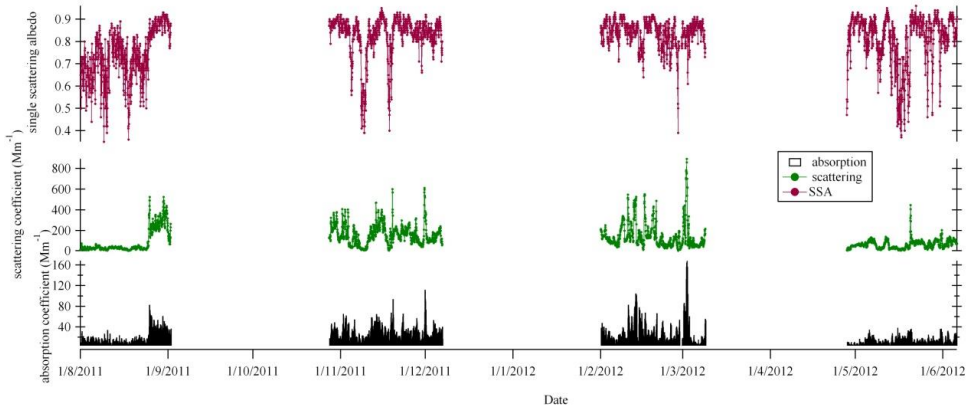
single scattering albedo
scattering coefficient (Mm-1)
absorption coefficient (Mm-1)
absorption
scattering
SSA
1/8/2011 1/9/2011 1/10/2011 1/11/2011 1/12/2011 1/1/2012 1/2/2012 1/3/2012 1/4/2012 1/5/2012 1/6/2012
Date

(b) TC

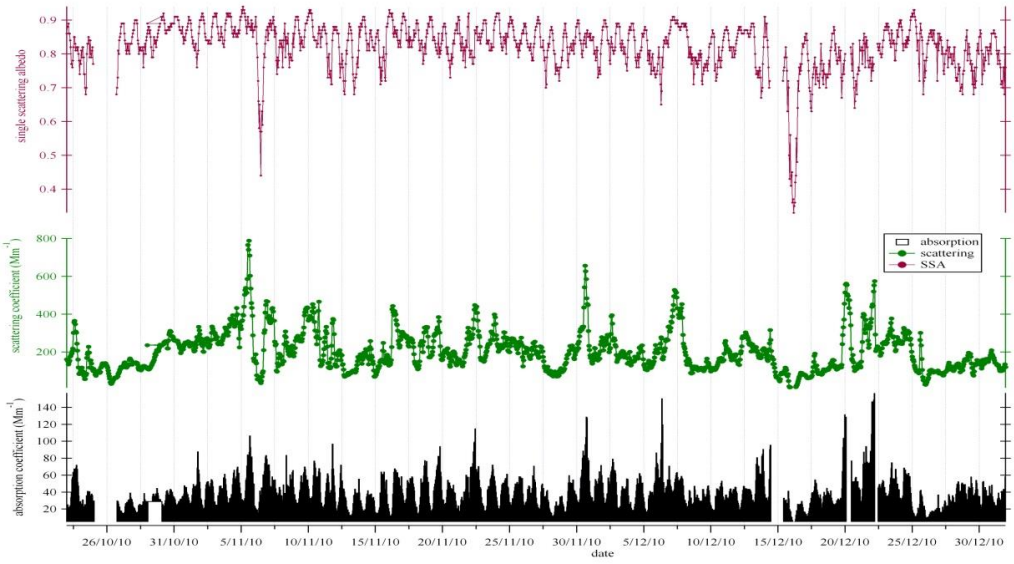

(c) HKPU

Figure 4.3: Time series of B_{sp}, B_{ap} and single scattering albedo (SSA, ω) in a) HT, b) TC and c) HKPU

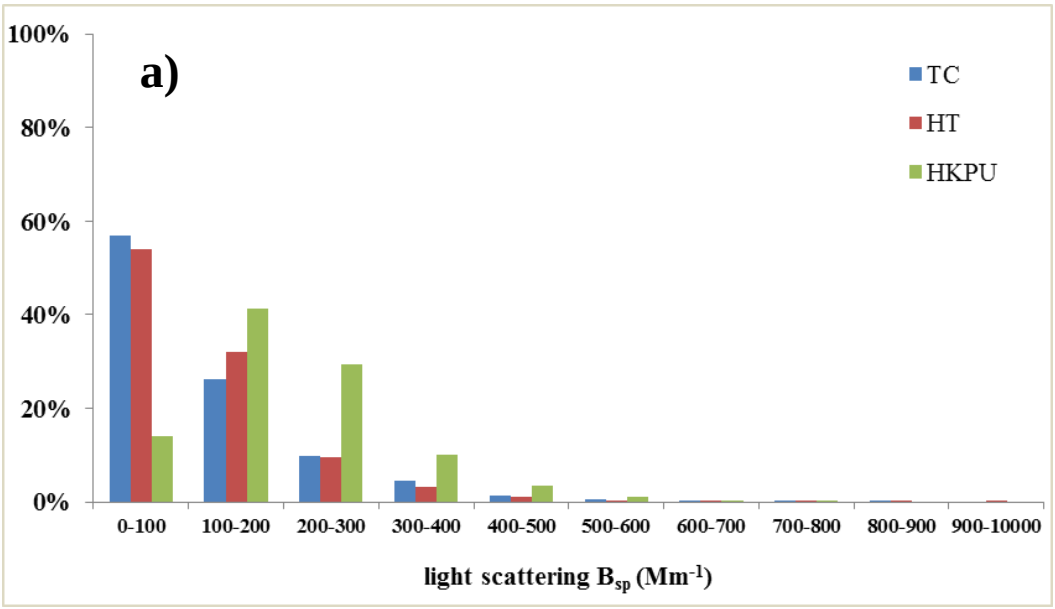

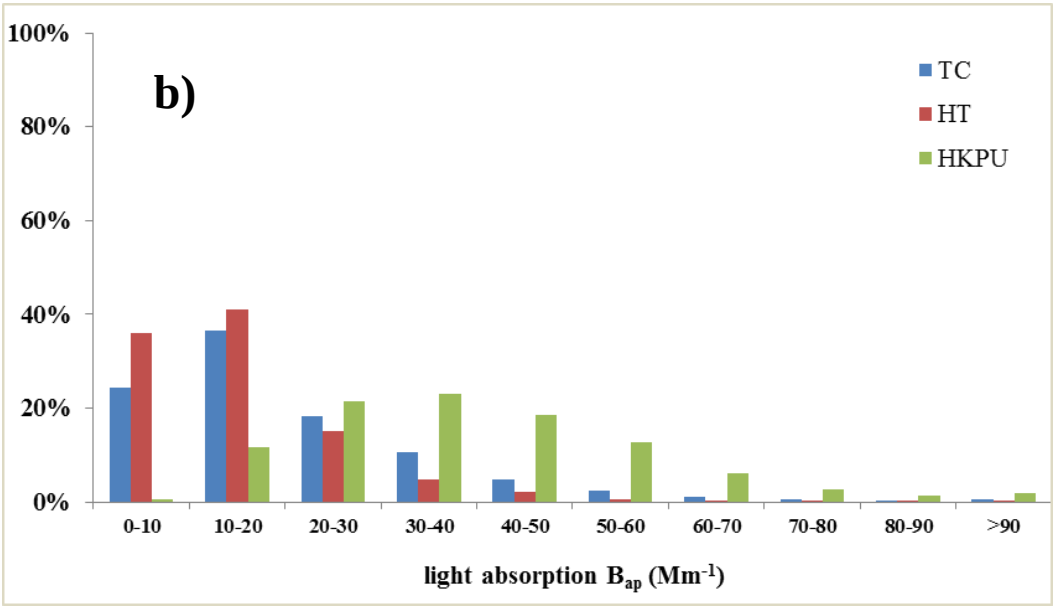

Figure 4.4: a) Distribution of particle light scattering (B_{sp}) at HT, TC and HKPU; b) Distribution of particle absorption coefficient (B_{ap}) at HT, TC and HKPU

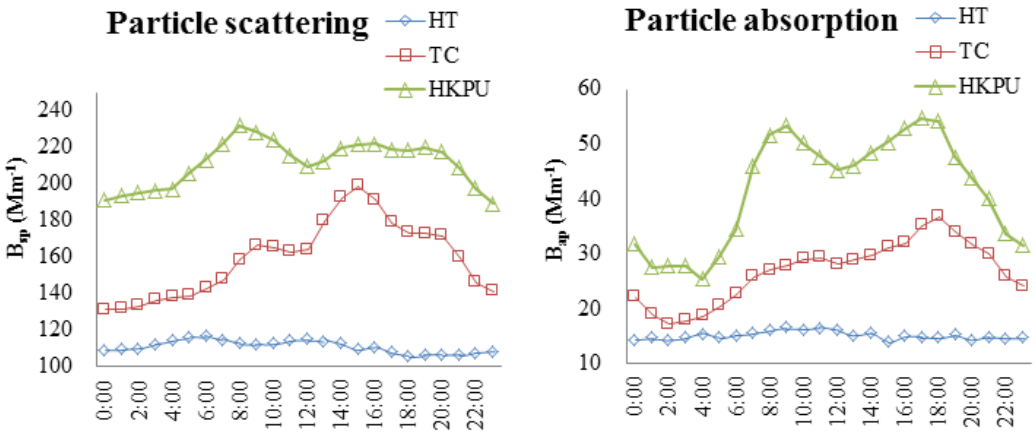

Figure 4.5 a) Diurnal variations of particle scattering coefficient (B_{sp}) at HT, TC and HKPU; and b) Diurnal variations of particle absorption coefficient (B_{ap}) at HT, TC and HKPU

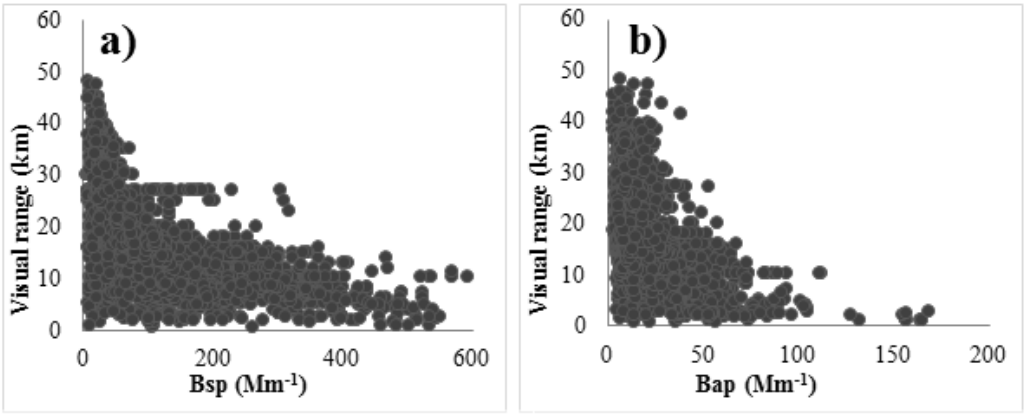

(a) scattering coefficient versus visual range (b) absorption coefficient versus visual range

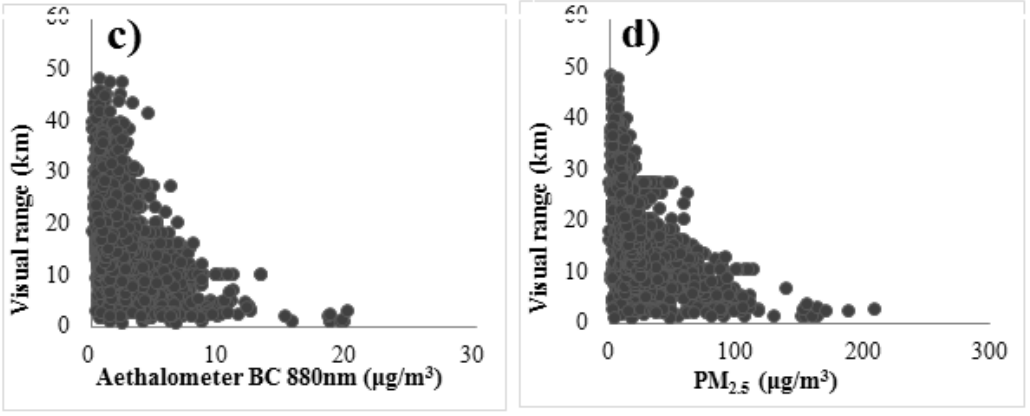

(c) BC concentration versus visual range (d) $PM_{2.5}$ concentration versus visual range

Figure 4.6 Relationships between visual range and a) B_{sp}, b) B_{ap}, c) black carbon (BC) and d) $PM_{2.5}$ at TC

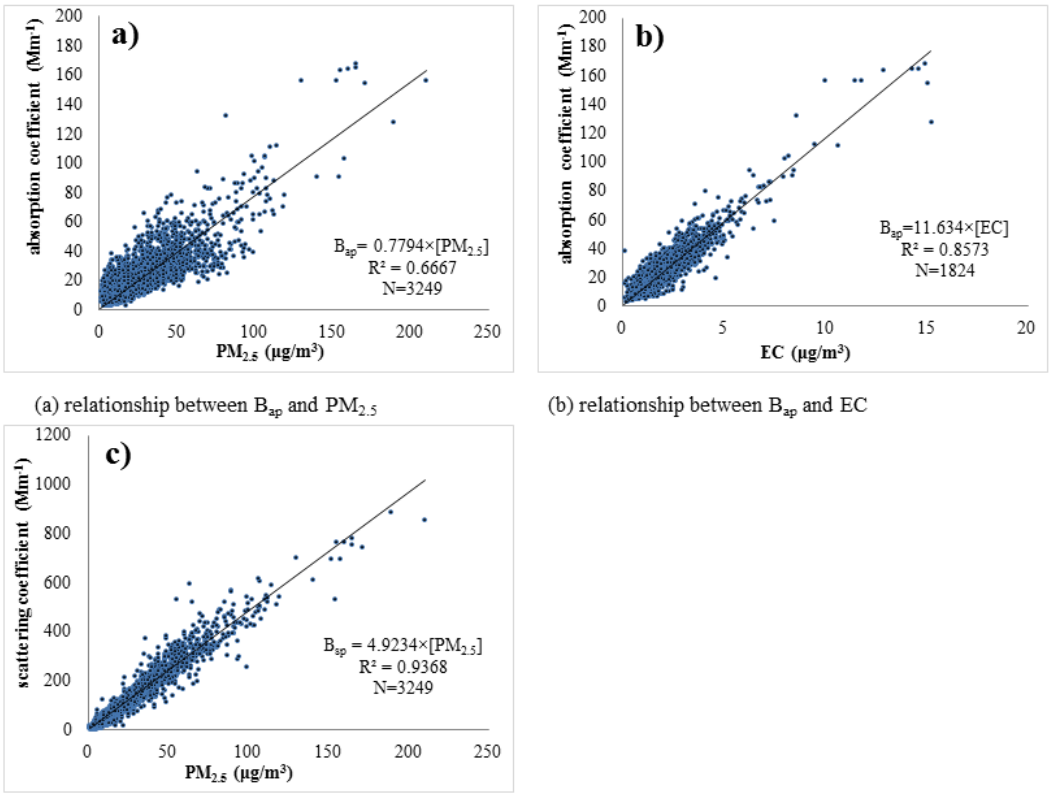

(a) relationship between B_{ap} and $PM_{2.5}$

(b) relationship between B_{ap} and EC

(c) relationship between B_{sp} and $PM_{2.5}$

Figure 4.7 Relationships between a) B_{ap} and $PM_{2.5}$, b) B_{ap} and EC; c) B_{sp} and $PM_{2.5}$

Table 4.1 Statistical summary of B_{ap}, B_{sp}, SSA (ω) and scattering Angström exponent (α_s) for HT a) HT, b) TC and c) HKPU; all data calculated on 1-hour averaged data

a)

HT	scattering (B_{sp} 550nm) Mm^{-1}	absorption (B_{ap} 550nm) Mm^{-1}	single scattering albedo (SSA ω)	scattering angstrom exponent (α_s 450-700nm)
Average	110.84	15.12	0.84	1.23
SD	89.19	9.85	0.11	0.42
Max	907.11	122.35	0.99	3.39
Min	2.09	2.23	0.12	0.00
Median	90.75	12.60	0.87	1.25
Hours	7909	7914	6371	7853

b)

TC	scattering (B_{sp} 550nm) Mm^{-1}	absorption (B_{ap} 550nm) Mm^{-1}	single scattering albedo (SSA ω)
average	116.48	21.08	0.81
SD	106.60	16.45	0.11
Max	892.04	168.23	0.96
Min	5.67	3.36	0.35
Median	86.05	16.35	0.84
Hours	3539	3533	3520

c)

HKPU	scattering (B_{sp} 550nm) Mm^{-1}	absorption (B_{ap} 550nm) Mm^{-1}	single scattering albedo (SSA ω)
Average	201.96	39.91	0.82
SD	105.82	19.16	0.07
Max	788.91	156.95	0.94
Min	2.43	4.77	0.33
Median	183.04	36.99	0.83
Hours	1679	1600	1600

Table 4.2 Particles B_{ap}, B_{sp}, SSA (ω) measured in the other sites

Site	Period	B_{sp} (Mm^{-1})	B_{ap} (Mm^{-1})	SSA ω	Instrumentation	References
Rural area						
Lin'an, China	1999.11	353	23	0.93	• PSAP, Radiance Research, M903 • Nephelometer, Radiance research	(Xu et al., 2004)
Yulin, China (Gobi desert)	2001.4	158	6	0.95	• PSAP, Radiance Research, M903 • Nephelometer, Radiance research	(Xu et al., 2004)
Shangdianzi, China	2003.9-2005.1	174.6	17.54	0.88	• AE-31, Magee scientific • M9003 Nephelometer EcoTech	(Yan et al., 2008)
Cape D'Aguilar, Hongkong	1997.1-1998.2	20	56	0.72	• PSAP, Radiance Research, M903 • Nephelometer, Radiance research	(Man and Shih, 2001)
Xinken, China	2004. 10-11	333	70	0.83	● 3563 Nephelometer, TSI, Inc. ● 5012 MAAP, Thermo, Inc.	(Cheng et al., 2008)

Tai O, Hong Kong	2002.10-12	224	22.1	0.92	• NGN-2 nephelometer, Optec. Inc. • PSAP, Radiance Research, M903	(Wang T. 2003)
Mukteshwar, India	2005.9-2007.9	24.6-94.3	4.5-20.3	0.75-0.85	• M9003 Nephelometer, EcoTech • AE-31 Magee scientific	(Hyvärinen et al., 2009)
Urban area						
Beijing, China	1999.6	488	83	0.81	• PSAP, Radiance Research, M903 • Nephelometer, Radiance research	(Bergin et al., 2001)
Guangzhou, China	2004. 10-11	418	91	0.80	• Nephelometer, Radiance Research, • M903 PAS	(Andreae et al., 2008)
Shanghai, China	2010.12-2011.3	293	66	0.81	• AE-31 Magee Scientific, • M9003 Nephelometer, Eco Tech	(Xu et al., 2012)
Thessaloniki and Crete, Greece	1998.8	80	15	0.89	• 3563 Nephelometer, TSI. • PSAP Radiance Research	Formenti et al., 2002

Gosan, Korea	Episode in 2001	244			• 1597 Nephelometer • Belfort AE-14U Magee scientific	Kim et al., 2004
Atlanta, USA	1999. 8	120	16	0.88		Carrico et al., 2002
Southern Mexico City	2005.2-8	20.6-93.3	12.0-29.4	0.59-0.83	• PASP, Radiance Research, M903 • Nephelometer, Radiance research	(Garcia et al., 2010)
Granada, Spain	2006.3-2007.2	61	24	0.71	● 3563 Nephelometer, TSI, Inc. ● 5012 MAAP, Thermo, Inc.	(Titos et al., 2012)

Table 4.3 Seasonal average of B_{sp}, B_{ap}, SSA (ω) at a) HT and b) TC

a) HT

HT	B_{sp} (550nm)	B_{ap} (550nm)	SSA, ω (550nm)
summer	81.7 ± 93.3	15.1 ± 14.1	0.78 ± 0.11
autumn	142.6 ± 78.0	18.4 ± 8.4	0.87 ± 0.06
winter	93.8 ± 65.2	13.9 ± 5.7	0.82 ± 0.12
spring	66.5 ± 3.2	10.6 ± 3.2	0.80 ± 0.14

Remark: the summer time is from June to August 2011, the autumn is from September to November 2011, the winter is from December 2011 to February 2012 and the spring is from March to May of 2012

b) TC

TC	B_{sp} (550nm)	B_{ap} (550nm)	SSA, ω (550nm)
summer	99.28 ± 120.8	18.60 ± 14.0	0.75 ± 0.11
autumn	159.28 ± 95.5	26.85 ± 13.9	0.83 ± 0.09
winter	148.51 ± 126.8	26.72 ± 22.0	0.84 ± 0.05
spring	65.39 ± 41.7	12.64 ± 6.7	0.81 ± 0.11

Remark: August, November, February and May represent the four seasons, which are summer, autumn, winter and spring

Chapter 5. Chemical characteristics of size-resolved particles in Hong Kong

5.1 Introduction

The particle size and chemical components are the key factors causing direct and indirect effects on earth's radiative balance, visibility impairment, climate change and human health (Huang and Yu, 2008; Malm and Pitchford, 1997; Milford and Davidson, 1987; Penttinen et al., 2001; Seinfeld and Pandis, 2006; Sloane et al., 1991; Watson, 2002). Size-resolved particles are usually used to discuss formation mechanism with physical and chemical characteristics. Previous studies have focused on $PM_{2.5}$ chemical components, e.g., sulfate [SO_4^{2-}], nitrate [NO_3^-], and organic carbon, elemental carbon and mineral of their detailed size distributions (Howell and Huebert, 1998; Huang et al., 2006a; John et al., 1990; Kim et al., 2003; Plaza et al., 2011; Tang, 1996; Tsai et al., 2012; Wang et al., 2013). Past Hong Kong studies have shown SO_4^{2-}, POM, OC and EC with high concentrations in the submicron-mode, that is the largest contributor to B_{ext} (Gao et al., 2015; Yao et al., 2002; Yao et al., 2003b; Zhuang et al., 1999b). Chow et al. (2008) observed different SO_4^{2-} size distributions in different environments, i.e. a wide multi-modal distribution at a California urban site but a narrow uni-modal distribution at a California rural site. Size-distributions of three inorganic compounds (i.e., SO_4^{2-}, NO_3^-, and NH_4^+) at the same site changed over a 20-year period (Bian et al., 2014). Zhuang et al., (1999a) used the Mirco-Orifice Uniform Deposit Impactor (MOUDI) at a Hong Kong rural site to find 35% of the total sulfate in coarse mode (1.8 μm

to 10 μm) and ~65% in the fine mode (< 1.8 μm). Since the site was near coast, some of the size distributions for sulfate, nitrate and ammonium were also addressed (Zhuang et al., 1999b). $PM_{2.5}$ chemical compositions were measured at Hong Kong roadside, urban (Cheng et al., 2011; Ho et al., 2006b; Lee et al., 2006) and rural sites (Louie et al., 2005; Wong et al., 2011). Engine exhaust, secondary aerosols, residual oil combustion, fresh and aged sea salt, soil, coal combustion and biomass burning were the main $PM_{2.5}$ sources derived from these compositions. A few contributions to different size ranges (Contini et al., 2014; Han et al., 2006; Kim et al., 2003), outside of Hong Kong. This chapter focuses on: 1) investigating the particle size distribution of water-soluble ions and carbon; 2) determining size modes by PMF applied to MOUDI (Model 110, MSP Corp. Minnesota, U.S.A.) data in Hong Kong.

5.2 Result and discussions

5.2.1 Particle mass and chemical components

Figure 5.1 shows PM_{10} concentration from each size mode at TC in four seasons. The droplet mode (0.56 -1.8 μm) accounted for 27-59% of PM_{10} mass, followed by 10-42% from the condensation mode (0.1-0.56 μm), and then by 10-34% from the coarse modes (1.8-10 μm). Average $PM_{1.8}$ and PM_{10} concentrations are summarized in Table 5.1 for each season. $PM_{1.8}$ average ranged from 26 $\mu g/m^3$ in spring to 37 $\mu g/m^3$ in fall. PM_{10} average ranged from 39 $\mu g/m^3$ in spring to 53 $\mu g/m^3$ in fall. Approximately 39% of the samples exceeded the 24-hour PM_{10}

standard/guideline of 50 μg/m^3 as set by the European Union and WHO. $PM_{1.8}$ and PM_{10} concentrations at TC were ~20 - 60% lower than those at Hong Kong urban sites (Chow et al., 2010b; Ho et al., 2006; Louie et al., 2005). Comparable $PM_{2.5}$ concentrations were found at the Tai'O (41 μg/m^3) and Tung Chung (37 μg/m^3) sites (Cheung et al., 2005), with fine particles ($PM_{2.5}$) to PM_{10} ratios averaging 0.72 ± 0.09, and ranging from 0.46 to 0.88.

Reconstructed PM_{10} mass concentrations correlated well (R^2 = 0.8) with measured PM_{10} mass concentrations. Figure 5.2 shows that the most abundant species was SO_4^{2-}, constituting about 26 - 37% of PM_{10} mass. The second largest chemical component of PM_{10}, POM accounted for 8 - 10% in spring and winter months and 24 - 29% in fall and summer months. Because NO_3^- is a semi-volatile compound, it had a lower contribution to PM_{10} mass in summer and spring periods. Sea salt contributed its largest fraction in spring (~31%) and was the lowest in winter (11%). Sea salt fractions of PM_{10} during summer and fall were ~ 14%. The soil contribution ranged from 5% in spring to 10 - 11% in summer and fall. There were no apparent seasonal variations for NH_4^+ (2 - 5%), EC (5%), TEO (1 - 2%), or K^+ (0 - 1%). Differences between reconstructed and measured PM_{10} (i.e., others) were higher in winter and spring (9-18%). These differences may be due to liquid water retention by hygroscopic sulfate, nitrate, and sea salt (Chow et al 2015).

5.2.2 Summer pollution episode in sub-urban area

The highest average concentration of PM_{10} (80 ± 13 μg/m^3) was found during the summer hazy days, with a $PM_{1.8}/PM_{10}$ ratio of 0.78 ± 0.04. As shown in Table

5.1, both $PM_{1.8}$ and PM_{10} concentrations were 3-4 fold higher during pollution episodes, but the ratio of $PM_{1.8}$ to PM_{10} decreased from 0.83 ± 0.02 (clean day) to 0.78 ± 0.04 (episode day), indicating larger particle sizes for the polluted days. As illustrated in Figure 5.3, the ratio of each size mode to PM_{10} changed from the clean day to the end of the pollution episode. The fraction contributed by the condensation mode particle decreased from ~31 to ~18% between the beginning and end of the episode. This decrease was offset by an increasing contribution from the droplet mode of ~42% to ~52% and an increase (~19% to 24%) in the coarse mode. This may have been caused by aqueous chemistry processing during the pollution episode. The contributions from POM and EC summed to 44% at the beginning of the episode and decreased to 24% at the end. The SO_4^{2-} contribution increased from 17% to 41%, showing the importance of secondary particle formation in the transported air masses. Figure 5.4 shows a remarkable high sulfur oxidation ratio (SOR) for the droplet mode during the polluted days, indicating of reactions in the liquid phase. Due to higher summertime temperatures that shift NO_3^- to the gas phase, the nitrogen oxidation ratio (NOR) value did not exhibit much change. The 3-day back trajectories identify the emission source regions during the clean and pollution episode days (Figure 5.3). For the clean days, the air mass originated from the ocean, bringing uncontaminated air to TC. During the polluted days, a slowly moving air mass passed over the PRD region, combining high emissions with low dispersion and low dilution meteorology.

5.2.3 Wintertime similarity and difference at TC and HKPU

Average concentrations at TC and HKPU during winter period varied from 52.44 to 77.31 μg/m^3 for PM_{10} and from 34.51 to 52.11 μg/m^3 for $PM_{1.8}$ (Table 5.2). The highest daily PM_{10} and $PM_{1.8}$ levels were observed at HKPU, 99.19 and 69.99 μg/m^3, respectively. Recently, the Hong Kong government has established air quality standard for $PM_{2.5}$, which is 75 μg/m^3 daily average. Same value is for Chinese air quality standard. During the whole year, only ~10% of the daily $PM_{2.5}$ concentrations in HK exceeded 75 μg/m^3. The average $PM_{1.8}$ concentrations measured in HKPU were higher than those at TC, probably due to higher traffic flows and stronger dilution winds at TC. Similar $PM_{1.8}/PM_{10}$ ratios were observed at HKPU and TC sites, 0.67 and 0.7, similar to those found by Ho et al. (2003) at the HKPU, and KT sites. The chemical mass balance was calculated in the two sites, which is shown in Table 2 and Table 3. Chemical contribution at the two sties SO_4^{2-} in $PM_{1.8}$/ SO_4^{2-} in PM_{10} are 83% and 81% at HKPU and TC, respectively. $PM_{1.8}/PM_{10}$ ratios for NH_4^+, EC, and POM and trace element oxides (TEOs) are around 0.9 at both sites, indicating the most of the sulfates, ammonium, EC and POM are in fine particle fraction. Natural emission sources, such as, sea salt and soil dust have lower $PM_{1.8}/PM_{10}$ ratios, consistent with other findings of their presence in the coarse mode $PM_{1.8}/PM_{10}$ for NO_3^- was also low, the reaction of HNO_3 with sea salt. Variation of the size distributions appear to be similar for all species at both sites.

Figure 5.5 shows that POM and EC constituted ~40% of PM_{10} fraction at the HKPU site, but only 13% of PM_{10} fraction at TC, again consistent with traffic activities contributions at the HKPU site. The relative high fraction of soil dust at HKPU site was also consistent with road dust suspension, as well as nearby construction activity. PM_{10} at TC was dominated by secondary pollutants, i.e. SO_4^{2-}, NH_4^+ and NO_3^-, ~60% of PM_{10}.

5.2.3 Particle size distributions in Hong Kong

The PMF solution has been previously applied to particle size distributions (Garrido Frenich et al., 2000; Huang et al., 2006b; Huang et al., 2006d; Kim et al., 2003; Yu et al., 2010). A total of 224 samples (32 sets × 7 species (i.e. ions and carbon)) were used as PMF input. In general, the three or four size modes are often observed in the ambient particles in each of the nucleation mode, condensation mode, droplet mode, and coarse mode. The particle origination and its formation mechanism can be estimated based on the particle size distribution. For example, the in-cloud process or aqueous reaction mainly happened in droplet mode particle (Hering and Friedlander, 1982; Seinfeld and Pandis, 2006). The PMF resolved three modes based on Hong Kong data is shown in Figure 5.6, with mass median aerodynamic diameters (MMAD) and standard deviation (σ) of 0.4 μm (σ = 1.42), 0.7 μm (σ = 1.32) and 3.8 μm (σ = 1.38), respectively. The narrower particle size range was seen based on the small standard deviation (σ). In Shenzhen and Beijing urban area, similar MMADs of droplet (0.84 μm) and condensation (0.34 μm) modes have been observed, with narrowly distributed droplet mode (σ = 1.39), but

the MMADs for the coarse mode at Beijing and Shenzhen were 5.4 μm and 5.7 μm, respectively, which larger than the Hong Kong coarse mode MMAD (Guo et al., 2010; Lan et al., 2011), indicating the presence of more aged particles in the coarse mode in Beijing and Shenzhen.

In order to understand the size distribution on major chemical components in Hong Kong, 7 species (SO_4^{2-}, NO_3^-, NH_4^+, Cl^-, K^+, OC and EC) were used to analyze size distributions with the PMF model (Figure 5.7). SO_4^{2-} was dominant for the droplet mode (0.8 μm, σ=1.2), with two smaller peaks in the condensation and coarse modes (Figure 5.7(a)). The characteristics of SO_4^{2-} size distributions were previously indicated condensation mode formation conversions for SO_2 to SO_4^{2-} (Lan et al., 2011; Seinfeld and Pandis, 2006); in the droplet mode, the oxidation of SO_2 was formed by aqueous processes (John et al., 1990; Kerminen and Wexler, 1995; Zhuang et al., 1999b), because usually H_2SO_4 reacts with sea salt and soil dust to form coarse-mode sulfate (Zhuang et al., 1999a). This resolved SO_4^{2-} size distribution was similar to previously-observed Hong Kong and mainland China distributions (Guo et al., 2010; Lan et al., 2011; Yao et al., 2003a; Zhuang et al., 1999b), which attributed ~60% of SO_4^{2-} to aqueous formation in droplet, ~25% to gas phase reaction, and ~15% to sulfuric acid reactions by soil dust and sea salt.

The potential pathways to form nitrate include processes and condensation onto pre-existing particles. Because of the characteristics of NO_3^-, the key determining factor for NO_3^- size distribution is the thermodynamic equilibrium described in the following equation (John et al., 1990; Seinfeld and Pandis, 2006):

$$HNO_3\ (g) + NH_3\ (g) \longleftrightarrow NH_4NO_3\ (s, aq) \qquad (5.1)$$

When the gaseous ammonia (NH_3) and nitric acid (HNO_3) are sufficient, T is low and RH is high, NH_4NO_3 is preferred form (Zhuang et al., 1999b). Two NO_3 peaks were found with the coarse mode accounting for ~67% of total NO_3^-, and the droplet mode NO_3^- contributing 33% of the total NO_3^- (Figure 5.7(b)). The coarse mode NO_3^- is stable, unlike NH_4NO_3, which explains why only a few condensation peaks were observed in this study.

The sulfur oxidation ratio (SOR) and the nitrogen oxidation ratio (NOR) are indicators of PM formation mechanisms. Higher SOR and NOR values indicate larger amounts of secondary formation via photochemical oxidation of SO_2 and NO_2 precursor gases, respectively (Kadowaki, 1986; Khoder, 2002). The conversion equation was described as followed:

$$SOR = \frac{[{SO_4}^{2-}]}{[{SO_4}^{2-}+SO_2]} \qquad (5.2)$$

$$NOR = \frac{[{NO_3}^{-}]}{[{NO_3}^{-}+NO_2]}, \qquad (5.3)$$

where SO_4^{2-}, sulfur dioxide (SO_2), NO_3^- and nitrogen dioxide (NO_2) are expressed in units of mol/m^3. Figure 5.8 shows the value of the SOR and NOR for the condensation, droplet and coarse modes. The SOR and NOR are smaller in spring and summer, with higher values in fall and winter period. Smaller NOR

values were observed in spring and summer compared with fall and winter, but the opposite patterns for SOR value in the four seasons, which indicating the varied pollutant removal mechanism and formation process for the two species, SO_4^{2-} and NO_3^-. High temperatures (23-29 ºC in summer and spring) favor SO_4^{2-} formation, but enhance NH_4NO_3 volatilization. When temperature increases, the correlation between particle size and temperature decreases and R^2 declined from 0.6 in coarse mode to 0.5 in condensation mode. The highest SOR corresponded with the droplet mode, which was ~60% higher than that for the condensation and coarse modes. NOR was higher in the coarse mode resulting from sodium nitrate, calcium nitrate formed through nitric acid reactions with seal salt and soil dust present in the coarse mode.

The observed NH_4^+ and K^+ were in the droplet mode (Figure 5.7(c), (d)). The incomplete neutralization occurred between NH_4^+ and SO_4^{2-}, because the molar ratio of NH_4^+ to SO_4^{2-} in fine mode was 1.0, instead of 2 for $(NH_4)_2SO_4$. The remaining may be ammonium bisulfate and sulfuric acid (Liu et al., 2008). K^+ is a biomass burning marker, which is applicable to the PRD region (Andreae, 1983; Huang et al., 2006b; Lan et al., 2011; Novakov and Corrigan, 1996). The presence of condensation mode K^+ is consistent with fresh emissions of biomass burning. The droplet mode K^+ correlated with SO_4^{2-} (R = 0.8), indicating aging with sulfate. There is a small peak of coarse mode K^+, may be due to soluble potassium in sea salt (Bian et al., 2014). Because of increasing chloride depletion with decreasing particle size, a single coarse mode Cl^- was observed (Figure 5.7(e)), deriving from local sea salt emission (Yao et al., 2003b).

EC showed a bi-modal size distribution pattern (Figure 5.7(f)). Concentrations of condensation EC (0.28 μm) and droplet EC (0.8 μm) were 0.5 and 0.6 μg/m^3, respectively. The dominant droplet mode EC had a high correlation with SO_4^{2-} (R = 0.72), which may relate to residual oil combustion in marine engines. PRD studies indicate EC and SO_4^{2-} are internally mixed through aqueous processes (Cheng et al., 2006; Huang and Yu, 2008). Fresh engine emission is the major EC source. The similar observations apply to Shenzhen (Huang and Yu, 2008). Mass concentration of OC in condensation, droplet and coarse modes were 1.9, 2.0 and 0.4 μg/m^3, respectively. Abundance of droplet mode was also apparent for OC, followed by a condensation mode.

5.3 Summary

Size-segregated samples were collected using a 10-stage Micro-Orifice Uniform Deposit Impactor (MOUDI) in Hong Kong. The gravimetric mass, water-soluble ions, organic and elemental carbon, and elements were analyzed. In this Chapter, the chemical species profile and its contribution to PM_{10} were calculated via the chemical mass closure method in urban and sub-urban areas to discuss its seasonal variations and pollution episode situation. In addition, the resolved size distribution of major chemical species was investigated using the positive matrix factorization (PMF) model.

The results show distinctive seasonal variations of PM_{10} chemical composition in sub-urban areas. Highest PM_{10} concentrations were found in the fall with lowest

PM_{10} concentrations in the spring. Secondary sulfate and particle organic matters (1.8 × OC) were the two largest components of PM_{10}, account for 26-37% and 8-30% of PM mass. One pollution episode was observed during the summer period of sub-urban site. The origin of the pollution source is from PRD with stagnant meteorological air. The elevated aged particles were transported to the site with many secondary pollutants.

During the winter period, the PM_{10} and $PM_{1.8}$ concentrations in urban area are very high compared with other European and U.S. cities. Moreover, the mean $PM_{1.8}/PM_{10}$ mass ratio was similar in urban and sub-urban site. The most dominated chemical species in Hong Kong PolyU site is POM and EC, due to high traffic flow, but secondary particles are the dominated chemical species in TC site with small fraction of primary emission, due to pollutants regional transportation.

The three particle size modes for particulate mass were resolved via PMF model. The mass median aerodynamic diameters were 0.4, 0.7, and 3.8 μm for the condensation, droplet and coarse modes, respectively with a similar width of distribution (i.e., standard deviation, σ, ranging 1.32 - 1.42). Moreover, the size distribution of major chemical components (e.g. SO_4^{2-}, NH_4^+ and OC) was also investigated. Droplet mode was found to be the most prominent mode for SO_4^{2-}, NH_4^+, K^+, OC and EC. NO_3^- was present in both the droplet and coarse modes, whereas Cl^- was found to be present solely in the coarse mode, indicative of sea salt contribution.

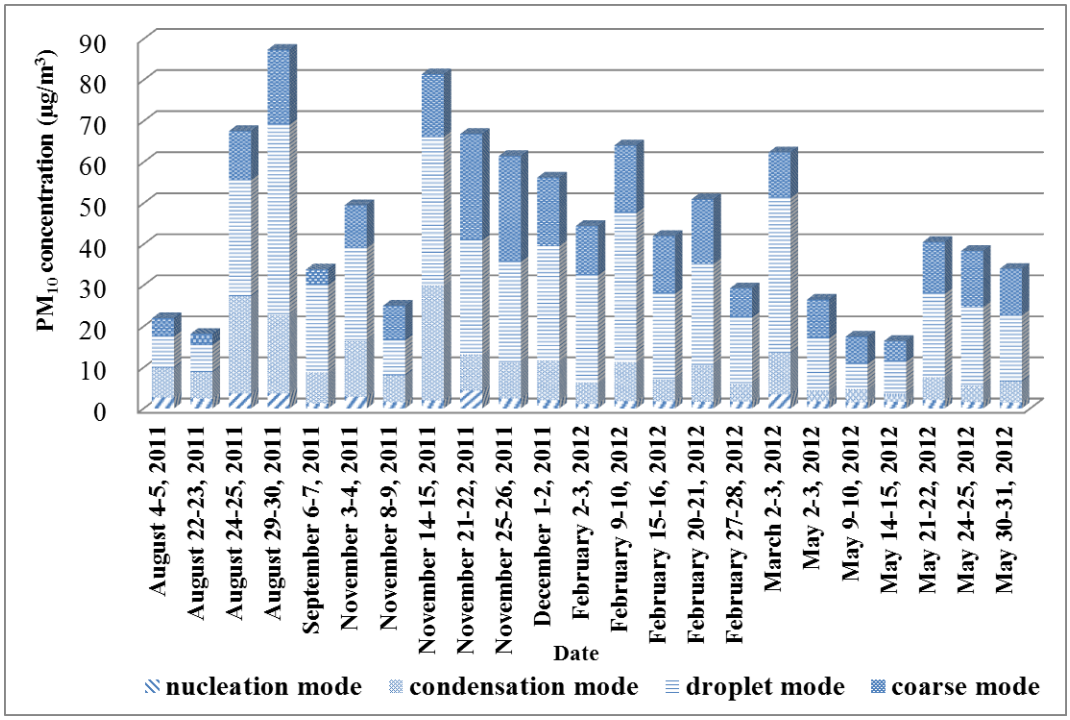

Figure 5.1 Time series of PM_{10} concentrations in four modes of size distribution at TC (Particle size modes are defined as: 0.056 -0.1 μm for the nucleation mode, 0.1-0.56 μm for the condensation mode, 0.56-1.8 μm for the droplet mode, and 1.8-10 μm for the coarse mode)

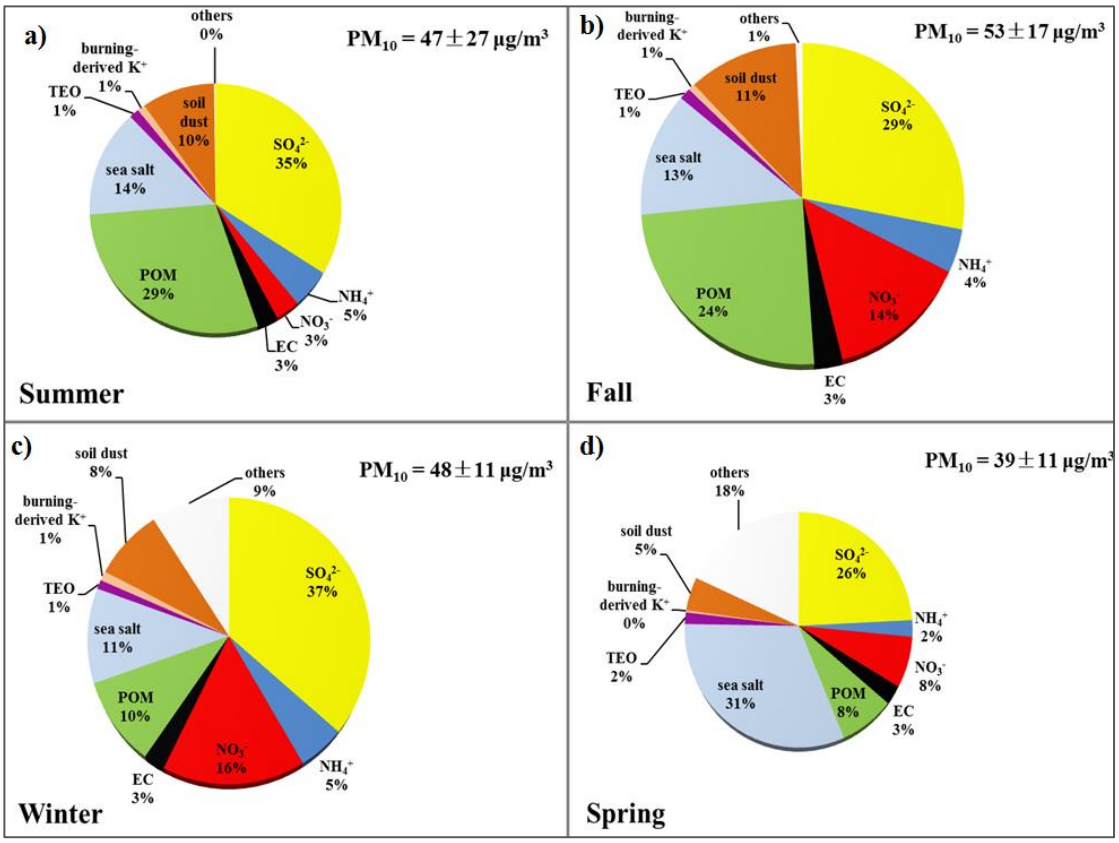

Figure 5.2. Reconstructed PM_{10} mass for: a) summer, b) fall, c) winter and d) spring. The components include sulfate, nitrate, ammonium, Particle organic matters ($POM = 1.8 \times OC$), EC, water-soluble potassium, trace element oxides ($TEO = 1.3 \times [0.5 \times (Sr + Ba + Mn + Co + Rb + Ni + V) + 1.0 \times (Cu + Zn + Mo + Cd + Sn + Sb + TI + Pb + As + Se + Ge + Cs + \mathrm{Ga})]$, sea salt ($sea\ \ salt = 1.8 \times \mathrm{Cl^-}$), soil ($soil\ \ = 2.20 \times Al + 2.49 \times Si + 1.63 \times Ca + 2.42 \times Fe + 1.94 \times Ti$)

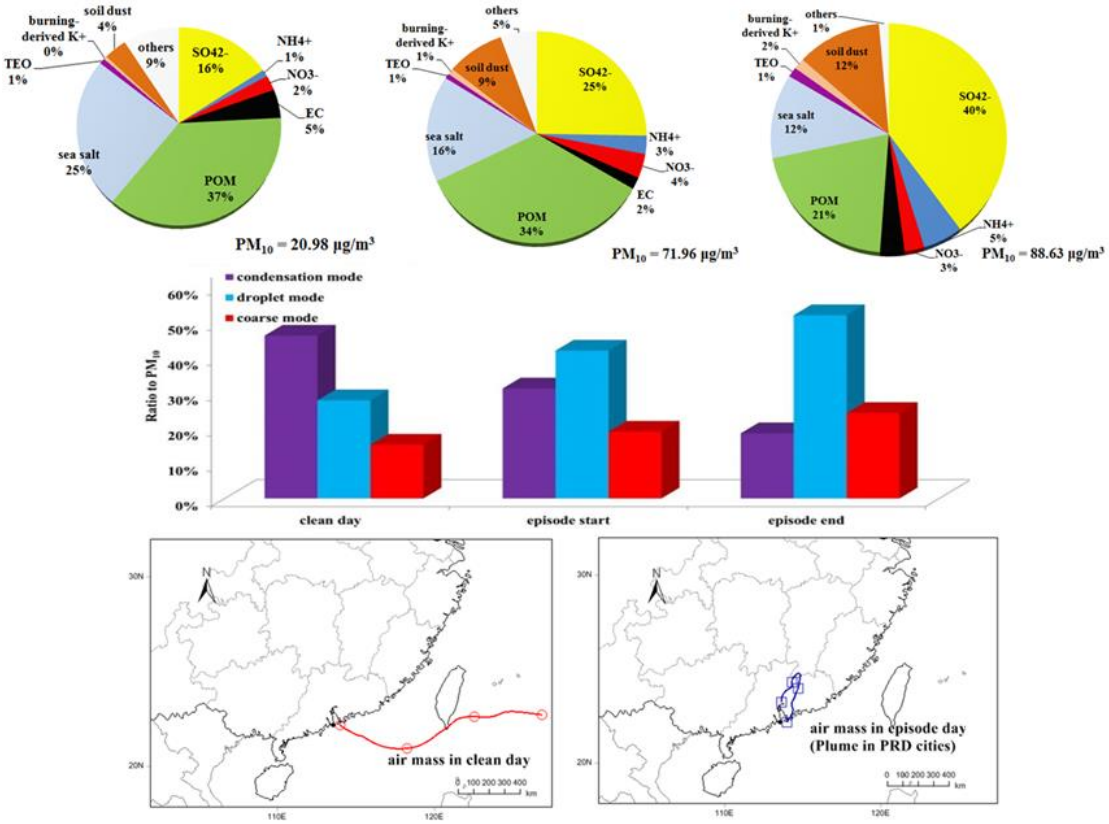

Figure 5.3 Reconstructed PM mass for a clean air mass August 20th, and for a polluted air mass transported from August 24th, to August 29th. Abundances in each of four size modes corresponding to the back trajectories are shown

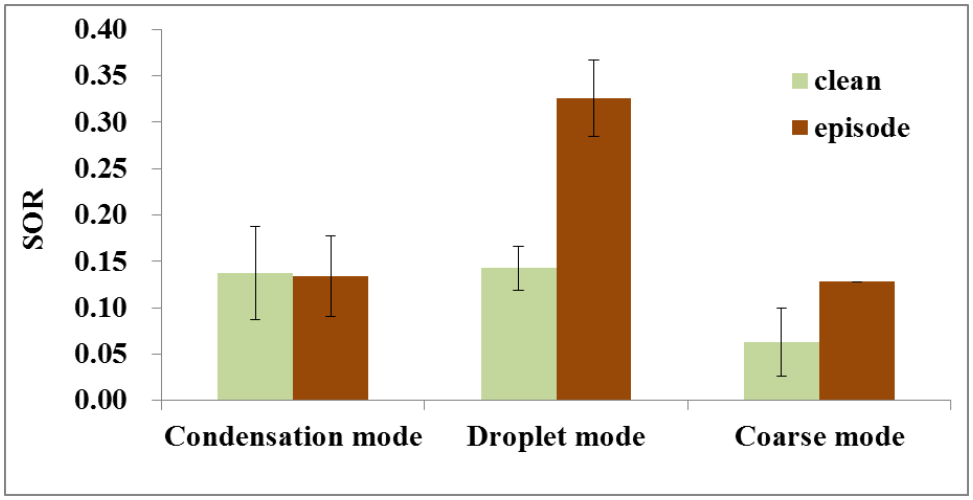

Figure 5.4 Size-fractionated sulfur oxidation ratio (SOR) value for clean and polluted episode days in TC

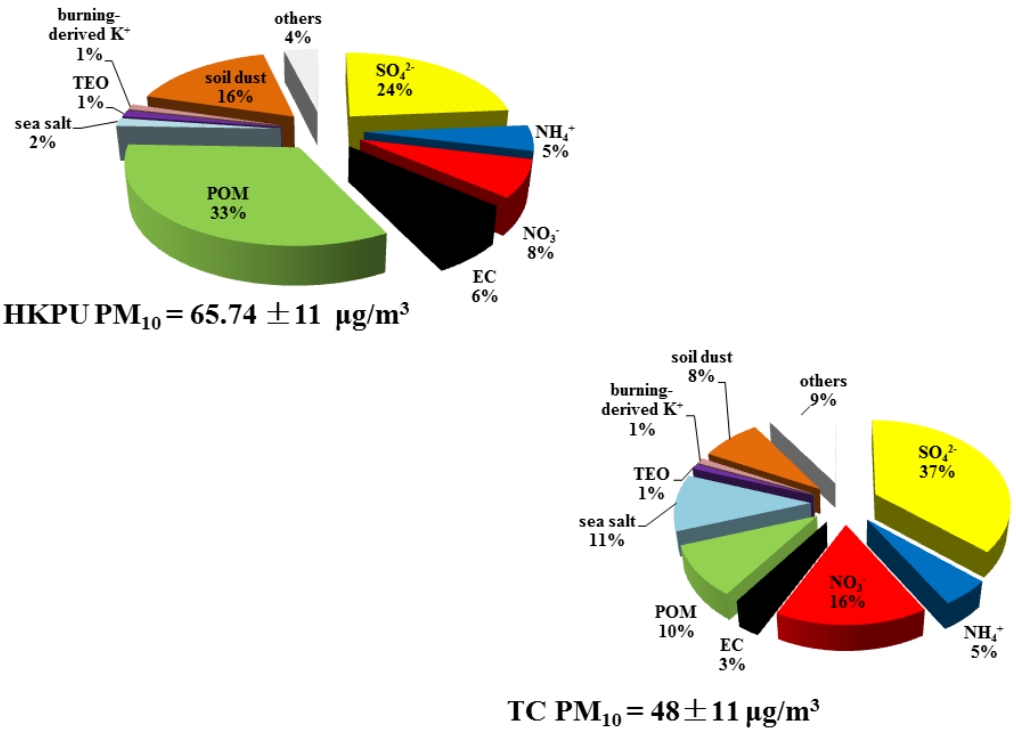

Figure 5.5 Reconstructed PM_{10} mass at HKPU and TC during winter period

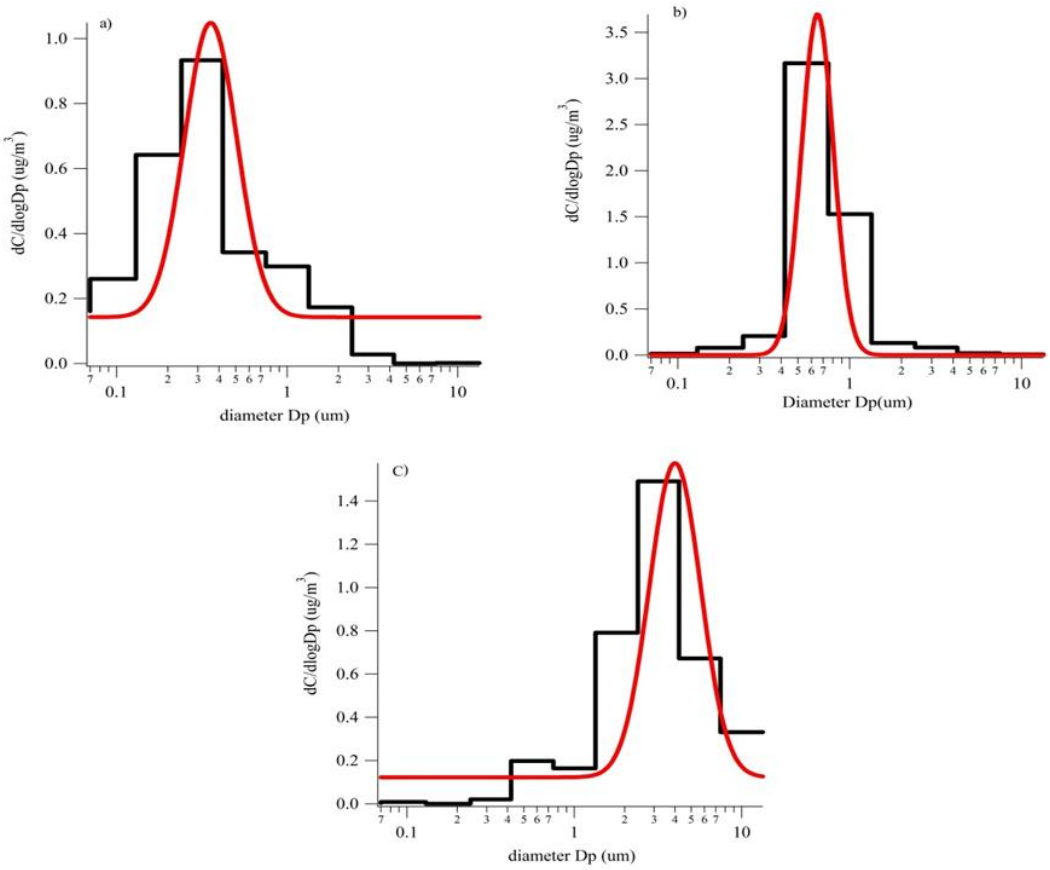

Figure 5.6 Measured PM mass size distributions illustration in TC and HKPU: a) condensation mode, b) droplet mode, and c) coarse mode; black line indicates mass on each MOUDI stage, and red line represents the fitting distribution

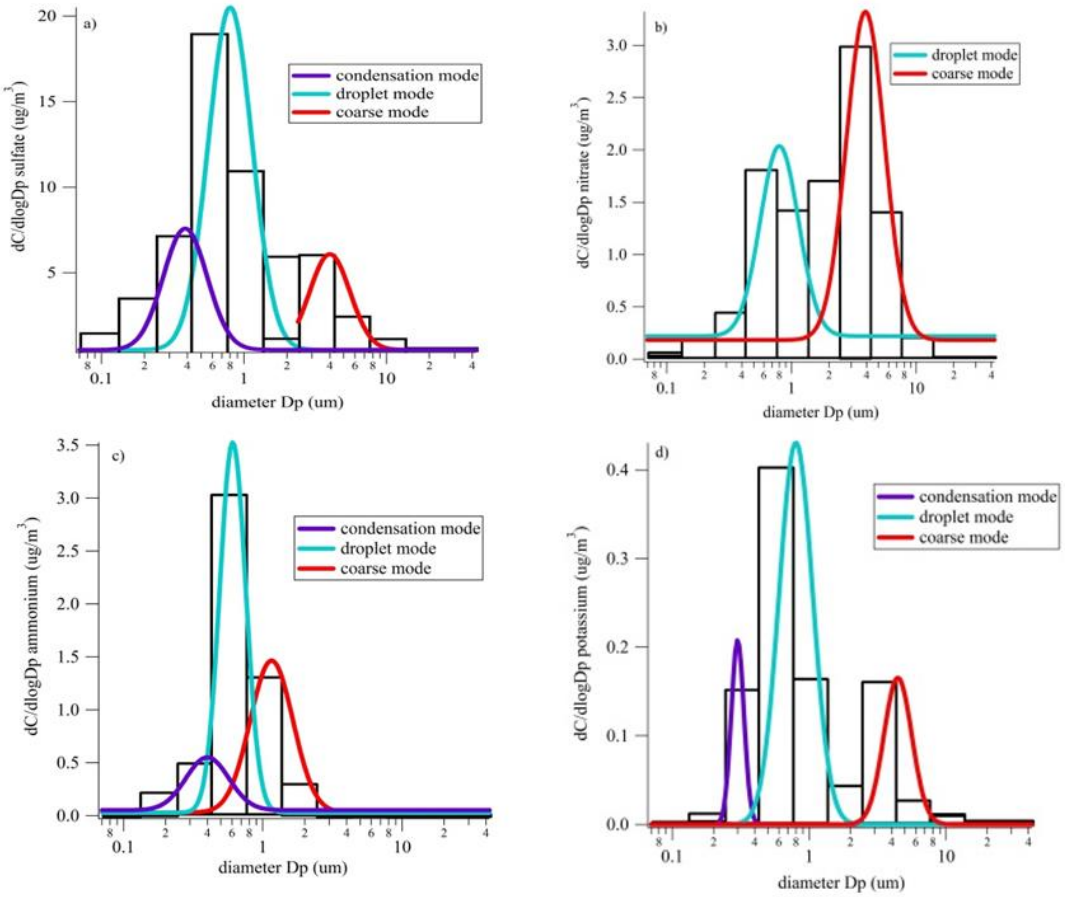
a)
dC/dlogDp sulfate (ug/m3)
condensation mode
droplet mode
coarse mode
diameter Dp (um)
b)
dC/dlogDp nitrate (ug/m3)
droplet mode
coarse mode
diameter Dp (um)
c)
dC/dlogDp ammonium (ug/m3)
condensation mode
droplet mode
coarse mode
diameter Dp (um)
d)
dC/dlogDp potassium (ug/m3)
condensation mode
droplet mode
coarse mode
diameter Dp (um)

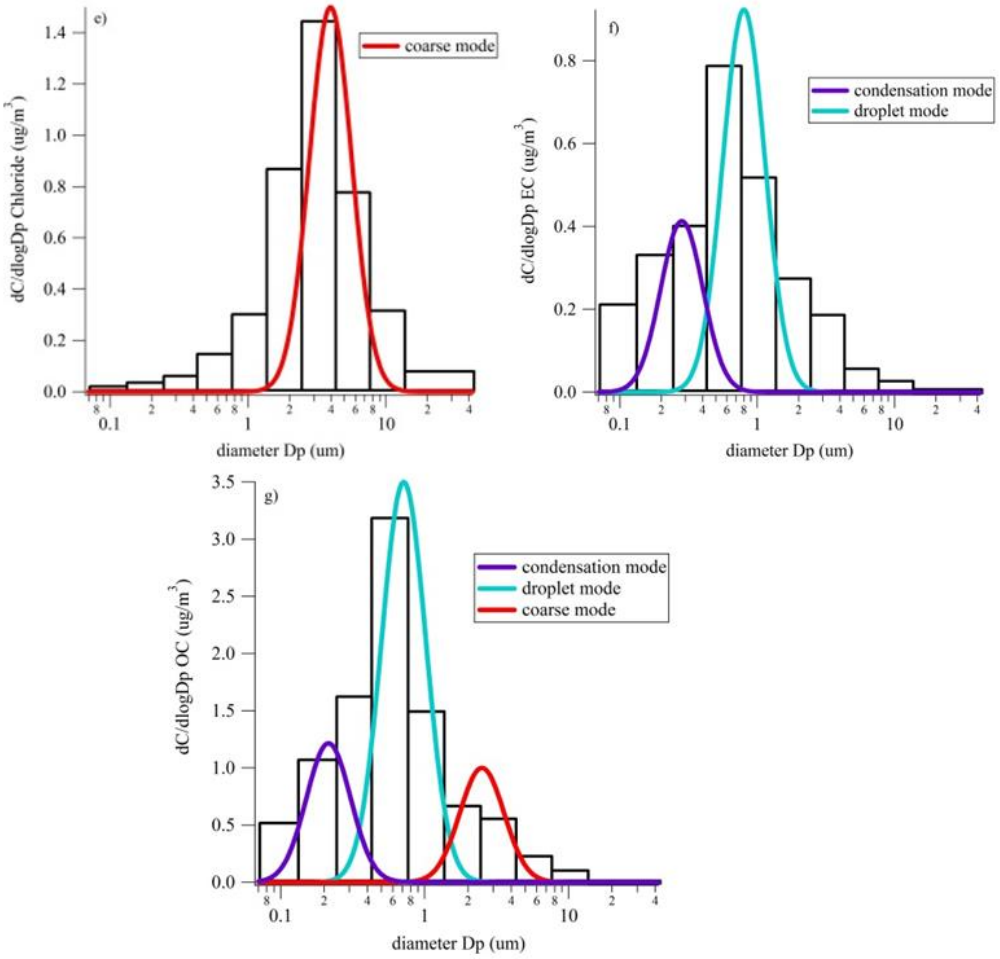

Figure 5.7 Average size distributions for: a) sulfate, b) nitrate, c) ammonium, d) water-soluble potassium, e) chloride, f) EC, and g) OC in TC and HKPU

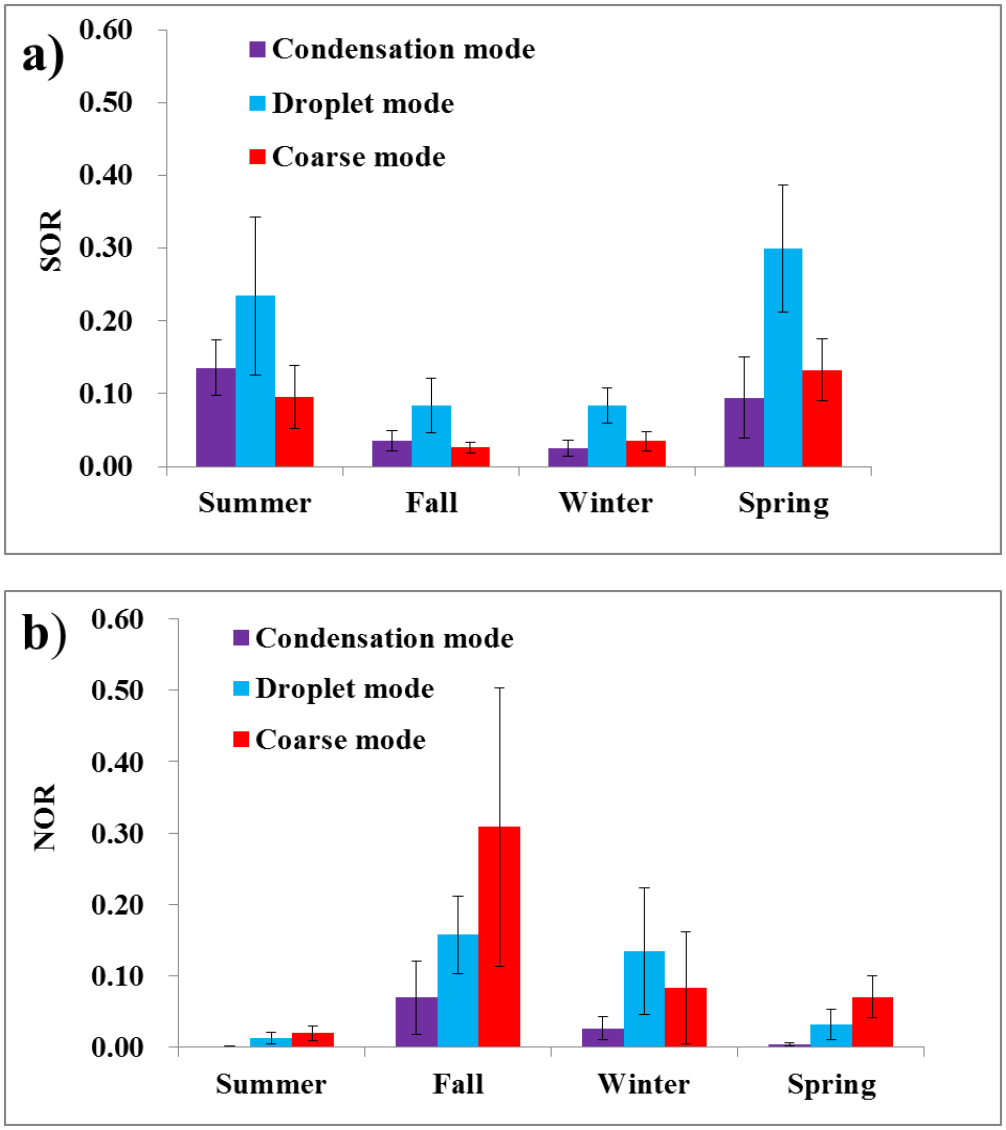

Figure 5.8 Size-fractionated: a) sulfur oxidation ratio (SOR); and b) nitrogen oxidation ratio (NOR) in four seasons in TC

Table 5.1 Seasonal PM_{10} and $PM_{1.8}$ concentrations at the TC site

Seasons (N=22)	PM_{10} $\mu g/m^3$	$PM_{1.8}$ $\mu g/m^3$	$PM_{1.8}/PM_{10}$
August/September (summer), 2011			
Clean days	23 ± 7	19 ± 8	0.83 ± 0.02
Polluted episode days	80 ± 13	62 ± 8	0.78 ± 0.04
average	47 ± 27	38 ± 20	0.81 ± 0.06
November/December (fall), 2011			
average	53 ± 17	37 ± 13	0.70 ± 0.09
February/March (winter), 2012			
average	48 ± 11	34 ± 11	0.71 ± 0.08
May (spring), 2012			
average	39 ± 11	26 ± 7	0.66 ± 0.03

Table 5.2 PM_{10} and $PM_{1.8}$ concentrations at TC and HKPU during winter period

Site	PM_{10} $\mu g/m^3$	$PM_{1.8}$ $\mu g/m^3$	$PM_{1.8}/PM_{10}$
TC			
	52.44 ± 17.11	34.51 ± 13.12	0.70 ± 0.09
HKPU			
	77.31 ± 12.34	52.11 ±10.23	0.67 ± 0.03

Table 5.3 Chemical contributions to PM_{10} and $PM_{1.8}$ at HKPU and TC, ($\mu g/m^3$)

	HKPU			TC		
	PM_{10}	$PM_{1.8}$	$PM_{1.8}/PM_{10}$	PM_{10}	$PM_{1.8}$	$PM_{1.8}/PM_{10}$
SO_4^{2-}	15.53±4.35	12.89±3.72	0.830	18.47±3.29	14.95±3.34	0.809
NH_4^+	3.41±1.07	3.22±0.83	0.944	2.75±1.43	2.68±1.39	0.973
NO_3^-	4.93±1.59	2.51±1.14	0.507	7.71±2.86	3.78±1.80	0.490
EC	4.04±0.65	3.71±0.63	0.919	1.36±0.46	1.23±0.43	0.908
POM	21.76±4.91	19.49±4.84	0.896	10.72±7.29	9.77±7.17	0.911
Sea salt	1.09±1.03	0.24±0.21	0.221	7.06±3.33	2.35±1.05	0.333
TEO	0.88±0.18	0.76±0.17	0.868	0.63±0.24	0.51±0.22	0.809
Burning-derived K^+	0.74±0.28	0.64±0.25	0.869	0.51±0.19	0.36±0.14	0.718
Soil dust	10.79±3.33	5.17±1.78	0.479	6.15±2.37	2.71±1.07	0.441

Chapter 6. Mass scattering efficiencies contributions to local visibility impairment

6.1 Introduction

Atmospheric suspended particles affect human health and contribute to global climate change by absorbing and scattering sun light (Lowenthal and Kumar, 2004). There are many approaches to estimate light scattering coefficient and to investigate the contributions on different chemical components, i.e. multi-linear regression between particle light extinction and chemical species, theoretical method to determine mass scattering/absorption efficiency (MSE/MAE) of each chemical component. MSE/MAE is a key factor related to chemical species and their particle scattering/absorption coefficient. In addition, MSE/MAE is a crucial in particle modules and chemical transport models with radiative forcing calculation (Hand and Malm, 2007).

In the past decade, there have been many studies worldwide using different methods to report MSE/MAE values of each chemical species. A large range of those values were observed in different sites around the world. The values for ammonium sulfate ranges from 2.0 to 10 m^2/g, ammonium nitrate from 1.7 to 6.2 m^2/g, particle organic matter from 0.7 to 12 m^2/g, sea salt for 0.5 to 5.2 m^2/g, soil dust from 0.5 to 3.6 m^2/g (Hand and Malm, 2007), and elemental carbon from 4-10 m^2/g in fine mode (Bond and Bergstrom, 2006). The differences may be due to differences in particle composition, morphology, size distribution and mixing state

(Watson, 2002) measured at different sites. Recently, Interagency Monitoring of Protected Visual Environments (IMPROVE) calculated MSE and MAE have been commonly used worldwide. In China, many researchers have used IMPROVE MSE/MAE to identify contribution to visibility degradation by each chemical component (i.e. ammonium sulfate, ammonium nitrate, particle organic matter, soil dust, sea salt and elemental carbon) in Guangzhou (Tao et al., 2009), Chengdu (Wang et al., 2013), Beijing (Li et al., 2013), Xi'an (Cao et al., 2012), Hong Kong (Cheung et al., 2005). However, the IMPROVE MSE/MAE were measured in U.S. low particle loading areas with less anthropogenic emission sources, as the average concentration of fine particles is 23 $\mu g/m^3$ in U.S. (U.S. IMPROVE). However, in China the concentration of fine particle is 60-180 $\mu g/m^3$, which is 3-4 times higher and the average $PM_{2.5}$ concentration in Hong Kong is around 30-50 $\mu g/m^3$, which is 1-2 times higher than particle concentration in U.S. (HKEPD). Therefore, directly applying the IMPROVE MSE/MAE values in Hong Kong or mainland China to chemical component contribution of visibility degradation investigation may cause large uncertainty. Hong Kong and the mainland China may need MSE/MAE values that differ from those of the IMPROVE chemical extinction equation. Jung et al. (2009) and Cheng et al. (2015) used both multi-linear regression method and Mie calculation to investigate MSE in Guangzhou and Shanghai (Cheng et al., 2015; Jung et al., 2009). These two studies had 1-2 months of measurement, and they do not cover the regional changes in the PRD or China.

This study, hence, has been designed to 1) evaluate the applicability of MSEs from the original IMPRVOE and the revised IMPROVE, the Guangzhou and the

Shanghai algorithms, and 2) estimates the Hong Kong specific MSEs based on four seasons of size-resolved measurements at urban and sub-urban locations.

6.2 Results and discussion

6.2.1 Difference among the four scattering algorithms

The 24-hour average chemical B_{sp} values were calculated using each of the four algorithms (Cheng et al., 2015; Jung et al., 2009; Lowenthal and Kumar, 2006; Pitchford et al., 2007); and the results are compared in Figure 6.1. All four algorithms have good correlations between measured and reconstructed value (R^2 = 0.7 – 0.8) but the slopes differ (0.97 to 1.36). The slope for the original IMPROVE algorithm (Figure 6.1a) is close to 1, but R^2 is only 0.7. The values of B_{sp} < 130 Mm^{-1} are overestimated by applying the old IMPROVE algorithm. The correlation coefficient for the revised IMPROVE algorithm is slightly higher (Figure 6.1b), but the slope is too high at 1.36. The average error [(chemical B_{sp} - measured B_{sp})/measured B_{sp}] is ~21% and 52%, respectively. Even such, the particle concentration Hong Kong exceed those in the U.S., the original IMPROVE formula provides reasonable, but not exceptional accuracy.

Jung et al., (2009) found the original IMPROVE algorithm underestimated B_{sp} and that the revised IMPROVE algorithm overestimated B_{sp} value of similar to Figure 6.1. Jung et al., (2009) used one month of data and the multi-linear regression method to estimate MSE values, which including small/large mode ammonium sulfate, ammonium nitrate and particle organic matter. Figure 6.1c

applies the Guangzhou algorithm with the slope close to unity, but higher correlations compared to original IMPROVE and a slightly lower average error of 20%. PM loadings in Guangzhou were twice higher in Hong Kong with fine mode average of 60 $\mu g/m^3$ in Guangzhou, but compared to ~40 $\mu g/m^3$ in Hong Kong.

From Malm and Hand point of view MSE can be calculated more accurately, based on the Mie theory (Hand and Malm, 2007). Cheng et al., (2015) applied Mie theory to estimate MSEs for ammonium sulfate, ammonium nitrate, and particle organic matter. Applying these MSEs to the measurement available in this study resulted in average error of ~42%. Cheng et al., (2015) used high PM loadings (average $PM_{2.5}$ concentration over 70 $\mu g/m^3$) for their MSE estimation and their algorithm may be more suitable for more polluted environment, such as Shanghai.

6.2.2 Chemical extinction algorithm for Hong Kong

Hong Kong MSE values were calculated for clean (less than 30^{th} percentile PM mass) and polluted (PM greater than 30^{th} percentile) circumstances, using equation 2.7. From the Table 6.1 specify the measurement used while Table 6.2 defines the other parameters (refractive index, density and geometric standard deviation (σ) on ammonium sulfate, ammonium nitrate, particle organic matters, soil dust and sea salt) for MSEs calculation. The geometric standard deviation (σ) of particle size distribution is a key assumption that affects the MSEs for each particle diameter. These σ were determined from the PMF fits to the MOUDI data for clean and polluted circumstance (Gao et al., 2015). Figure 6.2 illustrated MSEs change with particle diameter for the 5 chemical components, under two circumstances. Sea salt

and soil dust MSEs do not differ for clean and polluted air masses (Figure 6.2). Ammonium sulfate and organic matter MSEs show the largest variability between clean and polluted samples. Table 6.3 summarizes the MSEs for 5 components. No size distribution pattern was identified for coarse mass, so the IMPROVE MSE value (0.6) was assumed in calculating chemical B_{sp}. The average error for chemical and measured B_{sp} is around 7%, a large improvement over the other algorithms. As seem in Figure 6.3, chemical and measured B_{sp} are highly correlated (R^2=0.91) and the slope is close to unity.

6.2.3 Case study of particle light extinction and direct radiative forcing in a Hong Kong rural site (HT)

By using size-fractionated MSE with different species, size distribution on B_{ext} was shown in Figure 6.4. The single mode particle B_{ext} distribution with a peak in the droplet mode (0.56-1.8 μm) was observed, indicating that particles with size of 0.56-1.8 μm are the main contributor to visibility impairment. As shown in Table 6.4, the droplet mode accounted for 74% of the total particle B_{ext}, further confirming the importance of small particles (0.56 – 1.0 μm) in visibility degradation (Table 6.4).

Table 6.4 summarized the contribution from chemical species under four size modes, the nucleation mode (<0.1 μm), condensation mode (0.1-0.56 μm), droplet mode (0.56-1.8 μm) and coarse mode (1.8-10 μm). Soil dust contributes the most in the coarse mode and that contributions from EC are low and predominately in the condensation mode. Organic matter was the largest contributor to B_{ext} in the

droplet mode (~43%) and condensation mode (~8%). Ammonium sulfate was the second largest contributor, at around 20% in droplet mode, which suggesting the influence of local traffic and regional pollution.

And also the simulated algorithm was used for Hong Kong rural site particle light extinction calculation. Average HT chemical extinction at HT is 121.3 Mm^{-1}, when the Table 6.3 MSEs are applied for the $(NH_4)_2SO_4$, POM, and BC were the main contributors with ~58%, 19% and 13%, respectively (Figure 6.5) on an announced basis. Figure 6.6 shows the seasonal variability of the chemical contributions. B_{ext} derived from fall to summer: B_{ext} (Fall: 167.4 ± 47 Mm^{-1}) > B_{ext} (Winter: 132.3 ± 28 Mm^{-1}) > B_{ext} (Spring: 77.7 ± 26 Mm^{-1}) > B_{ext} (Summer: 77.8 ± 22 Mm^{-1}). $(NH_4)_2SO_4$ was the highest contributor, constituting ~62.58%, 56.47%, 52.14% and 50.13% of particle B_{ext} in fall, winter, spring and summer, respectively. Most of the PM at HT is transported from the PRD region, and it is minimally affected by local emissions. The $(NH_4)_2SO_4$ MSE is higher compared with MSEs for the other chemical species. Although, the BC average of 1.71 $\mu g/m^3$, is much lower than the $(NH_4)_2SO_4$ average of 10.11 $\mu g/m^3$ and the OM average of 5.44 $\mu g/m^3$, is high MAE of BC (10 m^2/g), gives it more weighted in chemical extinction formula with a ~8% to 16% contribution. The seasonal changes in the BC contribution were winter (18.7%) > summer (16.4%) > spring (16.3%) > fall (10.2%). Particle organic matter also has a MSE giving it an average contribution of ~19%. During spring, the soil dust/fugitive dust contribution increased to ~12% from ~2%, owing to an influx of Asian dust from the Chinese deserts.

Direct radiative forcing (DRF) is the net effect of pollutants on the Earth's radiation balance (Solomon, 2007). Satellite data and global chemical transport

models are often used to determine DRF in all-sky, clear-sky and polluted sky conditions. PM contributions to DRF are estimated at HT from equation 6.1 (Bond and Bergstrom, 2006; Bond et al., 2013; Chylek and Wong, 1995; Jeong et al., 2013; Park et al., 2011):

$$DRF = \frac{S_o}{4} T_{atm}^2 (1 - N)\left[4\alpha\tau_{ap} - 2(1-\alpha)^2\beta\tau_{sp}\right] \quad (6.1)$$

Where S_o is the solar irradiation flux (1370 W/m^2), T_{atm} is the transmittance of the atmosphere (0.79), N is the cloud fraction (0.6, which is from the NASA/GSFC/DISC MODIS visualization and Analysis (MOVAS) website), α is the surface albedo (rural area (HT) = 0.18), β is the particle size dependent fraction of radiation scattered by the aerosol (0.17). τ_{ap} and τ_{sp} was absorption and scattering optical thicknesses, respectively. Equations (2.2, and 2.3) define τ_{ap} and τ_{sp} (Park et al., 2011):

$$\tau_{ap} = B_{ap} \times H \times f_m \quad (6.2)$$

$$\tau_{sp} = B_{sp} \times H \quad (6.3)$$

Where H is the effective height and f_m is the mixing state. In this study, the values of H and f_m values are assumed to be 1500 m and 1.2, respectively, based on the studies of Yang et al., (2013) and Jeong et al., (2013).

As seen in Figure 6.6 at HT ranged from -6.1 W/m^2 to 1.6 W/m^2, with an average value of -1.2 W/m^2 (Figure 6.7), The global particle all-sky DRF is -1.9 W/m^2 and clear-sky DRF is 4.1 W/m^2 (Bellouin et al., 2005). Only BC absorbs incoming solar

radiation and causes positive effect on DRF. Particle DRF in Hong Kong is higher than the global clear-sky DRF, due to higher BC light absorption effect. Heald et al., (2014) found a DRF for BC of 0.06 W/m^2 for clear sky. The positive contribution from BC in Hong Kong is 3-10 times higher than the global effect (Zhuang et al., 2013), indicating a regional "brown cloud" from an atmospheric chemistry model. Mainland China had average values of -0.78 to -0.61 W/m^2, also higher than the average global value, indicating a large area covered by the Chinese brown cloud.

6.3 Summary

Particles are the key factors affecting visibility degradation; and their contribution to visibility degradation can be estimated by known mass scattering/absorption efficiency and particle concentration. The IMPROVE algorithms have been commonly used in determining MSE values in different countries. Researchers in Guangzhou and Shanghai have calculated MSE in the two cities, but all of those formulas did not have good correlation between measured and reconstructed particle scattering coefficients, which could not well represent the Hong Kong situation. Around 20% of bias were identified by applying the previous IMPROVE and Guangzhou algorithms especially in low particle loading situation, and around 40-50% of bias were observed by applying revised IMPROVE and Shanghai algorithms. Therefore, based on the four season's size-resolved particles concentration in Hong Kong, MSEs were determined based on the Mie theory under clean and unclean situation. The calculated MSEs value were

2.6 and 3.2 m^2/g for ammonium sulfate under clean and unclean situation, 2.2 (clean) and 1.5 m^2/g (unclean) for ammonium nitrate, 2.1 (clean) and 4.3 m^2/g (unclean) for particle organic matters, 1.5 m^2/g for sea salt and 1.5 m^2/g for soil dust. The correlation between measured particle scattering coefficients with reconstructed B_{sp} was 0.95 with slope 0.99, which is suitable for Hong Kong case.

The simulated equation was used to identify Hong Kong rural site particle optical properties. From the size distribution on B_{ext}, Droplet mode (0.56 – 1.8 μm) particles contributed the most to particle B_{ext}, compared to other four size groups. Within this mode, organic matter had the highest contribution (~41%) to particle B_{ext}. POM and AS were the highest contributors to the condensation mode (0.1 – 0.56 μm), accounting for ~8% and 7% of B_{ext}, respectively. (~5%). The average particle light extinction (B_{ext}) is 121.3 Mm^{-1} in Hong Kong rural site (HT). AS (~58%), OM (~19%), and BC (~13%) are the main contributors to the particle light extinction in annual average. During the contribution from soil/fugitive dust is increased to 12% from 2% in the site, since elevated soil/fugitive dust were brought from continental mainland China. The relatively high annual average particle DRF of -1.2 W/m^2 was observed in Hong Kong rural site, comparable to the global average particle DRF value.

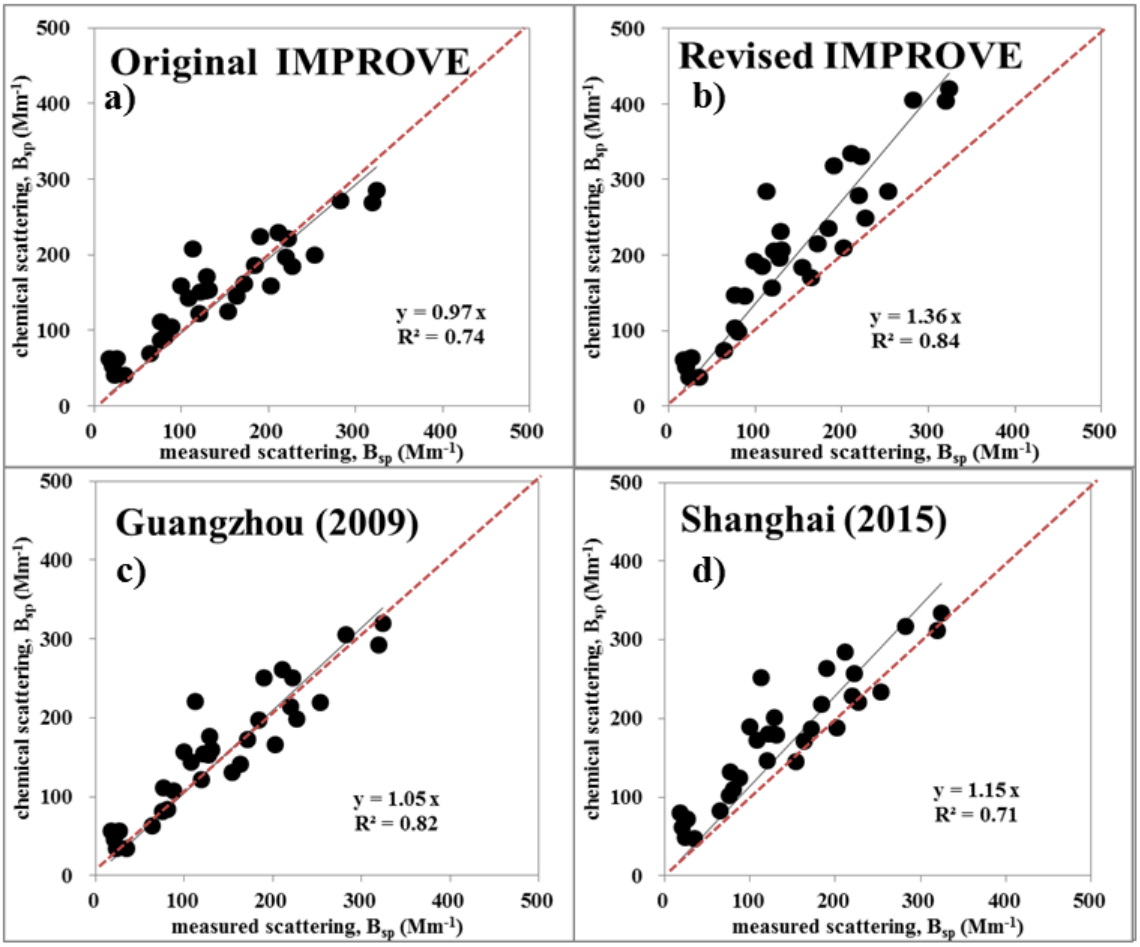

Figure 6.1 Comparison of chemical B_{sp} with measured B_{sp} from nephelometer for (a) original IMPROVE, (b) revised IMPROVE, (c) Guangzhou and (d) Shanghai chemical scattering algorithms.

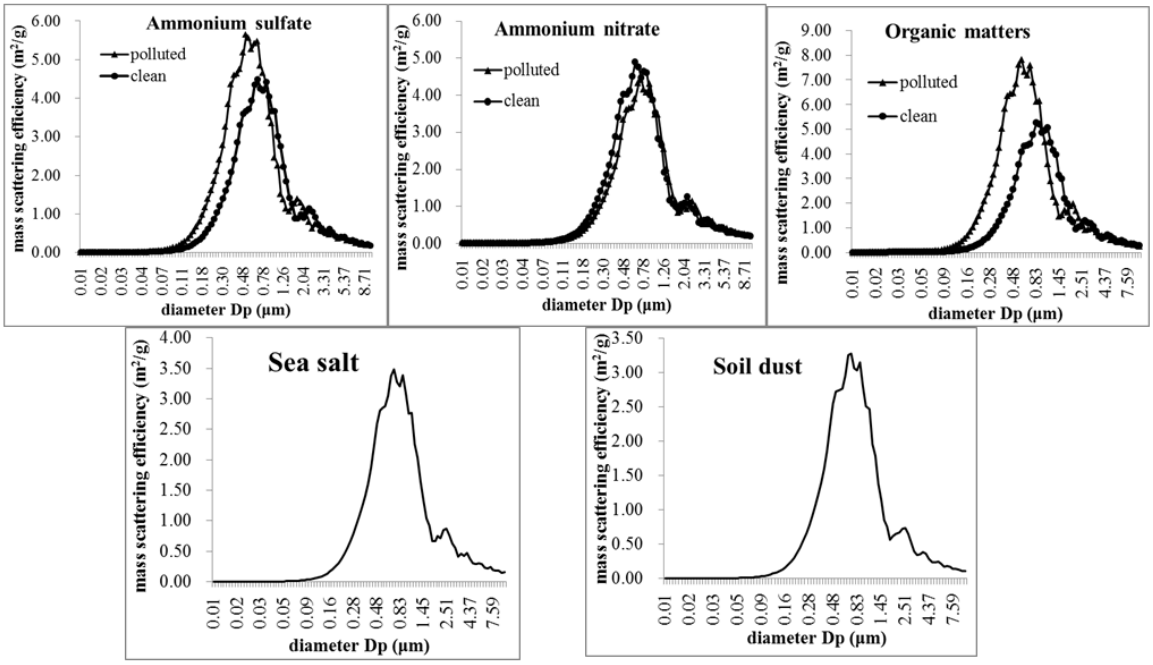

Figure 6.2 Mie-theory-based MSEs as a function of particle size of ammonium sulfate, ammonium nitrate, particle organic matter, sea salt and soil dust for clean and polluted situation in Hong Kong

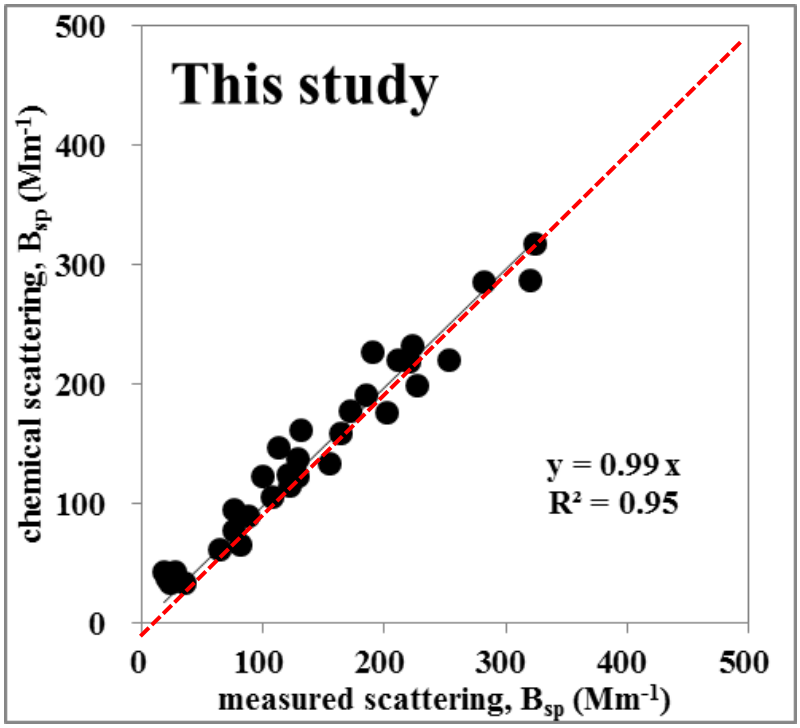

Figure 6.3 Chemical B_{sp} compared with measured B_{sp} using MSEs from Table 6.3

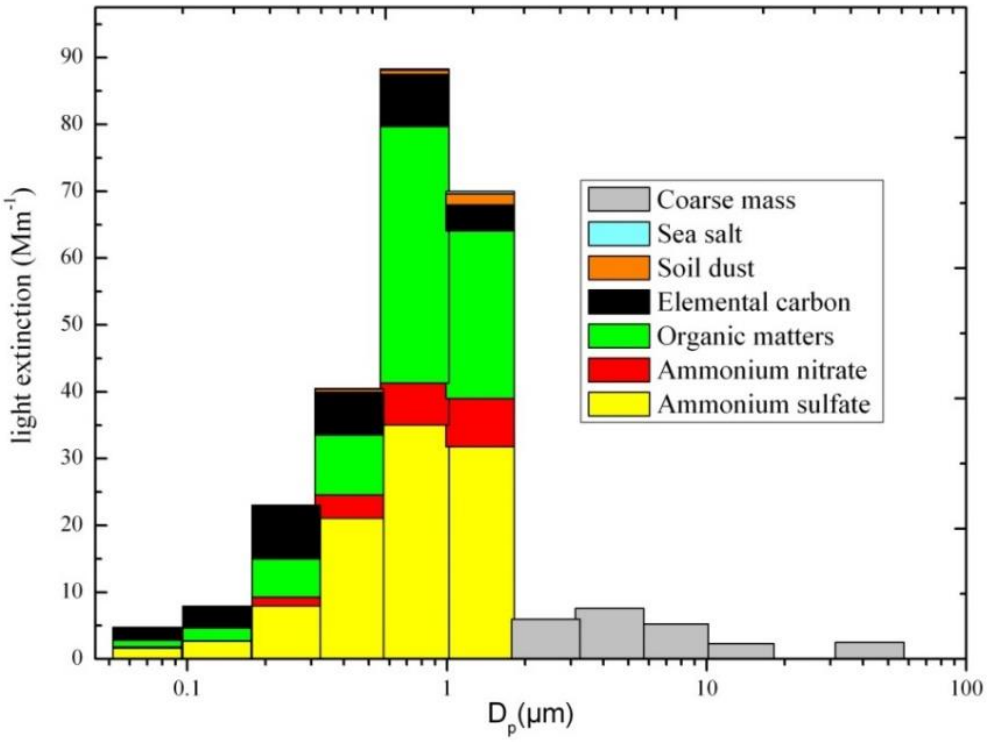

Figure 6.4 Size distribution on particle B_{ext}

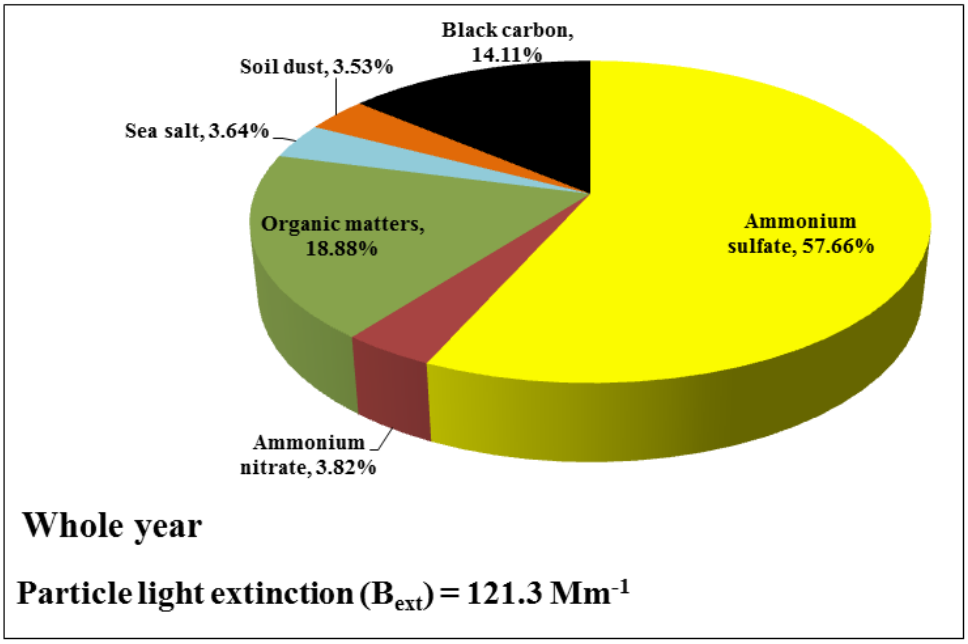

Figure 6.5 Annual average chemical contributions to HT PM light extinction

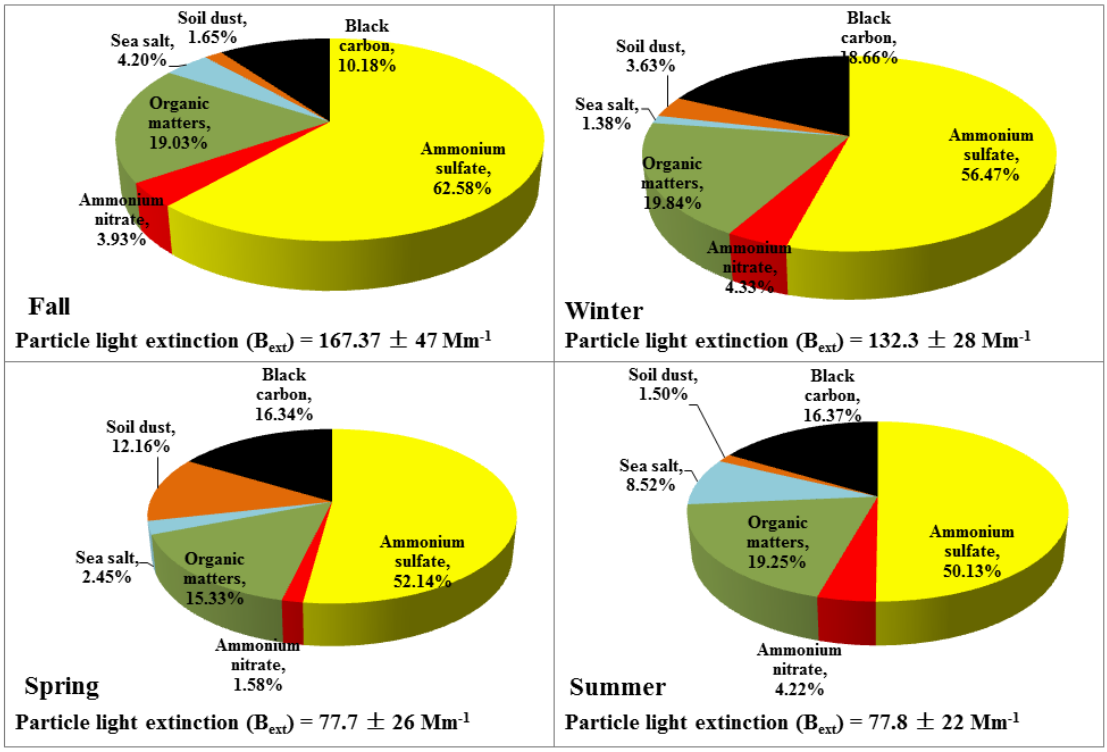

Figure 6.6 Seasonal average chemical contributions to light extinction at the HT site.

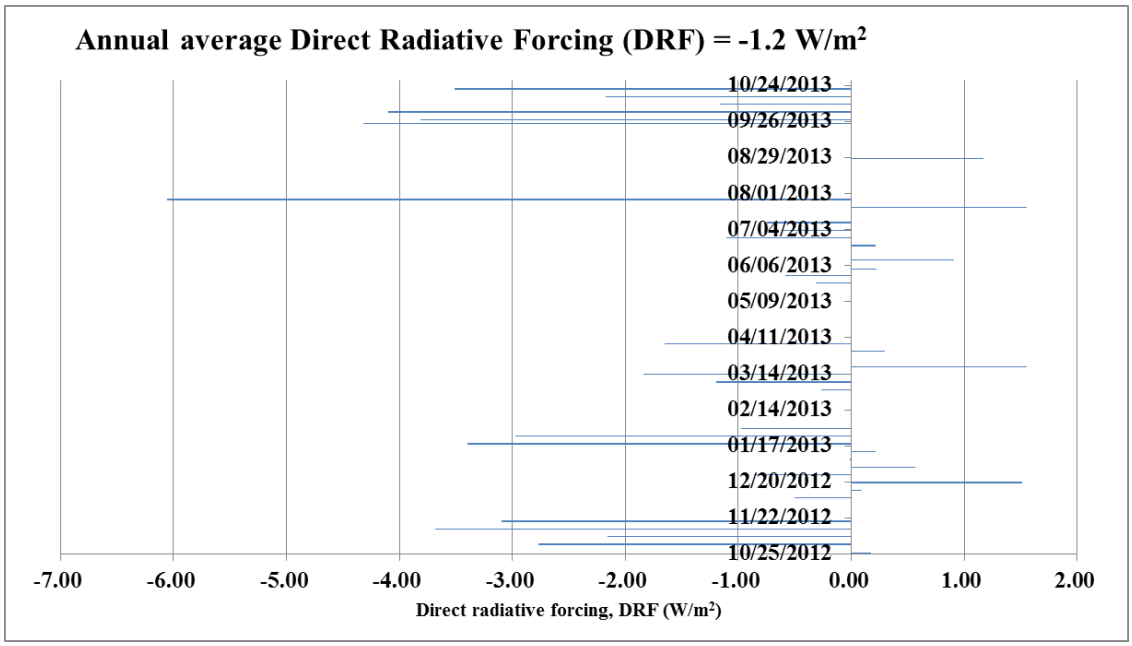

Figure 6.7 Direct radiative forcing (DRF) at the Hong Kong rural site (HT)

Table 6.1 Data used for MSE calculation and evaluation

Measurement parameters	Instrument	Average time
particle light scattering coefficient (B_{sp})	Aurora 1000 Nephelometer (EcoTech Ltd., Australia)	24 hours
PMF-fitted particle size distributions for each chemical components	MOUDI Model 100 (MSP Co., MN)	24 hours

Table 6.2 Densities, refractive indices (m) and size distribution geometric standard deviation (σ) used in the Mie theory based calculations

Chemical component	Densities (g/cm^3)	Refractive index (m)	Geometric standard deviation (σ)	
			Clean	Polluted
Ammonium sulfate	1.77	1.53, i0.0	1.6	0.7
Ammonium nitrate	1.73	1.55, i0.0	2	1.5
Particle organic matter	1.4	1.55, i0.0	3	1
Sea salt	2.16	1.54, i0.0	2	2
Soil dust	2.3	1.56, i0.005	2	2

Table 6.3 MSEs calculated based on the Mie theory under clean and polluted atmospheric conditions

Chemical component	Clean ($< 30^{th}$ percentile PM)	Polluted
Ammonium sulfate	2.64	3.21
Ammonium nitrate	2.20	1.49
Particle organic matters	2.10	4.27
Sea salt	1.49	1.49
Soil dust	1.52	1.52
Coarse mass (IMPROVE)	0.60	0.60

Table 6.4. Contribution to particle light extinction (B_{ext}) for different size-resolved chemical species

PU	Total mass	Ammonium sulfate	Ammonium nitrate	Organic matters	Elemental carbon	Soil dust	Sea salt
Coarse mode (1.8-10 μm)	4%	1%	Nil c	1%	<1%	1%	<1%
Droplet mode (0.56-1.8 μm)	74%	20%	4%	43%	2%	5%	<1%
Condensation mode (0.1-0.56 μm)	22%	7%	1.1%	8%	5%	1%	<1%
Nucleation mode (<0.1 μm)	0.4%	N.A	N.A.	N.A.	0.4%	N.A	N.A

Chapter 7. Source apportionment for airborne particles and particle light extinction in Hong Kong and China

7.1 Introduction

The main objective in air pollution study is to identify relationship between local air quality and the pollutants emission. In China, rapid economic development has greatly contributed to ambient air pollution. The Beijing-Tianjin-Hebei area, the Yangtze Delta region, and the Pearl Delta region have been considered as three most polluted areas in China. In addition, the air pollution pattern has been transitioning from primary emissions to to secondary pollution recently. The complex regional air pollution elevated the difficulties for air pollution controls in China. Quantifying emission sources in China is needed to develop cost-effective emission reduction strategies.

Source-oriented dispersion models and receptor models was used for this purpose in a previous study (Viana et al., 2008). Several source apportionments have evaluated $PM_{2.5}$ or PM_{10} source contributions in Hong Kong and the mainland China (Fung and Wong 1995; Guo et al. 2009; Lee et al. 1999). More recently, PMF has been recognized as a most useful technique for ambient atmospheric particulate matter source identification (Viana et al., 2008).

Traffic emission, secondary pollutant, residual oil combustion, fresh and aged sea salt, crustal soil coal/biomass burning have been identified in China and Hong Kong via solutions to the chemical mass balance (CMB) equations (Contini et al.

2014; Han et al. 2006; Kim et al. 2003). Size-specific source studies are limited in Hong Kong and they are well related to visibility (Tao et al., 2009; Watson, 2002).

In this chapter, the PMF solution to the CMB equation is applied to the available data to estimate source contributions to Hong Kong and B_{ext}.

7.2 Results and discussion

7.2.1 Source apportionment of size-resolved particles

Data input on size-resolved particles

PMF model was used to estimate the contributions on sources of particulate matters and particle light extinction in Hong Kong. The PMF input file contained all of the chemical species concentration and their uncertainties. Uncertainties were adjusted to account for the sampling biases and instrument precisions. Concentrations below detection limits can result in errors. When concentrations of a species were below detection limits for more than 50% of the samples, the species was excluded from analysis (Yau et al., 2013). Chemical species were categorized as "strong", "weak", and "bad" in accordance with their influence on the PMF-CMB solution (Paatero and Tapper, 1994; Watson et al., 2015).

The signal to noise ratio (S/N) is a good indicator of species' influence on the PMF factors. Species with S/N ratios > 2 were categorized as "strong", ratios between 0.2 and 2 were categorized as "weak", and S/N ratios < 0.2 were assigned to the "bad" category and were excluded from the PMF analysis. Twenty one to 22 species were included in separate input files for the condensation, droplet, coarse

modes and the total of all models. Condensation mode particles species included: NH_4^+, K^+, NO_3^-, SO_4^{2-}, OC, EC, Na, Mg, Al, Cl, Ca, V, Mn, Fe, Cu, Zn, As, Br, Cs, Ba and Pb. Droplet mode species included: NH_4^+, K^+, NO_3^-, SO_4^{2-}, OC, EC, Na, Mg, Al, Si, Cl, Ca, Ti, Mn, Fe, Cu, Zn, As, Br, Cs, Ba and Pb. Coarse mode species included: NH_4^+, K^+, NO_3^-, SO_4^{2-}, OC, EC, Na, Mg, Al, Si, Cl, Ca, Ti, Mn, Fe, Cu, Zn, Cs, Ba and Pb. The all-mode species included: NH_4^+, K^+, Cl^-, NO_3^-, SO_4^{2-}, OC, EC, Na, Al, Si, Ca, Ti, V, Mn, Fe, Cu, Zn, As, Br, Zn, Pb.

Number of sources and source profiles determination

The total of 93 (31 sets × 3 stages) filter samples were used in the size-resolved particle source apportionment analysis. Moreover, total of 279 samples (31 sets × 9 stages) were used in the particle B_{ext} source apportionment analysis.

The Q values are used to determine how well the factors and contributions reproduce the input data. Q robustness reflects a reduction of the effects of the outliers and extreme values, while Q included all values. The Q value approximately equals the degree of freedom (Polissar et al., 1998; Yau et al., 2013; Tan et al., 2014). The PMF software was run several times to determine the number of factors with source factors for the condensation, droplet, and coarse modes and particle B_{ext} numbering four, eight, three and six, respectively.

Sources factors were associated with real-word source according to the source marker prominent in each factor.

To attribute B_{ext} to source factors, a MLR was applied with B_{ext} as the dependent variable and the source factors as determined variable. The particle light extinction source apportionment cannot be initiated directly. Firstly, the source profile of suspended particles should be identified via previous steps and criteria and in the

next stage, the linear correlation between particle light extinction with suspended particle mass concentration should be investigated to find out the source profile and its contribution on particle light extinction.

7.2.2 Source factors in Hong Kong

Source apportionment on size-resolved particles in Hong Kong sub-urban area

Different source profiles have been constituted in size-resolved particles. USEPA has suggested that the better way to air quality management is to separate particle standard as $PM_{2.5}$ and PM_{coarse}, which helps people to have an in-depth understanding on the nature of particles. But particle nature and its composition of size below 2.5 μm also showed significant differences from place to place. The source apportionment in condensation, droplet and coarse mode particles was investigated in this study using the PMF model. The unique and largely constituted tracers are regarded as its corresponding sources. Table 7.1 summarizes the source profiles and the markers used to associate with real-world sources. Figure 7.1 shows the source factor/source markers identified in previous source apportionment studies (Choi et al., 2001; Han et al., 2006; Senaratne and Shooter, 2004; Yau et al., 2013).

Figure 7.2 shows the source factors that contributed to each size mode. The condensation mode consisted of 36% secondary SO_4^{2-}, 26% vehicle emissions, and 18-19% each for residual oil combustion and coal/biomass burning. The secondary sulfate factor was characterized by high loading for NH_4^+ and SO_4^{2-}. The vehicle emission factor was characterized by high loading for EC and OC. The residual oil

combustion factor was characterized high loading on Ni and V; marine engine emissions use the most residual oil in Hong Kong. Long-range transport of secondary aerosols and coal-biomass burning from the mainland China continental land affects Hong Kong air quality (Ho et al., 2006a). Vehicle emission and residual oil combustion are the typical local emission sources, whereas secondary sulfate and coal/biomass burning sources are regional source. Therefore, over 50% particles in condensation mode were from regional transport.

Eight source factors explained the droplet mode PM with the most from anthropogenic emission sources (~80%). More specifically source contributions followed the following order: secondary sulfate (24%) > industry emission (19%) > vehicle emission (14%) > secondary nitrate (13%) > incineration (6%) > coal/biomass burning (2%). About 20% of PM resulted from natural emission sources, including ~15% from sea salt and ~7% from soil dust. The coal/biomass burning and industrial emissions factor were from long-range transport, accounting for about 21%. Industrial emissions were characterized by Mn, Cs and other trace elements. The complex emission sources in this mode are combined with the most of local emission sources and few regional sources via long-range transport.

Coarse mode contributions were relatively simple. Approximately 80% of coarse mode mass was attributable to natural emission sources, sea salt and soil dust and only 20% pollutant sources are from anthropogenic emissions.

7.2.3 Source contributions to light extinction in Hong Kong

Two hundred and seventy-nine samples (31 sets × 9 stages) were used to identify and quantify particle source contributions to particle light extinction (Cao et al., 2012; Huang et al., 2006c) using the PMF model through which a total of 20 PMF base runs and 5 factors were identified (Figure 7.4). The 5 pollutant sources were determined for the particle light extinction (B_{ext}), including engine exhaust, sea salt, biomass/coal combustion, secondary formation particle and soil/fugitive dust. The detailed source factors are shown in Figure 7.3.

Factor 1 was dominated by EC and OC, markers for traffic or vehicle exhausts (Cao et al., 2012; Huang et al., 2006b), and contributed for 46% of the particle light extinction at HKPU due to the busiest cross-harbor tunnel and nearby high traffic flow. This source was the largest contributor to the B_{ext}.

Factor 2 was enriched in Na^+, Cl^- and nitrate, markers for sea salt (Huang et al., 2006b), which accounted for ~3% of the B_{ext}.

Factor 3 had high loadings of K, As, Br and Pb, typical of biomass/coal combustion (Han et al., 2006), and accounted for ~8% of particle B_{ext}. There are three coal-fired power plants in Hong Kong and many others in the PRD region.

Factor 4 was the second largest contributor to B_{ext} (~32%), abundant with NH_4^+, SO_4^{2-}, NO_3^+ and OC (Huang et al., 2006b). Prevailing northerly wind in cold season enhanced the transport of air pollutants. This factor reflected regional transport of secondary particles.

Factors 5 was associated with as soil/fugitive dust (Cheng, 2007), owing to the markers including Mn, Al, Si, Ca, Ti, Fe. High traffic volumes along with nearby construction sites contribute to ~11% of B_{ext}.

7.2.4 Comparison with source contributions in other Chinese cities

Since 2000, many source apportionment studies have been conducted via receptor model (i.e. chemical mass balance (CMB), positive matric factorization (PMF)) in many Chinese cities. The CMB model is one of the most widely used models in the world, because the model is based on a simple and clear mass conservation principle. However, the model requires the use of an explicit and integrity source inventory and source profiles that need to be kept up to date (as source profiles and inventory often evolve from time to time). . The PMF model does not need to build source databases but requires a large sample size. Therefore, the PMF model is commonly used for particle source apportionment studies in the area without clear source profiles.

Table 7.2 summarizes source contributions estimated for Chinese cities, apportionment status in Chinese major cities, Beijing, Nanjing, Shanghai, Shenzhen, Hong Kong, Wuhan, Chengdu and Xi'an, based on the recently studies (Fu et al., 2013; Ho et al., 2006a; Huang et al., 2006a; Song et al., 2006; Wang et al., 2015). $PM_{2.5}$ sources fall into six categories, fine soil/fugitive dust, coal combustion, industrial emissions, traffic emission/engine exhaust, biomass burning and secondary pollutant.

Secondary formation is the largest contributors in the seven cities, with more than 30% of $PM_{2.5}$ in each city. Large amount of gaseous precursors, i.e. SO_2, NO_x and VOCs are emitted from industrial and combustion process, Atmospheric

oxidants in these mega cities are increasing, thereby enhancing photochemical conversion of gases to particles.

Industrial emissions contributed to fine and ultra-fine PM. Large amounts of primary gaseous emissions from industry must be reduced to limit secondary aerosol formation. Because of nearby industry emission, its contribution on Beijing and Nanjing $PM_{2.5}$ pollution is up to 20%.

Engine exhaust is an important primary emission source of fine particles, $PM_{2.5}$. Traffic pollutants result from incomplete combustion in vehicle engines. In the past 20 years, the number of vehicles in China increased from 5 million to 168 million. In Shenzhen and Hong Kong, traffic emissions constitute ~15-20% of local $PM_{2.5}$. Some of the source apportionment studies conducted in Beijing do not show the importance of fresh traffic emission pollution (Zhang et.al 2013). It is the limitation of recent source model simulation. Vehicle emissions also contain gases that convert to secondary particles.

Coal consumption provides over 70% in China's energy usage. Some of the cities in China use coal for power generation; Xi'an and Wuhan have the highest contribution to $PM_{2.5}$ pollution, accounting 20% and 26%, respectively. In addition, varied energy structure makes coal consumption imbalanced distribution, which are also strongly affected by seasons. Cities in northern China use more coal than the cities in southern China. During the winter, coal-burning contributions to fine particles increase by 2 fold.

Most recently, the particle concentration in China started showing a decreasing trend. The small size particles (particle size smaller than 2.5 μm and 1 μm) problem becomes more and more prominent. In future studies, air pollution control should focus on primary gaseous, particle pollutants and atmospheric oxides reduction,

which can effectively control secondary aerosol formation problem. In addition, regional pollution problem is interaction; therefore, joint prevention and control scheme need to be launched in the whole country. The recent popular using receptor model can be further improved based on the situation of China. This survey identifies to the following needs:

1) Update the source inventory profiles in China;
2) Identify the specific sources and source area;
3) Develop and apply the source models to complement receptor model;
4) Formulate and apply a standard operating procedures for measurement and source apportionment;
5) Apply validation protocol to estimate the bias of source apportionment method, i.e. CMB solutions

7.2.5 Identification of BC Source regions in Hong Kong coastal areas

The cluster analysis technique can aid in understanding the particle emission sources under different air masses. It uses a multivariate statistics method to combine all the trajectories into one to ten representative trajectories based on the air parcel transportation. The concentration weighted trajectory (CWT) is applied to identify source regions. Each grid cell gets a weighted concentration by averaging sample values at the receptor when back trajectories pass the grid cell (Vinoj et al., 2010). The CWT analysis could improve the limitation of potential source contribution function (PSCF) method for the potential source region identification. CWT analysis has been developed more recently and the method is

more sophisticated than PSCF as it shows the spatial pattern of the potential sources of particles at the receptor site (Wang et al., 2009b). In this study, we used cluster analysis and the CWT technique to identify the potential source region that brings air pollution to the atmospheric station of HT in the cold and warm seasons. A "BC event, it is defined as BC concentration > 3 μg/m^3" and a total of 16675 hours of air masses were recorded at HT from October 2011 to September 2013 to identify BC events The cluster and CWT analysis method was applied to cold (October to March) and warm seasons (April to September). For BC concentration and its statistical parameters, along with cluster characterization for cold and warm seasons, are summarized in Table 7.3.

Figure 7.5 shows pollution clusters trajectories and identified potential source regions for the cold season. Four pollution clusters were determined (Figure 7.5a). As shown in Table 7.3, average BC concentrations for the four clusters were ~10% to 60% higher than the annual average BC concentration in the cold season. Around 45% of polluted air masses were associated with cluster #4, followed by cluster #3 (26%). Cluster #4 passed over North Vietnam and South China while Cluster #3 passed over South-east China (Cao et al., 2007). Clusters #3 and #4 originated from regions with many industrial activities. Cluster #4 from northern Vietnam (Hanoi), is a highly polluted area with a daily PM_{10} concentration up to 500 μg/m^3 (Saksena et al., 2008). Cluster #2 passed over South-west China. Elevated BC concentrations were due to pollutant transport from South China (~46%), and then from the Southeast (~26%), Northwest (~20%) and Northeast (~9%) of China.

According to the results of the CWT analysis, potential sources regions were identified as having an important contribution to BC at HT. Regions in white and dark colour indicate weak and strong potential BC source regions, respectively.

Three major potential source regions were identified for the cold season (Figure 7.5b), which were mainly located in South and South-east China, especially, Guangdong, Guangxi, Hunan and Fujian provinces.

The average trajectory clusters formed during the warm season showed different patterns. A total of three polluted clusters were formed for the warm season (Figure 7.6a), which are cluster #5 from the South China Sea, cluster #6 from the East China sea and cluster #7 passing over North China. The average BC concentration for these three clusters was 1.2 μg/m^3, which is 20% lower than the annual average BC concentration (Table 7.3). Ship emissions can enhance BC concentration during warm seasons based on cluster #5 (~31%) and #6 (~7%). A higher average value of BC concentrations in cluster #7 was observed, at 2.2 μg/m^3, which is due to the air mass was passing through highly polluted areas of northern and central China. Therefore, the BC pollution during the warm season at HT was related to transport from North China (~62%) and emissions from ships (~38%). Based on the CWT, the potential source regions were identified to are northern and central China, i.e. the Anhui, Hunan, Jiangxi and Guangdong provinces (Figure 7.6b).

Potential source areas for HT BC concentrations were dominated by mainland China. In China, BC emission stem from industrial, commercial and/or residential fuel combustion. In addition, central and south east China, namely the Hunan, Guangdong, Guangxi, Jiangxi, Anhui and Fujian provinces have contribution from industrial and residential coal combustion (Wang et al., 2012). Hunan was among the top five BC emitting provinces in China, where approximately 90% of BC emission come from industrial and residential sectors in the Hunan province (Cao et al., 2006).

7.3 Summary

This section has reported above application on PMF receptor model for size-resolved particle source identification and the source profile of particle light extinction in Hong Kong. In addition, the source apportionment via PMF model was reviewed in many Chinese major cities. Most of the sources (8 sources) were determined in droplet mode; comparative source profiles were identified in coarse (3 sources) and condensation mode (4 sources). Sea salt and soil dust constituted over 80% of PM coarse mass. The greatest contribution from anthropogenic sources was resolved in droplet mode, e.g. Secondary SO_4^{2-} and industrial emission accounted for 24% and 19% of droplet mode particle mass concentrations, respectively, with 13-15% each from vehicle emission, secondary NO_3^- and sea salt. Other sources contributed to 10% of the droplet mode particle mass concentrations. Four sources were found in the condensation modes, with 37% secondary SO_4^{2-}, 27% vehicle emissions, and 18-19% each on residual oil combustion and coal/biomass burning.

The largest contributor to particle light extinction is traffic/engine exhaust accounting ~46% of B_{ext}, followed by secondary sulfate formation particle (~32%), soil dust/fugitive dust (~11%), biomass/coal burning (~8%), and sea salt (~3%).

The source apportionment studies in China were investigated by many models, i.e. diffusion model and receptor model (CMB and PMF). Due to limited database, the most popular model for source investigation is PMF. We chose 7 cities for the source apportionment studies located in Northern, eastern, southern, western, and central China. Based on the PMF model result, 6 sources for $PM_{2.5}$ in China are commonly observed, which are fine soil/fugitive dust, coal combustion, industrial

emission, vehicle emission, biomass burning and secondary aerosol. In these cities, the most $PM_{2.5}$ contributor is secondary formation aerosol, accounting over 30% of the total $PM_{2.5}$ mass. While, in recent research stage, many issues related with $PM_{2.5}$ is still unclear, and $PM_{2.5}$ characteristics in several cities and areas need to have further discussion. The accuracy and uncertainty of source apportionment model in China need to further develop and updated. Multi-model combination may become a useful tool for pollutant source apportionment in China. This is the key and first step in China for buildup an effectiveness control method of air pollution problem.

The potential source areas have been identified of BC pollution in HT by using cluster analysis and CWT technique. In the cold season, the polluted BC was sourced from South and Southeast China, i.e. Guangdong, Guangxi, Fujian and Hunan provinces. In the warm season, sources area included the North and Central China, i.e. the Anhui, Hunan, Jiangxi and Guangdong provinces.

a)

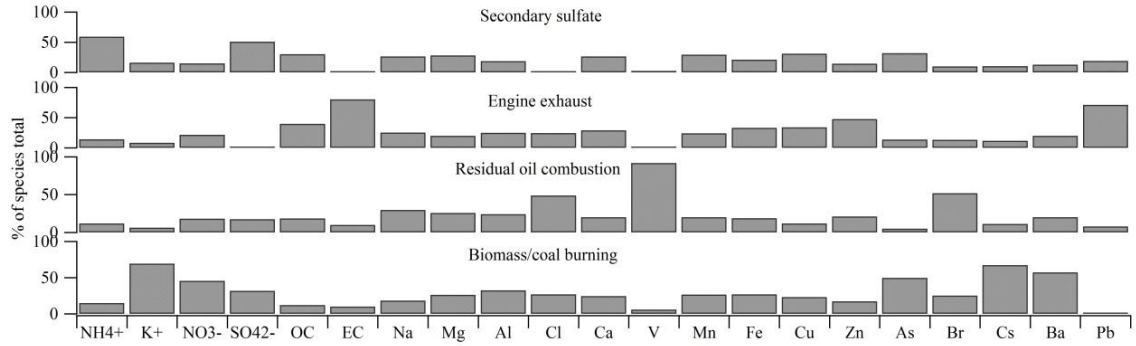
Secondary sulfate
Engine exhaust
Residual oil combustion
Biomass/coal burning
% of species total
100
50
0
NH4+ K+ NO3- SO42- OC EC Na Mg Al Cl Ca V Mn Fe Cu Zn As Br Cs Ba Pb

b)

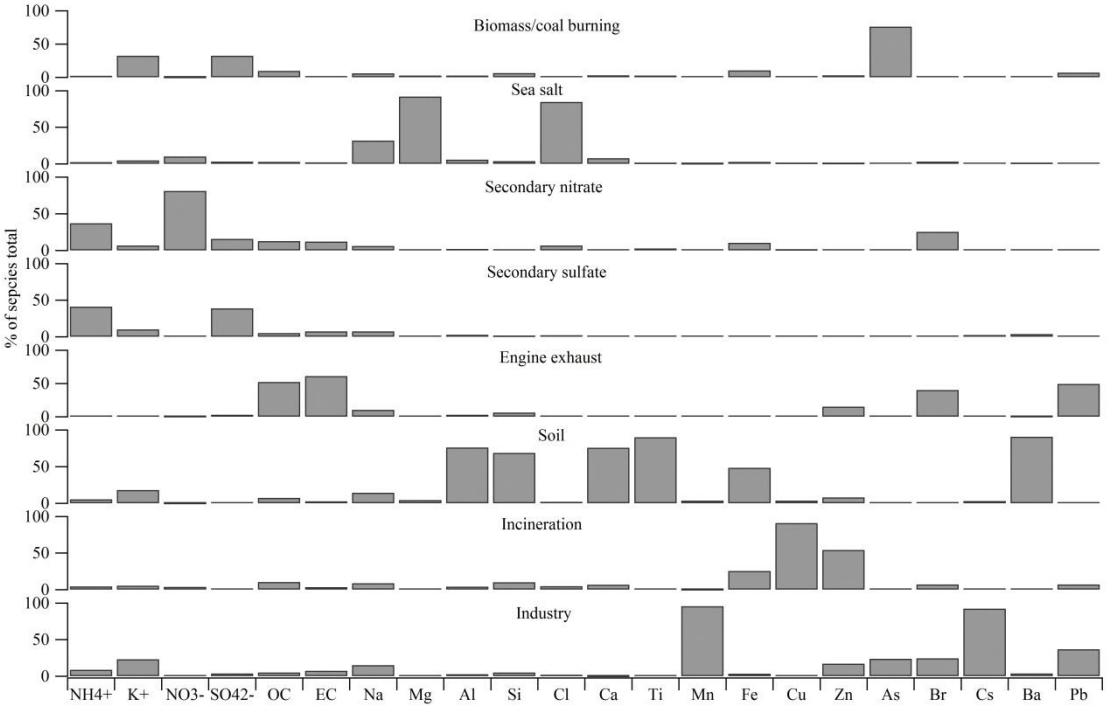
Biomass/coal burning
Sea salt
Secondary nitrate
Secondary sulfate
Engine exhaust
Soil
Incineration
Industry
% of sepcies total
100
50
0
NH4+ K+ NO3- SO42- OC EC Na Mg Al Si Cl Ca Ti Mn Fe Cu Zn As Br Cs Ba Pb

c)

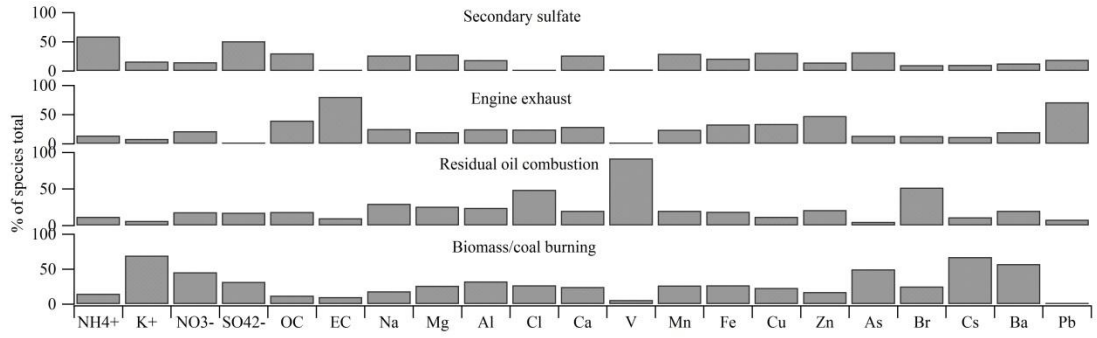

Figure 7.1 PMF-derived source factors for: a) condensation, b) droplet, and c) coarse modes;

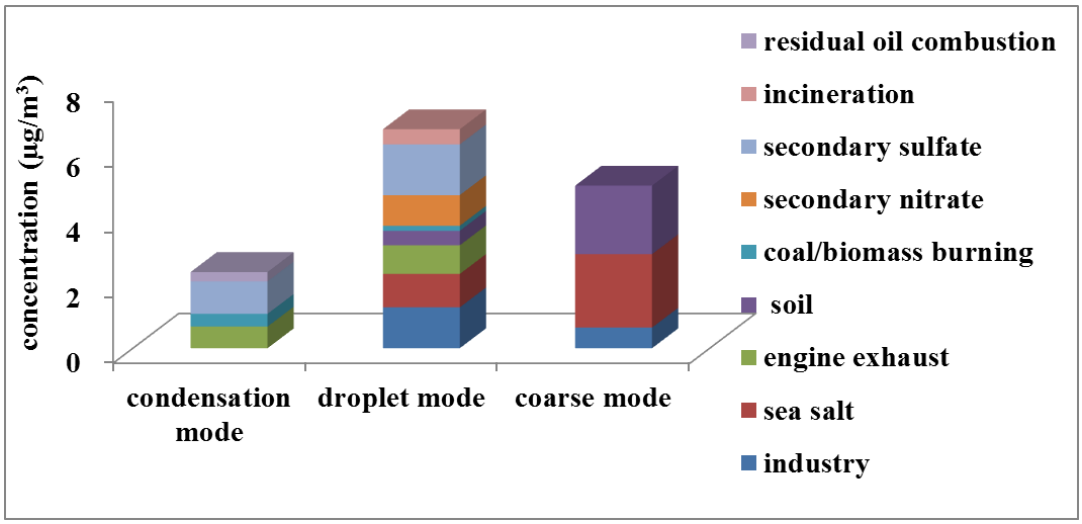

Figure 7.2 Source contributions to the condensation, droplet, and coarse modes

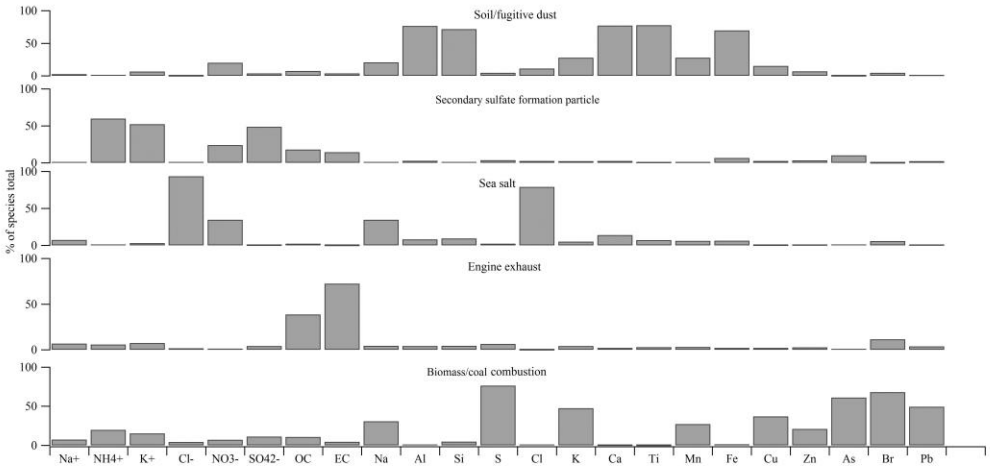

Figure 7.3 PMF-derived source factors for particle light extinction, B_{ext}

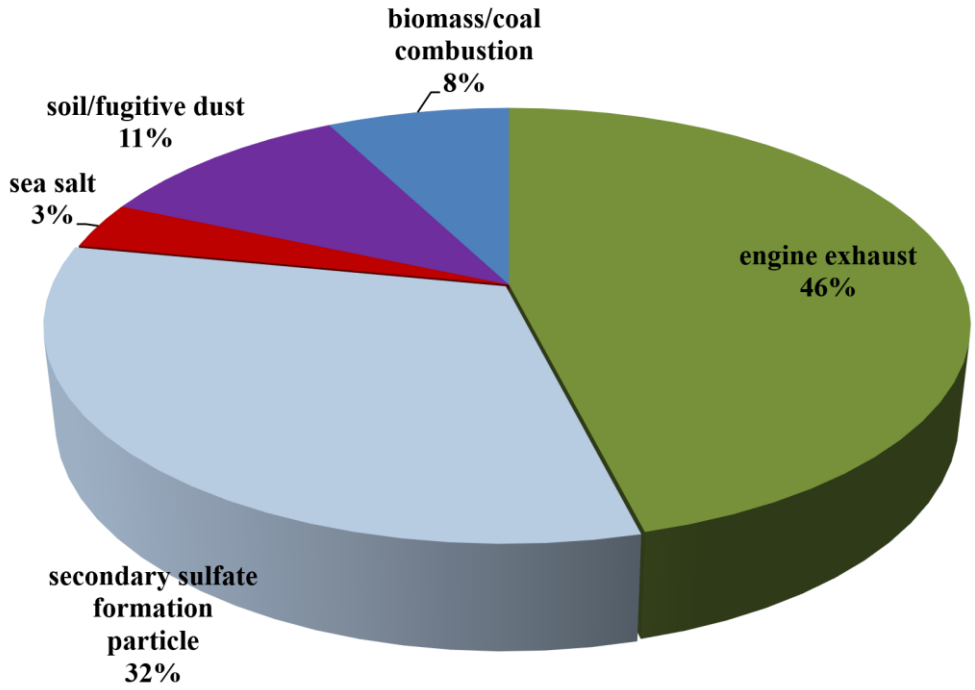

Figure 7.4 Fractional source contributions to particle B_{ext}

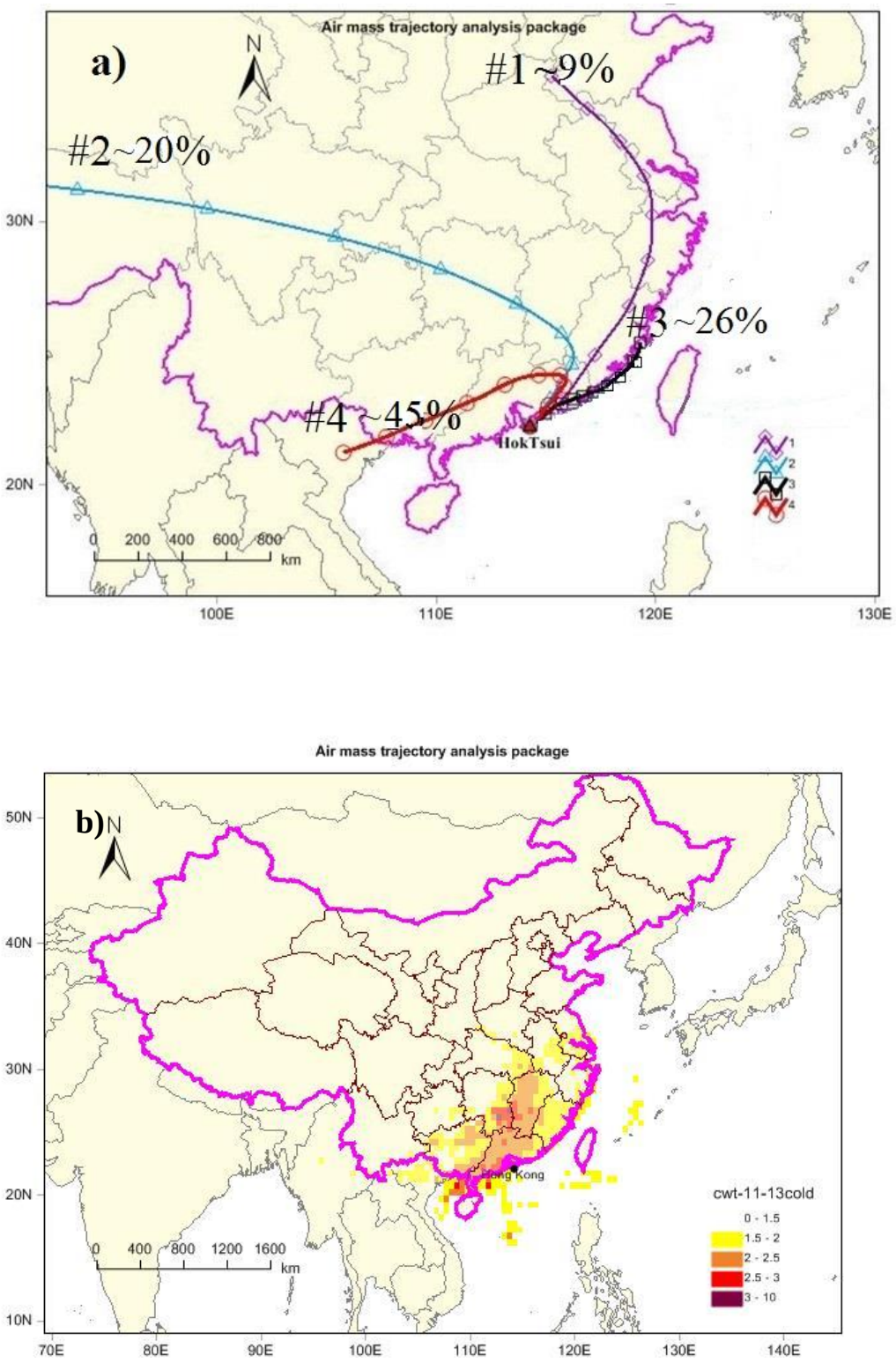

Figure 7.5 a) Cluster analysis of back trajectory for the cold season of 2011 to 2013; b) Potential source region for the cold season of 2011 to 2013

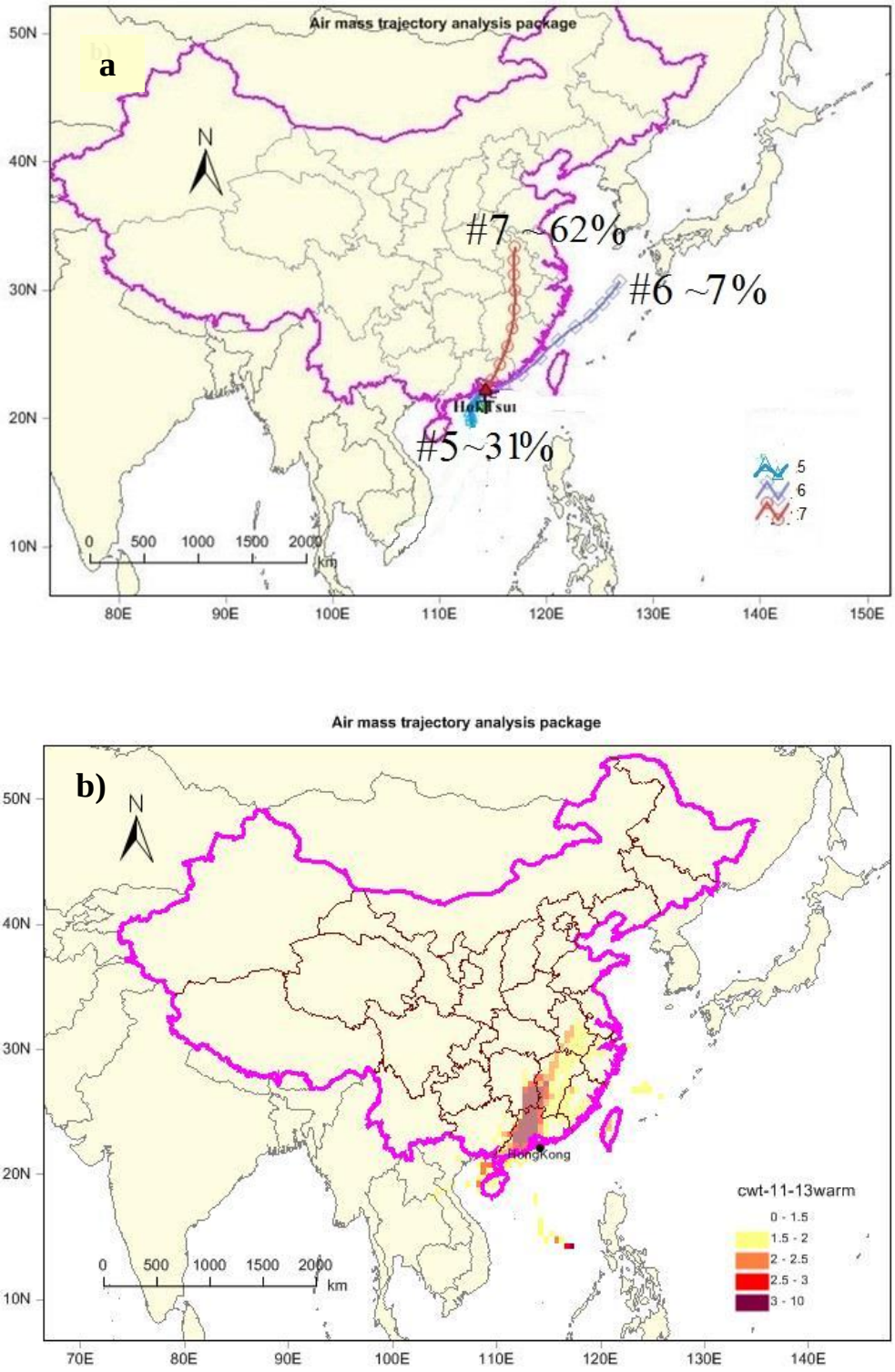

Figure 7.6 a) Cluster analysis of back trajectories for the warm season of 2011 to 2013; b) Potential source regions for the warm season of 2011 to 2013

Table 7.1 Fraction of PM source factors in each size mode

Remark: N.A.: not applicable

Sources	Source makers	Condensation mode (0.1 – 0.56 μm)	Droplet mode (0.56 – 1.8 μm)	Coarse mode (1.8 – 10 μm)
Residual oil combustion	V	21%	N.A.	N.A.
Engine exhaust/traffic emission	EC, OC	26%	14%	N.A.
Coal/Biomass burning	As, Pb, K^+	16%	2%	N.A.
Secondary sulfate	NH_4^+, SO_4^{2-}	37%	24%	N.A.
Secondary nitrate	NO_3^-, K^+	N.A.	13%	N.A.
Incineration	Cu, Zn, OC	N.A.	6%	N.A.
Industry	Mn, Cs	N.A.	19%	19%
Sea salt	Cl, Na, Mg	N.A.	15%	52%
Soil	Si, Al, Fe, Ti, Ca, Fe	N.A.	7%	29%

Table 7.2 Source contribution estimates for 7 Chinese cities

Name of cities	Source profiles
Beijing	secondary pollutant (26%) > industrial emission (25%) > coal combustion (18%) > soil dust (15%) > biomass burning (12%) > fresh traffic emission (4%)
Nanjing	secondary pollutant (35%) > industrial emission (29%) > biomass burning (12%) > coal combustion (10%) > fresh traffic emission (9%) > soil dust (5%)
Shenzhen	traffic emission (27%) > secondary sulfate (21%) > secondary organic matters (12%) > secondary nitrate (10%) > soil dust (6%) > residual oil combustion (5%) > biomass burning (5%) > sea salt (3%) > industrial emission (3%) > coal combustion (2%)
Hong Kong	secondary sulfate (23%) > sea salt (16%) > traffic emission (15%) > secondary nitrate (15%) > coal combustion (13%) > soil dust (12%) > industrial emission (5%) > residual oil combustion (1%)
Wuhan	traffic emission (27%) > coal combustion (26%) > secondary pollutants (14%) > biomass burning (12%) > soil dust (10%)
Chengdu	secondary pollutants (31%) > soil dust (19%) > coal combustion (15%) > biomass burning (10%) > traffic emission (10%) > salt (6%)
Xi’an	coal combustion (19%) > secondary sulfate (17%) > soil dust (17%) > traffic emission (15%) > secondary nitrate (12%) > industrial emission (11%) > biomass burning (9%)

Table 7.3 Characteristics of each cluster in cold and warm seasons by back trajectory clusters

Season	Cluster	Ratio on polluted air mass[a]	Mean value of BC ($\mu g/m^3$)	S.D. ($\mu g/m^3$)	Region	Characteristics
Cold season (October to March)	1	9%	1.5	0.7	North China	Developed industrial region
	2	20%	1.8	0.7	North-west China:	Populated
	3	26%	1.8	0.9	South-East China	Developed industrial region
	4	45%	2.3	1.0	South China	Motor vehicle emission
Warm season (April to September)	5	31%	1.39	1.25	South China Sea	Ships activities
	6	7%	1.15	0.57	East China Sea	Ships activities
	7	62%	2.2	1.15	North China and central China	Developed industrial region

[a] the polluted air mass ratio (polluted air mass/total air mass)

Chapter 8. Conclusions

Visual range in Hong Kong has decreased since 2000. In 2010 to 2013, this thesis work was conducted, the dominant portion of B_{ext} was particle light scattering (B_{sp}) followed by particle light absorption (B_{ap}). These components constituted over 90% of B_{ext}. This study also examined particle characteristics and their optical properties in Hong Kong.

Size-resolved aerosols and optical properties were measured at an urban, a sub-urban and a rural site in Hong Kong. The 24-hr size-resolved samples were speciated and associated with continuous particle light scattering/absorption coefficients. Particle light scattering/absorption coefficients in Hong Kong were analyzed. Chemical characteristics of size-resolved particles in Hong Kong were divided into condensation, droplet, and coarse modes. Based on the chemical characteristics and sizes of the aerosol, a chemical extinction algorithm specific to Hong Kong was derived and composed with other algorithms. Source factors, some of which could be related to real-world sources, were derived from a multivariate solution to the chemical mass balance equations.

No clear diurnal variation of B_{sp} and B_{ap} was found at the regional scale in the rural site. The dominant B_{sp} in the suburban (TC) site indicates a secondary formation process. Primary emission influences showed two traffic peaks at the urban site

(HKPU). The over 30% reduction in light absorbing BC from 2004-05 to 2011-12 at HT, suggests the effectiveness of engine exhaust controls in the PRD and Hong Kong.

Distinctive seasonal and spatial variations of PM_{10} chemical components were observed. PM_{10} concentrations were the highest in the fall and the lowest in the spring. Due to high traffic volume near HKPU, the most dominant components were POM and EC. Secondary sulfate accounted for 26-37% of PM mass. Regional transportation and stagnant meteorological conditions elevated concentration of aged and secondary pollutants in Hong Kong.

The PMF resolved mass median aerodynamic diameters (MMAD) for three particle size modes were 0.4, 0.7, and 3.8 μm for the condensation, droplet and coarse modes, respectively. Geometric standard deviations, σ, ranging from 1.32 - 1.42 were observed in Hong Kong. The droplet mode was dominated by SO_4^{2-}, NH_4^+, K^+, OC and EC. NO_3^- was mostly found in the coarse mode, due to neutralization of HNO_3 by sea salt and soil dust.

Because of specific particle size distribution and chemical composition features, around 20% to 50% biases were found using four chemical extinction algorithms, (original and revised IMPROVE, Shanghai and Guangzhou equations) when applied in Hong Kong. The MSEs for major chemical components were calculated for clean and polluted situations, and these showed better between chemical and measured B_{sp} for Hong Kong sites. The value of MSEs for Hong Kong were: 2.6 (clean) and 3.2 m^2/g (polluted) for ammonium sulfate, 2.2 (clean) and 1.5 m^2/g (polluted) for ammonium

nitrate, 2.1 (clean) and 4.3 m^2/g (polluted) for particle organic matter, 1.5 m^2/g for sea salt and 1.5 m^2/g for soil dust.

Droplet mode (0.56 – 1.8 μm) particles contributed the most to particle $B_{ext,}$ compared to other four size groups. Within this mode, POM had the highest contribution (~41%) to particle B_{ext}. POM and AS were the highest contributors to the condensation mode (0.1 – 0.56 μm), accounting for ~8% and 7% of B_{ext}, respectively.

At HT, major chemical contributors to particle extinction were: $(NH_4)_2SO_4$ (~58%), POM (~19%) and BC (~13%) as annual averages. The soil/fugitive dust contribution increased to 12% from 2% during the spring Asian dust period.

Eight source factors were found for particles in the droplet mode, three for those in the coarse mode, and four for those in the condensation mode. Over 80% of the coarse mode was contributed by sea salt and soil dust. The droplet mode particles, resulting from anthropogenic emission sources, included secondary SO_4^{2-} (24%), industrial emissions (19%), vehicle emission, secondary NO_3^- and sea salt (13-15% for each). Only 10% of the droplet mode particles resulted from other source types. Primary emissions contributed to the mode, including 27% from vehicle emissions, and 18-19% each from residual oil combustion and coal/biomass burning, and ~37% was from secondary SO_4^{2-}. Local traffic/engine emissions and secondary sulfate formation particle were the most important contributors to particle B_{ext}.

The combination of local emissions and the long-range transport affects particle B_{ext}. Transport was mainly from South and Southeast China, i.e. Guangdong, Guangxi,

Fujian and Hunan provinces during autumn and winter. Transport was from North and Central China, i.e., Anhui, Hunan, Jiangxi and Guangdong provinces during spring and summer. The Hong Kong government and mainland China governments need to make a long-term joint air pollution control policies scheme for improving Hong Kong air quality and atmospheric visibility.

Chapter 9. Significance and limitations of this study

The significant findings of this study are:

a) The study has provided the detailed discussion on Hong Kong particle optical properties.

b) Measured size distributions elucidated the relationships among particle formation mechanisms, chemical species concentrations, and atmospheric visibility.

c) The study calculated Hong Kong specific MSEs and MAEs that allow for a more accurate estimate of chemical extinction than other less specific algorithms.

d) This study, for the first time, combined size-segregated particles and particle light scattering coefficient via Mie theory to investigate local mass scattering efficiency to identify relative accurate the contribution on local visibility degradation from different chemical components. In addition, the information is also helpful for updating or improving optical related global models.

Several limitations were found in this study:

1) More chemical speciation over time period < 24 hours would better explain the diurnal evolution of B_{ext}.

2) Simultaneous measurements at all sites would better reflect spatial differences, but sufficient instrumentation was unavailable for such measurements.

3) PMF-derived source factors showed bias/uncertainty of real-world emitters.

4) Future measurements should include the treatment of brown carbon in Hong Kong, as it is an important light absorber independent from BC.

5) In recent, the continuous measurement on PM_1 is still limited, in the future study may focus more on PM_1 with optical characteristics.

References

Andreae, M.O., 1983. Soot Carbon and Excess Fine Potassium: Long-range transport of combustion-derived aerosols. Science 220, 1148-1151.

Andreae, M.O., Schmid, O., Yang, H., Chand, D., Yu, J.Z., Zeng, L.M., Zhang, Y.H., 2008. Optical properties and chemical composition of the Atmospheric Aerosol in urban Guangzhou, China. Atmospheric Environment 42, 6335-6350.

Arnott, W.P., Hamasha, K., Moosmüller, H., Sheridan, P.J., Ogren, J.A., 2005. Towards Aerosol Light-Absorption Measurements with a 7-Wavelength Aethalometer: Evaluation with a Photoacoustic Instrument and 3-Wavelength Nephelometer. Aerosol Science and Technology 39, 17-29.

Bellouin, N., Boucher, O., Haywood, J., Reddy, M.S., 2005. Global estimate of aerosol direct radiative forcing from satellite measurements. Nature 438, 1138-1141.

Bian, Q., Huang, X.H.H., Yu, J.Z., 2014. One-year observations of size distribution characteristics of major aerosol constituents at a coastal receptor site in Hong Kong – Part 1: Inorganic ions and oxalate. Atmospheric Chemistry and Physics 14, 9013-9027.

Bohren, C.F., Huffman, D.R., 2008. Absorption and Scattering of Light by Small Particles. Wiley and Sons, New York, NY.

Bond, T.C., Streets, D.G., Yarber, K.F., Nelson, S.M., Woo, J.-H., Klimont, Z., 2004. A technology-based global inventory of black and organic carbon emissions from combustion. Journal of Geophysical Research: Atmospheres 109, D14203.

Bond, T.C., Bergstrom, R.W., 2006. Light absorption by carbonaceous particles: An investigative review. Aerosol Science and Technology 40, 27-67.

Bond, T.C., Bhardwaj, E., Dong, R., Jogani, R., Jung, S., Roden, C., Streets, D.G., Trautmann, N.M., 2007. Historical emissions of black and organic carbon aerosol from energy-related combustion, 1850–2000. Global Biogeochemical Cycles 21, GB2018.

Bond, T.C., Doherty, S.J., Fahey, D.W., Forster, P.M., Berntsen, T., DeAngelo, B.J., Flanner, M.G., Ghan, S., Kärcher, B., Koch, D., Kinne, S., Kondo, Y., Quinn, P.K., Sarofim, M.C., Schultz, M.G., Schulz, M., Venkataraman, C., Zhang, H., Zhang, S., Bellouin, N., Guttikunda, S.K., Hopke, P.K., Jacobson, M.Z., Kaiser, J.W., Klimont, Z., Lohmann, U., Schwarz, J.P., Shindell, D., Storelvmo, T., Warren, S.G., Zender, C.S., 2013. Bounding the role of black carbon in the climate system: A scientific assessment. Journal of Geophysical Research: Atmospheres 118, 5380-5552.

Cao G, Zhang X, Zheng F. 2006. Inventory of black carbon and organic carbon emissions from China. Atmospheric Environment; 40: 6516-6527.

Cao, J.J., Lee, S.C., Chow, J.C., Watson, J.G., Ho, K.F., Zhang, R.J., Jin, Z.D., Shen, Z.X., Chen, G.C., Kang, Y.M., Zou, S.C., Zhang, L.Z., Qi, S.H., Dai, M.H., Cheng,

Y., Hu, K., 2007. Spatial and seasonal distributions of carbonaceous aerosols over China. Journal of Geophysical Research-Atmospheres; 112.

Cao, J.J., Wang, Q.Y., Chow, J.C., Watson, J.G., Tie, X.X., Shen, Z.X., Wang, P., An, Z.S., 2012. Impacts of aerosol compositions on visibility impairment in Xi'an, China. Atmospheric Environment 59, 559-566.

Cao, J., Chow, J.C., Lee, F.S., Watson, J.G., 2013. Evolution of PM2. 5 measurements and standards in the US and future perspectives for China. Aerosol and Air Quality Research 13, 1197-1211.

Chameides, W.L., Stelson, A.W., 1992. Aqueous-phase chemical processes in deliquescent sea-salt aerosols: A mechanism that couples the atmospheric cycles of S and sea salt. Journal of Geophysical Research: Atmospheres 97, 20565-20580.

Chang, W.L., Koo, E.H., 1986. A study of visibility trends in Hong Kong (1968–1982). Atmospheric Environment (1967) 20, 1847-1858.

Cheng, Y., 2007. The characteristics and source identification of airborne particles at the roadside of Hong Kong-PolyU (PU) supersite.

Cheng, Y., Zou, S.C., Lee, S.C., Chow, J.C., Ho, K.F., Watson, J.G., Han, Y.M., Zhang, R.J., Zhang, F., Yau, P.S., Huang, Y., Bai, Y., Wu, W.J., 2011. Characteristics and source apportionment of PM_1 emissions at a roadside station. Journal of Hazardous Materials 195, 82-91.

Cheng, Y.F., Eichler, H., Wiedensohler, A., Heintzenberg, J., Zhang, Y.H., Hu, M., Herrmann, H., Zeng, L.M., Liu, S., Gnauk, T., Brüggemann, E., He, L.Y., 2006. Mixing state of elemental carbon and non-light-absorbing aerosol components derived from in situ particle optical properties at Xinken in Pearl River Delta of China. Journal of Geophysical Research: Atmospheres 111, D20204.

Cheng, Y.F., Wiedensohler, A., Eichler, H., Su, H., Gnauk, T., Brüggemann, E., Herrmann, H., Heintzenberg, J., Slanina, J., Tuch, T., Hu, M., Zhang, Y.H., 2008. Aerosol optical properties and related chemical apportionment at Xinken in Pearl River Delta of China. Atmospheric Environment 42, 6351-6372.

Cheng, Z., Jiang, J., Chen, C., Gao, J., Wang, S., Watson, J.G., Wang, H., Deng, J., Wang, B., Zhou, M., Chow, J.C., Pitchford, M.L., Hao, J., 2015. Estimation of Aerosol Mass Scattering Efficiencies under High Mass Loading: Case Study for the Megacity of Shanghai, China. Environmental Science & Technology 49, 831-838.

Cheung, H.-C., Wang, T., Baumann, K., Guo, H., 2005. Influence of regional pollution outflow on the concentrations of fine particulate matter and visibility in the coastal area of southern China. Atmospheric Environment 39, 6463-6474.

Choi, J.C., Lee, M., Chun, Y., Kim, J., Oh, S., 2001. Chemical composition and source signature of spring aerosol in Seoul, Korea. Journal of Geophysical Research: Atmospheres 106, 18067-18074.

Chow, J.C., Watson, J.G., 1999. Ion chromatography in elemental analysis of airborne particles. Elemental analysis of airborne particles Vol. 1, Chapter: 3, Publisher: Gordon and Breach Science, Amsterdam, The Netherlands, Editors: S. Landsberger, M. Creatchman, pp.97-137.

Chow, J.C., Watson, J.G., Lowenthal, D.H., Magliano, K.L., 2005. Loss of $PM_{2.5}$ Nitrate from Filter Samples in Central California. Journal of the Air & Waste Management Association 55, 1158-1168.

Chow, J.C., Watson, J.G., Chen, L.-W.A., Chang, M.O., Robinson, N.F., Trimble, D., Kohl, S., 2007. The IMPROVE_A temperature protocol for thermal/optical carbon analysis: maintaining consistency with a long-term database. Journal of the Air & Waste Management Association 57, 1014-1023.

Chow, J.C., Watson, J.G., Lowenthal, D.H., Magliano, K.L., 2008. Size-resolved aerosol chemical concentrations at rural and urban sites in Central California, USA. Atmospheric Research 90, 243-252.

Chow, J.C., Watson, J.G., Chen, L.W.A., Rice, J., Frank, N.H., 2010a. Quantification of $PM_{2.5}$ organic carbon sampling artifacts in US networks. Atmospheric Chemistry and Physics 10, 5223-5239.

Chow, J.C., Watson, J.G., Kohl, S., Chen, L.-W.A., Chai, W., 2010b. Measurements and validation for the 2008/2009 particulate matter study in Hong Kong. Reno, USA: Desert Research Institute. NV.

Chow, J., Watson, J., Robles, J., Wang, X., Chen, L.W.A., Trimble, D., Kohl, S., Tropp, R., Fung, K., 2011. Quality assurance and quality control for thermal/optical analysis of aerosol samples for organic and elemental carbon. Analytical and Bioanalytical Chemistry 401, 3141-3152.

Chow, J., Lowenthal, D., Chen, L.W.A., Wang, X., Watson, J., 2015. Mass reconstruction methods for $PM_{2.5}$: a review. Air Quality, Atmosphere & Health 8, 243-263.

Chylek, P., Wong, J., 1995. Effect of absorbing aerosols on global radiation budget. Geophysical Research Letters 22, 929-931.

Clegg, S.L., Brimblecombe, P., Wexler, A.S., 1998. Thermodynamic Model of the System H^+−NH_4^+−SO_4^{2-}−NO_3^-−H_2O at Tropospheric Temperatures. The Journal of Physical Chemistry A 102, 2137-2154.

Clegg, S.L., Seinfeld, J.H., 2004. Improvement of the Zdanovskii−Stokes−Robinson Model for Mixtures Containing Solutes of Different Charge Types. The Journal of Physical Chemistry A 108, 1008-1017.

Contini, D., Cesari, D., Genga, A., Siciliano, M., Ielpo, P., Guascito, M.R., Conte, M., 2014. Source apportionment of size-segregated atmospheric particles based on the major water-soluble components in Lecce (Italy). Science of the Total Environment 472, 248-261.

Crilley, L.R., Bloss, W.J., Yin, J., Beddows, D.C.S., Harrison, R.M., Allan, J.D., Young, D.E., Flynn, M., Williams, P., Zotter, P., Prevot, A.S.H., Heal, M.R., Barlow, J.F., Halios, C.H., Lee, J.D., Szidat, S., Mohr, C., 2015. Sources and contributions of wood smoke during winter in London: assessing local and regional influences. Atmospheric Chemistry and Physics 15, 3149-3171.

De Haan, D., Finlayson-Pitts, B., 1997. Knudsen cell studies of the reaction of gaseous nitric acid with synthetic sea salt at 298 K. The Journal of Physical Chemistry A 101, 9993-9999.

Deng, X.J., Tie, X.X., Wu, D., Zhou, X.J., Bi, X.Y., Tan, H.B., Li, F., Hang, C.L., 2008. Long-term trend of visibility and its characterizations in the Pearl River Delta (PRD) region, China. Atmospheric Environment 42, 1424-1435.

Dubovik, O., Holben, B., Eck, T.F., Smirnov, A., Kaufman, Y.J., King, M.D., Tanre, D., Slutsker, I., 2002. Variability of absorption and optical properties of key aerosol types observed in worldwide locations. Journal of Atmospheric Science 59, 590-608.

Dumka, U.C., Manchanda, R.K., Sinha, P.R., Sreenivasan, S., Moorthy, K.K., Suresh Babu, S., 2013. Temporal variability and radiative impact of black carbon aerosol over tropical urban station Hyderabad. Journal of Atmospheric and Solar-Terrestrial Physics 105–106, 81-90.

Dzubay, T.G., Hasan, H., 1990. Fitting Multimodal Lognormal Size Distributions to Cascade Impactor Data. Aerosol Science and Technology 13, 144-150.

Esteve, A.R., Estellés, V., Utrillas, M.P., Martínez-Lozano, J.A., 2012. In-situ integrating nephelometer measurements of the scattering properties of atmospheric aerosols at an urban coastal site in western Mediterranean. Atmospheric Environment 47, 43-50.

Finlayson-Pitts, B.J., Pitts Jr, J.N., 1999. Chemistry of the upper and lower atmosphere: theory, experiments, and applications. Academic Press.

Flagan, Richard C. and Seinfeld, John H. (1988) Fundamentals of air pollution engineering. Prentice-Hall, Inc. , Englewood Cliffs, New Jersey.

Flesch, J.P., Norris, C.H., Nugent, A.E., 1967. Calibrating Particulate Air Samplers with Monodisperse Aerosols.: Application to the Andersen Cascade Impactor. American Industrial Hygiene Association Journal 28, 507-516.

Fu, X., Wang, S., Zhao, B., Xing, J., Cheng, Z., Liu, H., Hao, J., 2013. Emission inventory of primary pollutants and chemical speciation in 2010 for the Yangtze River Delta region, China. Atmospheric Environment 70, 39-50.

Fujitani, Y., Hasegawa, S., Fushimi, A., Kondo, Y., Tanabe, K., Kobayashi, S., Kobayashi, T., 2006. Collection characteristics of low-pressure impactors with various impaction substrate materials. Atmospheric Environment 40, 3221-3229.

Fung, Y.S., Wong, L.W.Y., 1995. Apportionment of air pollution sources by receptor models in Hong Kong. Atmospheric Environment 29, 2041-2048.

Gao, Y., Lai, S., Lee, S.-C., Yau, P.S., Huang, Y., Cheng, Y., Wang, T., Xu, Z., Yuan, C., Zhang, Y., 2015. Optical properties of size-resolved particles at a Hong Kong urban site during winter. Atmospheric Research 155, 1-12.

Gao Y, Lee S-C, Huang Y, Chow JC, Watson JG., 2016. Chemical characterization and source apportionment of size-resolved particles in Hong Kong sub-urban area. Atmospheric Research; 170: 112-122.

Garcia, L.Q., Castro, T., Saavedra, M.I., Martinez-Arroyo, M.A., 2010. Optical properties of aerosols: Southern Mexico City. Atmosfera 23, 403-408.

Garrido Frenich, A., Martínez Galera, M., Martínez Vidal, J.L., Massart, D.L., Torres-Lapasió, J.R., De Braekeleer, K., Wang, J.-H., Hopke, P.K., 2000. Resolution of multicomponent peaks by orthogonal projection approach, positive matrix factorization and alternating least squares. Analytica Chimica Acta 411, 145-155.

Geiser, M., Rothen-Rutishauser, B., Kapp, N., Schürch, S., Kreyling, W., Schulz, H., Semmler, M., Hof, V.I., Heyder, J., Gehr, P., 2005. Ultrafine Particles Cross Cellular Membranes by Nonphagocytic Mechanisms in Lungs and in Cultured Cells. Environ. Health Perspect. 113, 1555-1560.

Gerecke, A., Thielmann, A., Gutzwiller, L., Rossi, M.J., 1998. The chemical kinetics of HONO formation resulting from heterogeneous interaction of NO2 with flame soot. Geophysical Research Letters 25, 2453-2456.

Gogoi, M.M., Krishna Moorthy, K., Babu, S.S., Bhuyan, P.K., 2009. Climatology of columnar aerosol properties and the influence of synoptic conditions: First-time results from the northeastern region of India. Journal of Geophysical Research: Atmospheres 114, D08202.

Goodman, A., Underwood, G., Grassian, V., 2000. A laboratory study of the heterogeneous reaction of nitric acid on calcium carbonate particles. Journal of Geophysical Research: Atmospheres (1984–2012) 105, 29053-29064.

Gray, H.A., Cass, G.R., Huntzicker, J.J., Heyerdahl, E.K., Rau, J.A., 1986. Characteristics of atmospheric organic and elemental carbon particle concentrations in Los Angeles. Environmental Science & Technology 20, 580-589.

Groblicki, P.J., Wolff, G.T., Countess, R.J., 1981. Visibility-reducing species in the denver "brown cloud"—I. Relationships between extinction and chemical composition. Atmospheric Environment (1967) 15, 2473-2484.

Guo, H., Ding, A.J., So, K.L., Ayoko, G., Li, Y.S., Hung, W.T., 2009. Receptor modeling of source apportionment of Hong Kong aerosols and the implication of urban and regional contribution. Atmospheric Environment 43, 1159-1169.

Guo, S., Hu, M., Wang, Z.B., Slanina, J., Zhao, Y.L., 2010. Size-resolved aerosol water-soluble ionic compositions in the summer of Beijing: implication of regional secondary formation. Atmospheric Chemistry and Physics 10, 947-959.

Han, J., Moon, K., Lee, S., Kim, Y., Ryu, S., Cliff, S., Yi, S., 2006. Size-resolved source apportionment of ambient particles by positive matrix factorization at Gosan background site in East Asia. Atmospheric Chemistry and Physics 6, 211-223.

Hand, J.L., Malm, W.C., 2007. Review of aerosol mass scattering efficiencies from ground-based measurements since 1990. Journal of Geophysical Research: Atmospheres 112, D16203.

Hand, J., Copeland, D., Day, A., Indresand, D., Malm, W., McDade, C., Moore, C., Pitchford, M., Schichtel, B., Watson, J., 2011. Spatial and seasonal patterns and temporal variability of haze and its constituents in the United States: Report V: June 2011. Cooperative Institute for Research in the Atmosphere for the IMPROVE program, Ft. collins, Co.

Heald, C.L., Ridley, D.A., Kroll, J.H., Barrett, S.R.H., Cady-Pereira, K.E., Alvarado, M.J., Holmes, C.D., 2014. Contrasting the direct radiative effect and direct radiative forcing of aerosols. Atmospheric Chemistry and Physics 14, 5513-5527.

Hering, S.V., Friedlander, S.K., 1982. Origins of aerosol sulfur size distributions in the Los Angeles basin. Atmospheric Environment (1967) 16, 2647-2656.

Hering, S.V., 1995. Impactors, cyclones, and other inertial and gravitational collectors. Air Sampling Instruments 8, 279-321.

Ho, K.-f., 2003. Source apportionment of toxic air pollutants and particulate matter in Hong Kong. Ph.D. Dissertation. The Hong Kong Polytechnic University.

Ho, K.F., Cao, J.J., Lee, S.C., Chan, C.K., 2006a. Source apportionment of $PM_{2.5}$ in urban area of Hong Kong. Journal of Hazardous Materials 138, 73-85.

Ho, K.F., Lee, S.C., Cao, J.J., Chow, J.C., Watson, J.G., Chan, C.K., 2006b. Seasonal variations and mass closure analysis of particulate matter in Hong Kong. Science of the Total Environment 355, 276-287.

Hopke, P.K., Gladney, E.S., Gordon, G.E., Zoller, W.H., Jones, A.G., 1976. The use of multivariate analysis to identify sources of selected elements in the Boston urban aerosol. Atmospheric Environment (1967) 10, 1015-1025.

Howell, S.G., Huebert, B.J., 1998. Determining marine aerosol scattering characteristics at ambient humidity from size‐resolved chemical composition. Journal of Geophysical Research: Atmospheres (1984–2012) 103, 1391-1404.

Huang, H., Liu, H., Jiang, W., Huang, S., Zhang, Y., 2006a. Physical and chemical characteristics and source apportionment of $PM_{2.5}$ in Nanjing. Climate Environmental Research 6, 713-722.

Huang, X.-F., Yu, J.Z., He, L.-Y., Hu, M., 2006b. Size Distribution Characteristics of Elemental Carbon Emitted from Chinese Vehicles: Results of a Tunnel Study and Atmospheric Implications. Environmental Science & Technology 40, 5355-5360.

Huang, X.F., Yu, J.Z., He, L.Y., Hu, M., 2006c. Size distribution characteristics of elemental carbon emitted from Chinese vehicles: Results of a tunnel study and atmospheric implications. Environmental Science & Technology 40, 5355-5360.

Huang, X.F., Yu, J.Z., He, L.Y., Yuan, Z.B., 2006d. Water-soluble organic carbon and oxalate in aerosols at a coastal urban site in China: Size distribution characteristics, sources, and formation mechanisms. Journal of Geophysical Research: Atmospheres 111.

Huang, X.F., Yu, J.Z., 2008. Size distributions of elemental carbon in the atmosphere of a coastal urban area in South China: characteristics, evolution processes, and implications for the mixing state. Atmospheric Chemistry and Physics 8, 5843-5853.

Huang, X.-F., Yu, J.Z., Yuan, Z., Lau, A.K.H., Louie, P.K.K., 2009. Source analysis of high particulate matter days in Hong Kong. Atmospheric Environment 43, 1196-1203.

Huang, Z., Harrison, R.M., Allen, A.G., James, J.D., Tilling, R.M., Yin, J., 2004. Field intercomparison of filter pack and impactor sampling for aerosol nitrate, ammonium, and sulphate at coastal and inland sites. Atmospheric Research 71, 215-232.

Hyvärinen, A.P., Lihavainen, H., Komppula, M., Sharma, V.P., Kerminen, V.M., Panwar, T.S., Viisanen, Y., 2009. Continuous measurements of optical properties of atmospheric aerosols in Mukteshwar, northern India. Journal of Geophysical Research: Atmospheres 114, D08207.

Jeong, C.-H., Herod, D., Dabek-Zlotorzynska, E., Ding, L., McGuire, M.L., Evans, G., 2013. Identification of the Sources and Geographic Origins of Black Carbon using Factor Analysis at Paired Rural and Urban sites. Environmental Science & Technology 47, 8462-8470.

John, W., Wall, S.M., Ondo, J.L., Winklmayr, W., 1990. Modes in the size distributions of atmospheric inorganic aerosol. Atmospheric Environment Part A. General Topic 24, 2349-2359.

Jones, W., Jankovic, J., Baron, P., 1983. Design, Construction and Evaluation of a Multi-Stage "Cassette" Impactor. American Industrial Hygiene Association Journal 44, 409-418.

Jung, J., Lee, H., Kim, Y.J., Liu, X., Zhang, Y., Gu, J., Fan, S., 2009. Aerosol chemistry and the effect of aerosol water content on visibility impairment and radiative forcing in Guangzhou during the 2006 Pearl River Delta campaign. Journal of Environmental Management 90, 3231-3244.

Kadowaki, S., 1986. On the nature of atmospheric oxidation processes of sulfur dioxide to sulfate and of nitrogen dioxide to nitrate on the basis of diurnal variations of

sulfate, nitrate, and other pollutants in an urban area. Environmental Science &Technology 20, 1249-1253.

Kannosto, J., Virtanen, A., Lemmetty, M., Makela, J.M., Keskinen, J., Junninen, H., Hussein, T., Aalto, P., Kulmala, M., 2008. Mode resolved density of atmospheric aerosol particles. Atmospheric Chemistry and Physics 8, 5327-5337.

Kerminen, V.-M., Wexler, A.S., 1995. Enhanced formation and development of sulfate particles due to marine boundary layer circulation. Journal of Geophysical Research: Atmospheres 100, 23051-23062.

Khoder, M.I., 2002. Atmospheric conversion of sulfur dioxide to particulate sulfate and nitrogen dioxide to particulate nitrate and gaseous nitric acid in an urban area. Chemosphere 49, 675-684.

Kim, E., Hopke, P.K., Larson, T.V., Covert, D.S., 2003. Analysis of Ambient Particle Size Distributions Using Unmix and Positive Matrix Factorization. Environmental Science & Technology 38, 202-209.

Kim, Y.J., Kim, K.W., Kim, S.D., Lee, B.K., Han, J.S., 2006. Fine particulate matter characteristics and its impact on visibility impairment at two urban sites in Korea: Seoul and Incheon. Atmospheric Environment 40, Supplement 2, 593-605.

Kong, S., Wen, B., Chen, K., Yin, Y., Li, L., Li, Q., Yuan, L., Li, X., Sun, X., 2014. Ion chemistry for atmospheric size-segregated aerosol and depositions at an

offshore site of Yangtze River Delta region, China. Atmospheric Research 147–148, 205-226.

Kumar, A., Sarin, M.M., Sudheer, A.K., 2008. Mineral and anthropogenic aerosols in Arabian Sea–atmospheric boundary layer: Sources and spatial variability. Atmospheric Environment 42, 5169-5181.

Lai, L.Y., Sequeira, R., 2001. Visibility degradation across Hong Kong: its components and their relative contributions. Atmospheric Environment 35, 5861-5872.

Lamarque, J.F., Bond, T.C., Eyring, V., Granier, C., Heil, A., Klimont, Z., Lee, D., Liousse, C., Mieville, A., Owen, B., Schultz, M.G., Shindell, D., Smith, S.J., Stehfest, E., Van Aardenne, J., Cooper, O.R., Kainuma, M., Mahowald, N., McConnell, J.R., Naik, V., Riahi, K., van Vuuren, D.P., 2010. Historical (1850–2000) gridded anthropogenic and biomass burning emissions of reactive gases and aerosols: methodology and application. Atmospheric Chemistry and Physics 10, 7017-7039.

Lan, Z.-J., Chen, D.-L., Li, X., Huang, X.-F., He, L.-Y., Deng, Y.-G., Feng, N., Hu, M., 2011. Modal characteristics of carbonaceous aerosol size distribution in an urban atmosphere of South China. Atmospheric Research 100, 51-60.

Laven, P., 2005. Atmospheric glories: simulations and observations. Applied Optics 44, 5667-5674.

Lee, E., Chan, C.K., Paatero, P., 1999. Application of positive matrix factorization in source apportionment of particulate pollutants in Hong Kong. Atmospheric Environment 33, 3201-3212.

Lee, S.C., Cheng, Y., Ho, K.F., Cao, J.J., Louie, P.K.K., Chow, J.C., Watson, J.G., 2006. $PM_{1.0}$ and $PM_{2.5}$ Characteristics in the Roadside Environment of Hong Kong. Aerosol Science and Technology 40, 157-165.

Lee, Y.L., Sequeira, R., 2002. Water-soluble aerosol and visibility degradation in Hong Kong during autumn and early winter, 1998. Environmental Pollution 116, 225-233.

Li, X., He, K., Li, C., Yang, F., Zhao, Q., Ma, Y., Cheng, Y., Ouyang, W., Chen, G., 2013. $PM_{2.5}$ mass, chemical composition and light extinction before and during the 2008 Beijing Olympics. Journal of Geophysical Research: Atmospheres, 2013JD020106.

Limpert, E., Stahel, W.A., Abbt, M., 2001. Log-normal Distributions across the Sciences: Keys and Clues: On the charms of statistics, and how mechanical models resembling gambling machines offer a link to a handy way to characterize log-normal distributions, which can provide deeper insight into variability and probability—normal or log-normal: That is the question. BioScience 51, 341-352.

Liu, N., Yu, Y., He, J., Zhao, S., 2013. Integrated modeling of urban-scale pollutant transport: application in a semi-arid urban valley, Northwestern China. Atmospheric Pollution Research 4.

Liu, S., Hu, M., Slanina, S., He, L.Y., Niu, Y.W., Bruegemann, E., Gnauk, T., Herrmann, H., 2008. Size distribution and source analysis of ionic compositions of aerosols in polluted periods at Xinken in Pearl River Delta (PRD) of China. Atmospheric Environment 42, 6284-6295.

Louie, P.K.K., Chow, J.C., Chen, L.W.A., Watson, J.G., Leung, G., Sin, D.W.M., 2005. $PM_{2.5}$ chemical composition in Hong Kong: urban and regional variations. Science of the Total Environment 338, 267-281.

Lowenthal, D.H., Kumar, N., 2003. $PM_{2.5}$ mass and light extinction reconstruction in IMPROVE. Journal of the Air & Waste Management Association 53, 1109-1120.

Lowenthal, D.H., Kumar, N., 2004. Variation of mass scattering efficiencies in IMPROVE. Journal of the Air & Waste Management Association 54, 926-934.

Lowenthal, D., Kumar, N., 2006. Light scattering from sea-salt aerosols at Interagency Monitoring of Protected Visual Environments (IMPROVE) sites. Journal of the Air & Waste Management Association 56, 636-642.

Malm, W.C., Sisler, J.F., Huffman, D., Eldred, R.A., Cahill, T.A., 1994. Spatial and seasonal trends in particle concentration and optical extinction in the United States. Journal of Geophysical Research 99, 1347-1370.

Malm, W.C., Pitchford, M.L., 1997. Comparison of calculated sulfate scattering efficiencies as estimated from size-resolved particle measurements at three national locations. Atmospheric Environment 31, 1315-1325.

Malm, W.C., 1999. Introduction to visibility. Cooperative Institute for Research in the Atmosphere, NPS Visibility Program, Colorado State University.

Malm, W.C., Day, D.E., Kreidenweis, S.M., Collett, J.L., Lee, T., 2003. Humidity-dependent optical properties of fine particles during the Big Bend Regional Aerosol and Visibility Observational Study. Journal of Geophysical Research: Atmospheres 108, 4279.

Man, C.K., Shih, M.Y., 2001. Light scattering and absorption properties of aerosol particles in Hong Kong. Journal of Aerosol Science 32, 795-804.

Marple, V.A., Rubow, K.L., Behm, S.M., 1991. A Microorifice Uniform Deposit Impactor (MOUDI): Description, Calibration, and Use. Aerosol Science and Technology 14, 434-446.

Meng, Z., Seinfeld, J.H., 1994. On the Source of the Submicrometer Droplet Mode of Urban and Regional Aerosols. Aerosol Science and Technology 20, 253-265.

Mie, G., 1908. Beiträge zur Optik trüber Medien, speziell kolloidaler Metallösungen. Annalen der physik 330, 377-445.

Moosmüller, H., Chakrabarty, R.K., Arnott, W.P., 2009. Aerosol light absorption and its measurement: A review. Journal of Quantitative Spectroscopy and Radiative Transfer 110, 844-878.

Milford, J.B., Davidson, C.I., 1987. The Sizes of Particulate Sulfate aed Nitrate 1B the Atmosphere—A-Review. JAPCA 37, 125-134.

Novakov, T., Corrigan, C.E., 1996. Cloud condensation nucleus activity of the organic component of biomass smoke particles. Geophysical Research Letters 23, 2141-2144.

Paatero, P., Tapper, U., 1994. Positive matrix factorization: A non-negative factor model with optimal utilization of error estimates of data values. Environmetrics 5, 111-126.

Paredes-Miranda, G., Arnott, W.P., Jimenez, J.L., Aiken, A.C., Gaffney, J.S., Marley, N.A., 2009. Primary and secondary contributions to aerosol light scattering and absorption in Mexico City during the MILAGRO 2006 campaign. Atmospheric Chemistry and Physics 9, 3721-3730.

Park, S., Gong, S., Bouchet, V., Gong, W., Makar, P., Moran, M., Stroud, C., Zhang, J., 2011. Effects of black carbon aging on air quality predictions and direct radiative forcing estimation. Tellus B 63, 1026-1039.

Pathak, R.K., Wu, W.S., Wang, T., 2009. Summertime PM2.5 ionic species in four major cities of China: nitrate formation in an ammonia-deficient atmosphere. Atmospheric Chemistry and Physics 9, 1711-1722.

Penttinen, P., Timonen, K.L., Tiittanen, P., Mirme, A., Ruuskanen, J., Pekkanen, J., 2001. Ultrafine particles in urban air and respiratory health among adult asthmatics. European Respiratory Journal 17, 428-435.

Pitchford, M., Malm, W., Schichtel, B., Kumar, N., Lowenthal, D., Hand, J., 2007. Revised algorithm for estimating light extinction from IMPROVE particle speciation data. Journal of the Air & Waste Management Association 57, 1326-1336.

Plaza, J., Pujadas, M., Gómez-Moreno, F.J., Sánchez, M., Artíñano, B., 2011. Mass size distributions of soluble sulfate, nitrate and ammonium in the Madrid urban aerosol. Atmospheric Environment 45, 4966-4976.

Polissar, A.V., Hopke, P.K., Paatero, P., Malm, W.C., Sisler, J.F., 1998. Atmospheric aerosol over Alaska: 2. Elemental composition and sources. Journal of Geophysical Research: Atmospheres 103, 19045-19057.

Rosenfeld, D., 1999. TRMM observed first direct evidence of smoke from forest fires inhibiting rainfall. Geophysical research letters 26, 3105-3108.

Russell, L.M., 2003. Aerosol Organic-Mass-to-Organic-Carbon Ratio Measurements. Environmental Science & Technology 37, 2982-2987.

Saksena, S., Quang, T.N., Nguyen, T., Dang, P.N., Flachsbart, P., 2008. Commuters' exposure to particulate matter and carbon monoxide in Hanoi, Vietnam. Transportation Research Part D: Transport and Environment 13, 206-211.

Schryer, D.R., 1982. Heterogeneous atmospheric chemistry. American Geophysical Union.

Seinfeld, J.H., Pandis, S.N., 2006. Atmospheric chemistry and physics: from air pollution to climate change. John Wiley & Sons.

Senaratne, I., Shooter, D., 2004. Elemental composition in source identification of brown haze in Auckland, New Zealand. Atmospheric Environment 38, 3049-3059.

Sequeira, R., Lai, K.-H., 1998. The effect of meteorological parameters and aerosol constituents on visibility in urban Hong Kong. Atmospheric Environment 32, 2865-2871.

Sisler, J.F., Malm, W., Gebhart, K., Pitchford, M.L., 1996. Spatial and Seasonal Patterns and Long Term Variability of the composition of the Haze in the United States. Report ISSN, 0737-5352, CIRA, Ft. Collins, Co.

Sheridan, P.J., Brock, C.A., Wilson, J.C., 1994. Aerosol particles in the upper troposphere and lower stratosphere: Elemental composition and morphology of individual particles in northern midlatitudes. Geophysical Research Letters 21, 2587-2590.

Sloane, C.S., 1983. Optical properties of aerosols—Comparison of measurements with model calculations. Atmospheric Environment (1967) 17, 409-416.

Sloane, C.S., Wolff, G.T., 1985. Prediction of ambient light scattering using a physical model responsive to relative humidity: Validation with measurements from Detroit. Atmospheric Environment (1967) 19, 669-680.

Sloane, C.S., 1986. Effect of composition on aerosol light scattering efficiencies. Atmospheric Environment (1967) 20, 1025-1037.

Sloane, C.S., Watson, J., Chow, J., Pritchett, L., Willard Richards, L., 1991. Size-segregated fine particle measurements by chemical species and their impact on visibility impairment in Denver. Atmos.Env.Part A. General Topic 25, 1013-1024.

Solomon, S., 2007. Climate change 2007-the physical science basis: Working group I contribution to the fourth assessment report of the IPCC. Cambridge University Press.

Song, Y., Zhang, Y., Xie, S., Zeng, L., Zheng, M., Salmon, L.G., Shao, M., Slanina, S., 2006. Source apportionment of $PM_{2.5}$ in Beijing by positive matrix factorization. Atmospheric Environment 40, 1526-1537.

Tan, J.-H., Duan, J.-C., Ma, Y.-L., Yang, F.-M., Cheng, Y., He, K.-B., Yu, Y.-C., Wang, J.-W., 2014. Source of atmospheric heavy metals in winter in Foshan, China. Science of The Total Environment 493, 262-270.

Tan, J., Duan, J., Zhen, N., He, K., Hao, J., 2016. Chemical characteristics and source of size-fractionated atmospheric particle in haze episode in Beijing. Atmospheric Research 167, 24-33.

Tang, I.N., 1996. Chemical and size effects of hygroscopic aerosols on light scattering coefficients. Journal of Geophysical Research: Atmospheres (1984–2012) 101, 19245-19250.

Tang, I.N., Tridico, A., Fung, K., 1997. Thermodynamic and optical properties of sea salt aerosols. Journal of Geophysical Research: Atmospheres (1984–2012) 102, 23269-23275.

Tao, J., Ho, K.-F., Chen, L., Zhu, L., Han, J., Xu, Z., 2009. Effect of chemical composition of $PM_{2.5}$ on visibility in Guangzhou, China, 2007 spring. Particuology 7, 68-75.

Tao, J., Gao, J., Zhang, L., Zhang, R., Che, H., Zhang, Z., Lin, Z., Jing, J., Cao, J., Hsu, S.C., 2014. $PM_{2.5}$ pollution in a megacity of southwest China: source apportionment and implication. Atmospheric Chemistry and Physics 14, 8679-8699.

Tao, J., Zhang, L., Gao, J., Wang, H., Chai, F., Wang, S., 2015. Aerosol chemical composition and light scattering during a winter season in Beijing. Atmospheric Environment 110, 36-44.

Tsai, J.-H., Lin, J.-H., Yao, Y.-C., Chiang, H.-L., 2012. Size distribution and water soluble ions of ambient particulate matter on episode and non-episode days in Southern Taiwan. Aerosol & Air Quality Research 12, 263-274.

Titos, G., Foyo-Moreno, I., Lyamani, H., Querol, X., Alastuey, A., Alados-Arboledas, L., 2012. Optical properties and chemical composition of aerosol particles at an

urban location: An estimation of the aerosol mass scattering and absorption efficiencies. Journal of Geophysical Research: Atmospheres 117.

Twomey, S., 1975. Comparison of constrained linear inversion and an iterative nonlinear algorithm applied to the indirect estimation of particle size distributions. Journal of Computational Physics 18, 188-200.

Vaughan, N.P., 1989. The Andersen impactor: Calibration, wall losses and numerical simulation. Journal of Aerosol Science 20, 67-90.

Viana, M., Kuhlbusch, T.A.J., Querol, X., Alastuey, A., Harrison, R.M., Hopke, P.K., Winiwarter, W., Vallius, M., Szidat, S., Prévôt, A.S.H., Hueglin, C., Bloemen, H., Wåhlin, P., Vecchi, R., Miranda, A.I., Kasper-Giebl, A., Maenhaut, W., Hitzenberger, R., 2008. Source apportionment of particulate matter in Europe: A review of methods and results. Journal of Aerosol Science 39, 827-849.

Vinoj, V., Satheesh, S.K., Moorthy, K.K., 2010. Optical, radiative, and source characteristics of aerosols at Minicoy, a remote island in the southern Arabian Sea. Journal of Geophysical Research: Atmospheres 115, D01201.

Wang, P., Cao, J.-j., Shen, Z.-x., Han, Y.-m., Lee, S.-c., Huang, Y., Zhu, C.-s., Wang, Q.-y., Xu, H.-m., Huang, R.-j., 2015. Spatial and seasonal variations of $PM_{2.5}$ mass and species during 2010 in Xi'an, China. Science of The Total Environment 508, 477-487.

Wang, Q., Cao, J., Tao, J., Li, N., Su, X., Chen, L.W.A., Wang, P., Shen, Z., Liu, S., Dai, W., 2013. Long-Term Trends in Visibility and at Chengdu, China. PLoS ONE 8, e68894.

Wang, R., Tao, S., Wang, W., Liu, J., Shen, H., Shen, G., Wang, B., Liu, X., Li, W., Huang, Y., Zhang, Y., Lu, Y., Chen, H., Chen, Y., Wang, C., Zhu, D., Wang, X., Li, B., Liu, W., Ma, J., 2012. Black Carbon Emissions in China from 1949 to 2050. Environmental Science & Technology; 46: 7595-7603.

Wang, T., Group, H.K.E.P.D.A.S., Technology, H.K.P.U.R.C.f.E., Management, 2003. Study of Visibility Reduction and Its Causes in Hong Kong: Final Report. Research Centre for Environmental Technology and Management, Department of Civil and Structural Engineering, Hong Kong Polytechnic University.

Wang, T., Guo, H., Blake, D.R., Kwok, Y.H., Simpson, I.J., Li, Y.S., 2005. Measurements of Trace Gases in the Inflow of South China Sea Background Air and Outflow of Regional Pollution at Tai O, Southern China. Journal of Atmospheric Chemistry 52, 295-317.

Wang, X., Wang, T., Pathak, R., Hallquist, M., Gao, X., Nie, W., Xue, L., Gao, J., Gao, R., Zhang, Q., Wang, W., Wang, S., Chai, F., Chen, Y., 2013. Size distributions of aerosol sulfates and nitrates in Beijing during the 2008 Olympic Games: Impacts of pollution control measures and regional transport. Advances in Atmospheric Sciences 30, 341-353.

Wang, Y., Zhang, X., Arimoto, R., Cao, J., Shen, Z., 2004. The transport pathways and sources of PM10 pollution in Beijing during spring 2001, 2002 and 2003. Geophysical research letters 31, L14110.

Wang, Y.Q., Zhang, X.Y., Draxler, R.R., 2009. TrajStat: GIS-based software that uses various trajectory statistical analysis methods to identify potential sources from long-term air pollution measurement data. Environmental Modelling & Software 24, 938-939.

Watson, J.G., Chow, J.C., Frazier, C.A., 1999. X-ray fluorescence analysis of ambient air samples, in: Landsberger, S., Creatchman, M. (Eds.), Vo-Dinh, T., ed. Advances in environmental industrial and process control technologies: v. 1 ed. Gordon and Breach Science Publishers, Amsterdam, The Netherlands, pp. 67-96.

Watson, J.G., 2002. Visibility: Science and Regulation. Journal of the Air & Waste Management Association 52, 628-713.

Watson, J.G., Chow, J.C. and Chen, L.W.A. (2005) Summary of Organic and Elemental Carbon/Black Carbon Analysis Methods and Intercomparisons. Aerosol and Air Quality Research, 5, 65-102.

Watson, J.G., Chow, J.C., Chen, L.W.A., Frank, N.H., 2009. Methods to Assess Carbonaceous Aerosol Sampling Artifacts for IMPROVE and Other Long-Term Networks. Journal of the Air & Waste Management Association 59, 898-911.

Watson, J.G., Chow, J.C., Lowenthal, D.H., Antony Chen, L.W., Shaw, S., Edgerton, E.S., Blanchard, C.L., 2015. $PM_{2.5}$ source apportionment with organic markers in the Southeastern Aerosol Research and Characterization (SEARCH) study. Journal of the Air & Waste Management Association 65, 1104-1118.

Weingartner, E., Saathoff, H., Schnaiter, M., Streit, N., Bitnar, B., Baltensperger, U., 2003. Absorption of light by soot particles: determination of the absorption coefficient by means of aethalometers. Journal of Aerosol Science 34, 1445-1463.

Whitby, K.T., Sverdrup, G.M., 1980. California aerosols - their physical and chemical characteristics. Journal Name: Adv. Environmental Science & Technology; (United States); Journal Volume: 9, Medium: X; Size: Pages: 477-517.

Willeke, K., Whitby, K.T., 1975. Atmospheric Aerosols: Size Distribution Interpretation. Journal of the Air Pollution Control Association 25, 529-534.

Winklmayr, W., Wang, H.-C., John, W., 1990. Adaptation of the Twomey Algorithm to the Inversion of Cascade Impactor Data. Aerosol Science and Technology 13, 322-331.

Wong, M.S., Nichol, J., Lee, K.H., Lee, B.Y., 2011. Monitoring 2.5 mu m particulate matter within urbanized regions using satellite-derived aerosol optical thickness, a study in Hong Kong. International Journal of Remote Sensing 32, 8449-8462.

Xu, J.W., Tao, J., Zhang, R.J., Cheng, T.T., Leng, C.P., Chen, J.M., Huang, G.H., Li, X., Zhu, Z.Q., 2012. Measurements of surface aerosol optical properties in winter of Shanghai. Atmospheric Research 109, 25-35.

Yan, P., Tang, J., Huang, J., Mao, J.T., Zhou, X.J., Liu, Q., Wang, Z.F., Zhou, H.G., 2008. The measurement of aerosol optical properties at a rural site in Northern China. Atmospheric Chemistry and Physics 8, 2229-2242.

Yang, D., Li, C., Lau, A.K.-H., Li, Y., 2013. Long-term measurement of daytime atmospheric mixing layer height over Hong Kong. Journal of Geophysical Research: Atmospheres 118, 2422-2433.

Yang, M., Howell, S.G., Zhuang, J., Huebert, B.J., 2009. Attribution of aerosol light absorption to black carbon, brown carbon, and dust in China – interpretations of atmospheric measurements during EAST-AIRE. Atmospheric Chemistry and Physics 9, 2035-2050.

Yao, X., Lau, A.P.S., Fang, M., Chan, C.K., Hu, M., 2003a. Size distributions and formation of ionic species in atmospheric particulate pollutants in Beijing, China: 1—inorganic ions. Atmospheric Environment 37, 2991-3000.

Yao, X.H., Fang, M., Chan, C.K., 2003b. The size dependence of chloride depletion in fine and coarse sea-salt particles. Atmospheric Environment 37, 743-751.

Yao, X.H., Zhang, L., 2011. Sulfate formation in atmospheric ultrafine particles at Canadian inland and coastal rural environments. Journal of Geophysical Research: Atmospheres 116, D10202.

Yau, P.S., Lee, S.C., Cheng, Y., Huang, Y., Lai, S.C., Xu, X.H., 2013. Contribution of ship emissions to the fine particulate in the community near an international port in Hong Kong. Atmospheric Research 124, 61-72.

Yu, H., Wu, C., Wu, D., Yu, J.Z., 2010. Size distributions of elemental carbon and its contribution to light extinction in urban and rural locations in the pearl river delta region, China. Atmospheric Chemistry and Physics 10, 5107-5119.

Zhang, X., Lin, Y.-H., Surratt, J.D., Weber, R.J., 2013. Sources, Composition and Absorption Ångström Exponent of Light-absorbing Organic Components in Aerosol Extracts from the Los Angeles Basin. Environmental Science & Technology

Zhang, R., Jing, J., Tao, J., Hsu, S.C., Wang, G., Cao, J., Lee, C.S.L., Zhu, L., Chen, Z., Zhao, Y., Shen, Z., 2013. Chemical characterization and source apportionment of $PM_{2.5}$ in Beijing: seasonal perspective. Atmospheric Chemistry and Physics 13, 7053-7074.

Zhou, S., Wang, T., Wang, Z., Li, W., Xu, Z., Wang, X., Yuan, C., Poon, C.N., Louie, P.K.K., Luk, C.W.Y., Wang, W., 2014. Photochemical evolution of organic

aerosols observed in urban plumes from Hong Kong and the Pearl River Delta of China. Atmospheric Environment 88, 219-229.

Zhuang, B.L., Li, S., Wang, T.J., Deng, J.J., Xie, M., Yin, C.Q., Zhu, J.L., 2013. Direct radiative forcing and climate effects of anthropogenic aerosols with different mixing states over China. Atmospheric Environment 79, 349-361.

Zhuang, H., Chan, C.K., Fang, M., Wexler, A.S., 1999a. Formation of nitrate and non-sea-salt sulfate on coarse particles. Atmospheric Environment 33, 4223-4233.

Zhuang, H., Chan, C.K., Fang, M., Wexler, A.S., 1999b. Size distributions of particulate sulfate, nitrate, and ammonium at a coastal site in Hong Kong. Atmospheric Environment 33, 843-853.

Appendix A: List of Abbreviations

ACI	Andersen Cascade Impactor
AERONET	Aerosol Robotic Network
B_{ap}	Particle light absorption
B_{ag}	Gaseous light absorption
B_{sp}	Particle light scattering
B_{sg}	Gaseous light scattering
B_{ext}	Light extinction
BC	Black Carbon
BrC	Brown Carbon
CMB	Chemical Mass Balance
CWT	Concentration Weighted Trajectory
DRF	Direct Radiative Forcing
EC	Elemental Carbon
EPA	Environmental Protection agency
FID	Flame Ionization Detection

HKEPD	Hong Kong Environmental Protection department
HKPU	Hong Kong Polytechnic University
HT	Hok Tsui
IMPROVE	Interagency Monitoring of Protected Visual Environment
MAE	Mass Absorption Efficiency
MAAP	Multi-Angle Absorption Photometer
MDL	Method of Detection Limit
MLR	Multi-linear regression
MMAD	Mass Median Aerodynamic Diameters
MOUDI	Micro-Orifice Uniform Deposit Impactor
MSE	Mass Scattering Efficiency
NIST	National Institute of Standard and Technology
NOR	Nitrogen Oxidation Ratio
OC	Organic Carbon
PMF	Positive Matrix Factorization
PSAP	Particle Soot Absorption Photometer

PRD	Pearl River Delta
PSCF	Potential Source Contribution Function
PAX	Photoacoustic Extinctiometer
PM	Particulate Matter
POM	Particle Organic Matter
PCA-APCS	Principal Component Analysis with Absolute Principal Component Scores
RSP	Respirable Suspended Particles
RH	Relative Humidity
SSA	Single Scattering Albedo
SP2	Single Particle soot photometer
SOR	Sulfur Oxidation Ratio
S/N	Signal to Noise ratio
TC	Tung Chung
TEO	Trace Element Oxides
TOR	Thermal/Optical Reflectance

VR	Visual Range
XRF	X-ray fluorescence

Appendix B: Photos of sampling sites and equipment

Photo 1. The Hong Kong Polytechnic University

Photo 2. Tung Chung (TC) air monitoring station

Photo 3. Hok Tsui (HT) air monitoring station

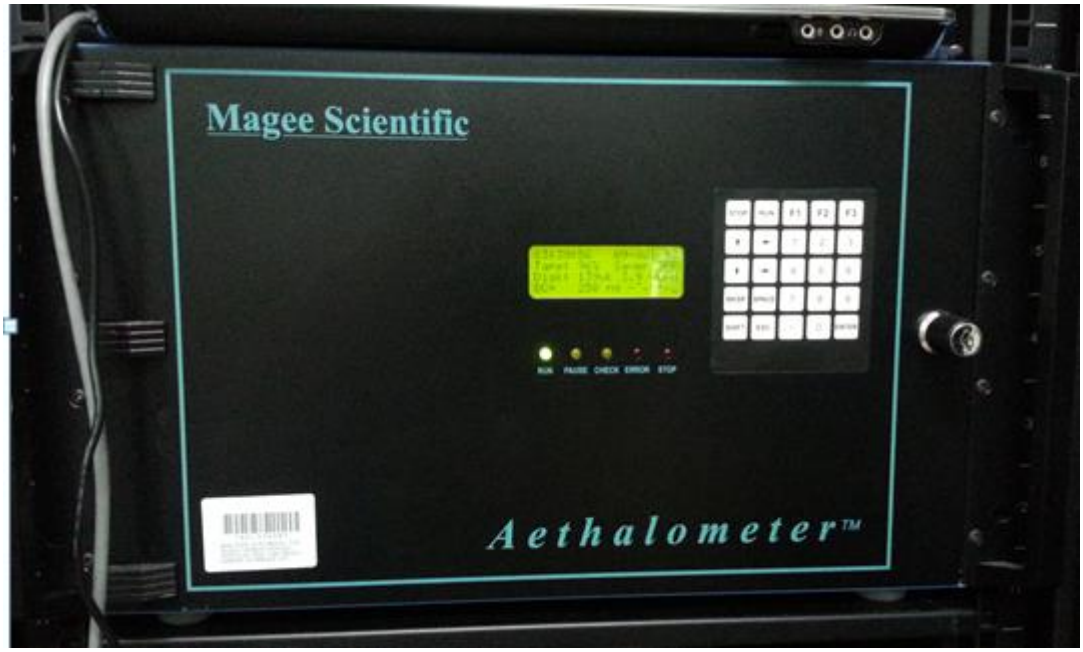

Photo 4. Aethalometer AE31

Photo 5. Nephelometer Ecotech M9003

Photo 6. MOUDI model 110